

THESIS ON INFORMATICS AND SYSTEM ENGINEERING C89

Pressure Sensitive Lateral Line for Underwater Robot

JAAS JEŽOV

TUT
PRESS

TALLINN UNIVERSITY OF TECHNOLOGY
Faculty of Information Technology
Centre for Biorobotics

Dissertation was accepted for the defence of the degree of Doctor of Philosophy in Engineering on August 28, 2013.

Supervisor: Prof. Maarja Kruusmaa
Centre for Biorobotics
Faculty of Information Technology
Tallinn University of Technology
Tallinn, Estonia

Opponents: Dr. Tjeerd C. Andringa
Institute of Artificial Intelligence
Faculty of Mathematics and Natural Sciences
University of Groningen
Groningen, The Netherlands

Dr. Nikola Mišković
Dept. of Control and Computer Engineering
Faculty of Electrical Engineering and Computing
University of Zagreb
Zagreb, Croatia

Defence of the thesis: October 15, 2013

Declaration:

Hereby I declare that this doctoral thesis, my original investigation and achievement, submitted for the doctoral degree at Tallinn University of Technology has not been submitted for any academic degree.

/Jaas Ježov/



European Union
European Social Fund



Investing in your future

Copyright: Jaas Ježov, 2013
ISSN 1406-4731
ISBN 978-9949-23-537-7 (publication)
ISBN 978-9949-23-538-4 (PDF)

INFORMAATIKA JA SÜSTEEMITEHNIKA C89

Rõhutundliku küljejoone kasutamine allveerobotil

JAAS JEŽOV

Contents

List of publications	7
Author’s Contribution to the Publications	8
Introduction	9
Motivation	9
Contribution of the thesis.....	10
Outline of the thesis.....	11
1 Background of the research	12
1.1 Flow negotiation in unsteady flow.....	13
1.1.1 Mechanical analog to Kármán gaiting	15
1.2 Flow sensing	16
1.2.1 Biological lateral line.....	16
1.2.2 Artificial flow sensors.....	18
1.2.3 Artificial lateral line sensing.....	20
1.3 Novelty beyond the related work.....	21
2 Materials and methods	23
2.1 Requirements for sensing platforms	23
2.2 Lateral line sensors	24
2.3 Platform 1	25
2.3.1 Experiments with Platform 1	26
2.4 Platform 2	27
2.4.1 Experiments with Platform 2	29
2.5 Platform 3	30
2.5.1 Experiments with Platform 3	32
2.6 Artificial lateral line calibration and testing	34
2.6.1 Sensitivity to pressure.....	34
2.6.2 Sensitivity to temperature	34
2.6.3 Effect of air bubbles in canals.....	34
2.7 Flow speed estimation with pressure sensors	35
2.7.1 Flow speed estimation in steady flow.....	36
2.7.2 Flow speed estimation in Kármán vortex street.....	38
Conclusion.....	39
3 Pressure sensing lateral line in steady and unsteady flows	41

3.1	Characterization of Kármán vortex street	42
3.1.1	Yaw angle offset in a vortex street and in steady flow	44
3.1.2	Lateral offset in Kármán vortex street	46
	Conclusion	48
4	Sensing self-motion with artificial lateral line	50
4.1	Forward and backward motion of the craft	50
4.2	Theoretical model	53
4.3	Mapping motion to pressure sensing	54
	Conclusion	56
5	Improving efficiency of tail fin propulsion	58
5.1	Swimming in Kármán vortex street	58
5.2	Vortex synchronization	59
5.3	Performance of the vortex synchronized tail beat	61
	Conclusion	64
	Conclusions and future work	66
	References	68
	Appendix A	77
	Appendix B	91
	Appendix C	103
	Acknowledgements	111
	Abstract	112
	Lühikokkuvõte	113
	Curriculum Vitae	114
	Elulookirjeldus	115

List of publications

This thesis is based on work reported in following publications. All publications are reprinted in Appendix of this thesis.

- A. R. Venturelli, O. Akanyeti, F. Visentin, J. Ježov, L. D. Chambers, G. Toming, J. Brown, M. Kruusmaa, W. M. Megill, and P. Fiorini, “Hydrodynamic pressure sensing with an artificial lateral line in steady and unsteady flows,” *Bioinspiration & Biomimetics*, vol. 7, no. 3, pp. 036004:1–12, 2012.
- B. O. Akanyeti, L. D. Chambers, J. Ježov, J. Brown, R. Venturelli, M. Kruusmaa, and W. M. Megill, “Self-motion effects on hydrodynamic pressure sensing. Part I: Forward backward motion,” *Bioinspiration & Biomimetics*, vol. 8, no. 2, pp. 026001:1–10, 2013.
- C. J. Ježov, O. Akanyeti, L. D. Chambers, and M. Kruusmaa, “Sensing oscillations in unsteady flow for better robotic swimming efficiency,” in *2012 IEEE International Conference on Systems, Man, and Cybernetics*, 2012, pp. 91–96.

Author's Contribution to the Publications

Publication A: the author designed, built and calibrated the sensor platform for experiments, contributed to interpreting the experimental data and to writing the manuscript.

Publication B: the author designed, built and calibrated the sensing platform for experiments, conducted experiments in cooperation with other authors of this publication and contributed to writing the manuscript.

Publication C: the author designed, built and calibrated the sensing platform for experiments, designed and performed the experiments, analyzed and interpreted the results, and was responsible for writing the publication.

Introduction

This thesis uses fish as inspiration to build a new kind of a sensory system for unmanned underwater vehicles. We describe fishlike robots that are equipped with pressure sensors to investigate the flow field around them. We also show how to interpret the information gathered with these sensors and how to detect periodically turbulent flow regions that can provide energy saving opportunities for underwater robots. To increase the usability of flow field information on moving crafts we have developed a method to predict self-motion signals in pressure sensors. And finally we put the information gathered from periodical turbulence in use and control the tail beat of a fishlike robot to increase the thrust by using alternating flows.

Motivation

In the vast underwater realm there is still a lot to be discovered. One reason why our knowledge about the aquatic world is limited is because of the harsh conditions that impede research. Current technologies trend towards using unmanned vehicles for jobs that are too demanding for humans. However the high hydrostatic pressure, reduced communication capabilities and invisible underwater currents challenge even machines. The development of terrestrial and aerial unmanned vehicles have progressed much further than the development of underwater vehicles because the liquid medium retards the use of electromagnetic signals for communication and navigation is interfered with undetectable currents.

The problem with flow currents is caused by the lack of suitable sensors for their detection. At the same time, fish as natural habitants of the underwater realm have had the ability to sense flow for millions of years. To detect flow currents they use a sensory organ called a lateral line. Only recently has the technology reached to a level that supports the manufacturing of flow sensors that are suitable for artificial lateral lines. The inspiration from biological lateral lines have resulted in many biomimetic designs of lateral line sensors that show promise for results comparable with their biological counterparts [1], [2].

As the artificial lateral line sensor technology is maturing, demand for tools that can help interpret the flow data that wasn't available before, is growing accordingly. Research presented in this thesis helps to move closer to understanding the wealth of information available in flow. Adaptation to environmental changes is the key for autonomy and thus it is expected that an underwater robot should change its control strategy to enhance swimming efficiency with respect to the surrounding flow regime. Even the knowledge of the flow direction can be used to orientate an underwater vehicle to reduce drag, but more sophisticated understanding of surroundings can help to carry out more complicated tasks faster and energy efficiently.

Research in artificial flow sensors is still mainly concerned with the sensitivity of the flow sensors and measuring the performance of the sensors in comparison with biological lateral line sensors [3–5]. Testing capabilities of these sensors help to improve the development process but to be able to start using these sensors on an underwater vehicle requires research with flow sensors mounted on a craft, testing them in a dynamic environment.

There is lack of research also in the area of flow feature recognition. Lateral line sensing of the features of a naturally occurring periodic turbulence can provide benchmark hydrodynamic challenges in laboratory conditions. From there this research can be expanded further to investigate and characterize other unsteady flows. Finding control strategies for periodically turbulent flow regimes may help to prepare underwater robots for more erratic flows.

Alternating flows are also known to be energy rich environments, providing resting opportunities for station holding fish in running waters. Even considering that manmade vehicles operate usually under different constraints compared to biological creatures, using the flow to maximize either thrust or efficiency of propulsion can be equally beneficial for marine vehicles. Reducing energy consumption is an important subject in control of underwater vehicles and if they can be programmed to recognize and use favorable flow conditions, the benefits will not only extend their battery life but also make their navigation more accurate.

Contribution of the thesis

This thesis addresses control oriented flow analysis using pressure sensors arranged into state-of-the-art artificial lateral line systems to test hydrodynamic hypothesis and analytical models. The contribution of this thesis is in:

- Designing and building artificial lateral line platforms for flow sensing experiments in flow tunnels, culminating in development of a fishlike sensory platform with 3D pressure field sensing capability around the head of the platform.
- Characterizing periodic turbulence from the perspective of a situated sensory agent in the flow and experimentally testing the methods to distinguish periodically turbulent flows from steady flows. The characterization presented in this thesis serves as a starting point for recognition of more complex flows.
- Proposing a method to derive a model that can predict pressure changes caused by self-motion. The predictions can be used to suppress self-induced signals in order to enhance the sensitivity to external stimuli.
- Showing that information sensed with pressure sensors in periodically turbulent flows can be used in a control loop to synchronize the tail beat of a fishlike robot with respect to vortices.

As a result an increase of thrust and efficiency of a tail fin propulsor is demonstrated.

Outline of the thesis

The material in this thesis is divided into 5 chapters. Chapter 1 gives an overview of fish swimming modes in steady and unsteady flows but the main focus of Chapter 1 is on the lateral line and its sensors, describing discoveries both about biological and manmade flow sensors. Chapter 2 provides a description of the equipment and methods used for the research disserted in chapters 3, 4 and 5. Chapter 3 shows the differences of steady and unsteady flows from the perspective of a sensing platform. The measurements are analyzed and interpreted for the characterization of flow regimes. Chapter 4 shows a method for building a model for reducing a self-movement signal in flow sensors and an inverse model to provide motion information with flow sensors. Chapter 5 describes the use of artificial lateral line sensors to detect vortices in the flow for vortex synchronized tail fin propulsion.

1 Background of the research

70 percent of the Earth's surface is covered with water. Human kind has used sea to extend trade and travel for thousands of years, exploiting different vessels and mechanisms to cover distances. Most common today is propeller propulsion that has been known for over 2000 years, but became common on ships only in the 19th century with use of steam engines. Since then the propeller design has improved to near perfection but it is still less efficient than fish swimming that uses fins instead of propellers.

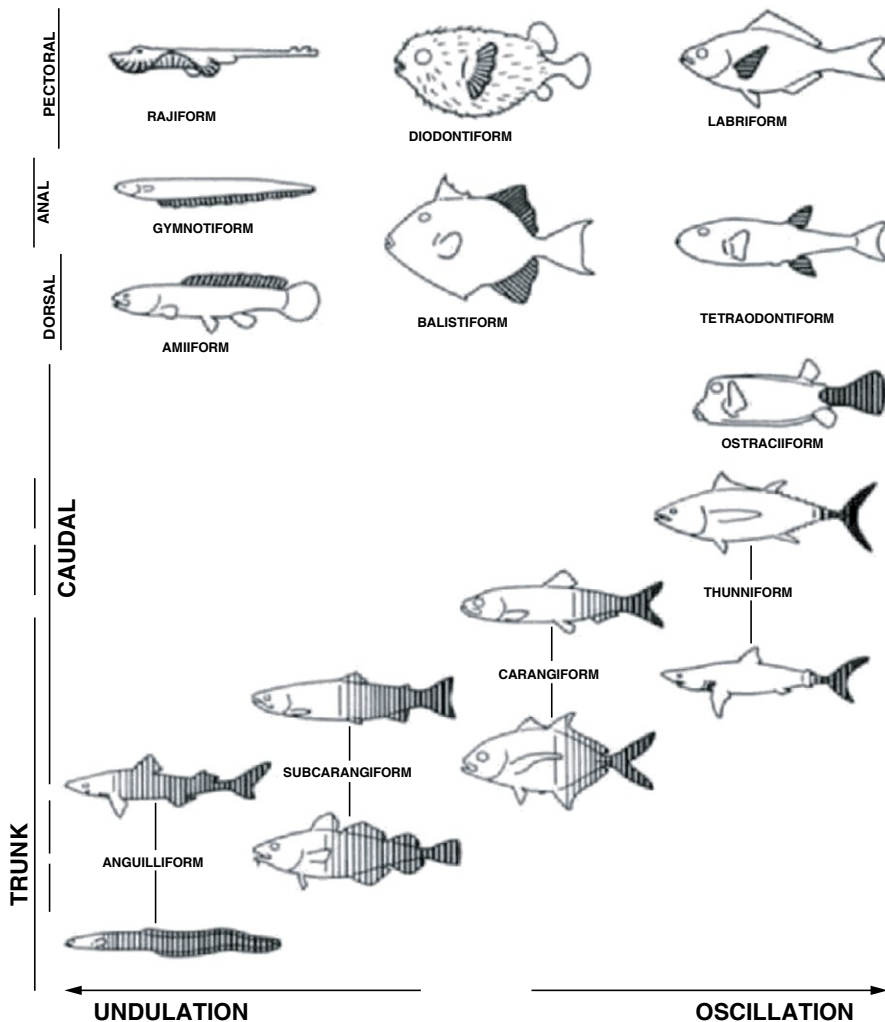


Figure 1.1. Swimming modes of fish. The vertical axis aligns swimming modes based on the role of body and fins in propulsion. The parts actively contributing to propulsion are shaded. The horizontal axis distributes the swimming modes based on the undulant and oscillatory motion. Adapted from [6].

There are over 32 000 fish species and their mechanisms for creating propulsion vary greatly. Some of the more common swimming modes are shown in Figure 1.1. Fish use different swimming modes to adapt to different hydrodynamic and behavioral conditions. For example pectoral fins are often used to achieve greater maneuverability whereas caudal fin swimming modes produce high speeds and high acceleration [6], [7].

In order to choose the best swimming pattern for its purposes, fish use different sensory organs to collect information about the environment. Vision, inertial sense of the inner ear and sense of smell play an important role in different swimming behaviors but in addition fish can also sense flow around them [8]. This sensing organ – the lateral line – gives them a direct feedback from the medium they use for propulsion. With the heightened perception of the surrounding fluid environment some fish are able to reduce their effort of swimming and let the hydrodynamic forces in the flow create thrust for them.

1.1 Flow negotiation in unsteady flow

Kinematics of swimming of different fish species has been studied extensively in steady flow [9–16]. Using that knowledge to design a propulsive system for manmade vehicles needs a decision about what is expected from this system. For example when high speed is the only criterion, it would be probably best to mimic the thunniform swimming mode, allowing the development of high cruising speed with very high efficiency [7]. However, when a fin propelled system is required to achieve a high cruising speed along with the good acceleration and maneuverability, one of the best examples would be trout. Trout mainly uses a subcarangiform swimming mode that provides speed and acceleration, whereas good maneuverability is achieved through the use of dorsal, pectoral and anal fins [17]. Trout are also known to swim in altered flows and have created an interest among biologists who have started to examine the kinematics of swimming in turbulent flows [18–20].

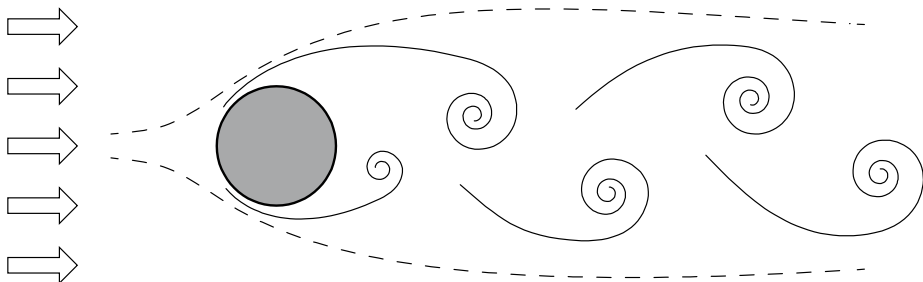


Figure 1.2. Schematic of a Kármán vortex street. Laminar flow from the left is obstructed by a circular cylinder. At moderate Reynolds numbers the viscosity of the fluid produce vortices that are shed intermittently from either side of the cylinder.

Turbulence in general is hard to characterize because of the unreliable repeatability of experiments. However, there is a flow phenomenon that is turbulent and at the same time regular and periodic. It is called a Kármán

Vortex Street and it can be produced by obstructing steady flow with a bluff body at moderate Reynolds numbers. In laboratory conditions it is usually created with a circular or D-shaped cylinder, but it also occurs commonly in natural running waters where rocks and tree trunks disturb flow. The phenomenon itself can be described as a successive pattern of alternating vortices, shed in the wake of a bluff body and traveling downstream in rows (Figure 1.2).

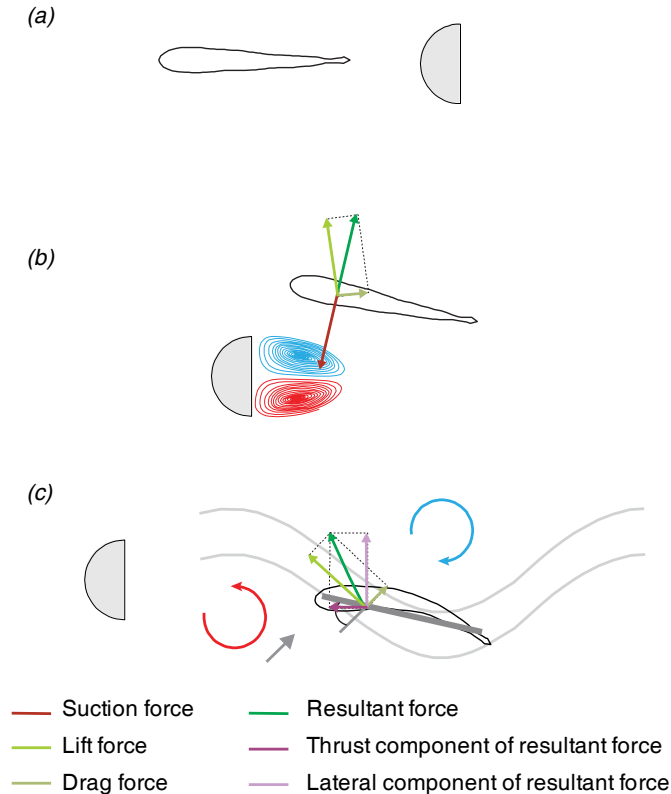


Figure 1.3. (a) Schematic of fish swimming in bow wake of a cylinder. (b) Schematic of principal forces acting on an entraining fish, adapted from [21]. (c) Schematic of principal forces acting on a Kármán gaiting fish, adapted from [22].

Rainbow trout (*Oncorhynchus mykiss*) and some other fish species have gained attention because of the ability to use these altered flows for their benefit. It has been hypothesized that trout prefer turbulent flows over steady because of the reduced drag condition, increased olfactory information and disorientation of prey, making the feeding easier [23], [24]. Experiments show that trout, placed in flow that is obstructed by a cylinder, have 3 preferred station holding positions in the near vicinity of it. They swim in the bow wake of the cylinder, entrain at the edge of the suction zone on either side of the cylinder or slalom directly behind the cylinder in the region where vortices have already formed [23], [21]. In the bow wake fish take advantage of the increased

pressure at the stagnation point that helps to reduce its drag while stationed just upstream from the cylinder (Figure 1.3(a)). Fish exhibit very little lateral movement when swimming in the bow wake, undulating the posterior part of the tail with reduced frequency [22]. For entraining, fish position themselves close to the cylinder at a side of a Kármán vortex street so that one side of a fish experience accelerated flow from outside of a Kármán street and the other side is influenced by vortices forming behind the cylinder, balancing the lift force and the suction force (Figure 1.3(b)). Entraining is very efficient for fish but the cost of losing the balance and resuming the entraining position can reduce its advantages [23].

Bow wake swimming and entraining make use of steady regions in altered flows. In a Kármán vortex street the body of the fish is influenced by turbulence. Kinematics of the fish swimming in a Kármán vortex street is distinguishable from swimming in steady flow by its increased lateral motion and body curvature, and also by the reduced tail beat frequency that match the vortex shedding frequency. This swimming mode has gained a specific name, Kármán gaiting, as it is fairly different from the usual gait in steady flows [22].

Liao et al. [18] have shown that Kármán gaiting trout decrease muscle activity while maintaining the distance from the cylinder. In Figure 1.3(c) is a schematic of a Kármán gaiting fish that can produce thrust by using its body as a reconfigurable hydrofoil, taking advantage of alternating flows. Beal et al. [25] have shown that for short time a dead fish can also produce thrust and swim upstream in a Kármán vortex street. However, to hold position, live fish make corrective strokes with fins, balancing thrust, drag, and lateral forces [23].

1.1.1 Mechanical analog to Kármán gaiting

Fish extracting energy from vortices by using its body as a hydrofoil have inspired researchers to investigate this phenomenon with the help of manmade mechanisms. Gopalkrishnan et al. [26] experimented with a rigid hydrofoil in a Kármán vortex street, synchronizing its movements with vortices and changing the phase of synchronization. The high aspect ratio hydrofoil, with a cord length less than half of the wavelength of the vortex street, was actuated in transverse (heave) and rotational (pitch) motion. In their experiments they observed the wake of the hydrofoil and categorized it based on how a vortex shed from the cylinder merged with a vortex from the hydrofoil. They noticed 3 different categories of wakes. In the destructive mode, a vortex created by the hydrofoil is pushed to merge with an opposite sign vortex from the cylinder, resulting in a wake of weaker vortices. In the constructive mode, the merging vortices are rotating in the same direction, creating a wake of stronger vortices. The third, the expanding wake mode, appears when vortices from the foil and the cylinder are not pushed together, but form mushroom shaped vortex pairs that move transversely in flow. Triantafyllou et al [27] describe these interaction modes through efficiency measurements. The destructive interaction mode gives the highest thrust with high efficiency while the constructive mode results in both minimal efficiency and thrust. The expanding wake mode operates with highest efficiency but the thrust produced in this mode is considerably lower than in the

destructive mode. Streitlien et al. [28] modelled the problem of heaving and pitching hydrofoil in a vortex street. The model predicted the highest efficiency and thrust for the destructive interaction mode with phase angles from 0° to 90° , where 0° means the maximum lateral displacement of the hydrofoil towards the vortex in the same streamwise position. These results for the most efficient phase shift angle were later confirmed by Alben [29], [30]. That is however opposite to the phase angle that is used by Kármán gaiting fish [18] and a freely heaving and pitching hydrofoil [25]. Beal et al. [25] have explained that Kármán gaiting fish can't use destructive interaction mode for Kármán gaiting because it would have to act against the hydrodynamic forces in the flow.

1.2 Flow sensing

Similarly to robots operating on the ground or in the air, underwater robots use vision, sonars and inertial measurement units to gather information about their surroundings and self-motion. However, in the underwater environment these sensor can be less useful for providing sufficient data for accurate positioning. With low visibility it is easy to get into a situation where there is not much to benefit from cameras and the sonar feedback can be useless because of the lack of landmarks in the vicinity. The situation is even worse when there are currents disturbing the navigation.

1.2.1 Biological lateral line

Fish have learned to cope with difficulties in the underwater environment as they can sense the flow field around them using their lateral line. The sense of flow comes from neuromasts that are the functional elements of the lateral line. A neuromast itself consists of mechanosensory hair cells that are covered with a gelatinous cupula. The cupula interacts with flow and the drag induced deflection is transmitted to the hair cells. The hair cell's deflection is converted into electrochemical signals that are forwarded to the brain through nerve fibers [8].

There are two types of neuromasts. Superficial neuromasts can be found on the surface of the skin, usually from tens to thousands, depending on the species of the fish. An illustration of lateral line sub-modalities of goldfish (*Carassius auratus*) is shown in Figure 1.4(a), where the placement of superficial neuromasts is marked with black dots. Superficial neuromasts (Figure 1.4(b)) have an elongated shape. Therefore they reach further through the boundary layer, which increases their sensitivity [31]. These neuromasts are mainly sensitive to bulk flow speed and can respond to very gentle flows with speed $1-10 \mu\text{m s}^{-1}$ [32]. Neuromasts have their maximum sensitivity along one axis [33]. So in addition to sensing of flow speed, superficial neuromasts with different polarization axis are grouped together to provide sense of flow direction for fish [34].

The second type of neuromasts are called subepidermal or canal neuromasts (Figure 1.4(c)). These are responsible for the name of the lateral line as the subepidermal canals along the midline and in the head region of the fish are

more visible and were noticed first. In Figure 1.4(a) the canals are shown with brown lines that are covered with white dots, representing canal neuromasts. These neuromasts are situated in the canals below the skin, and each of them measure pressure difference between adjacent points where the canal emerges to the surface of the skin. Canal neuromasts have more hair cells, up to thousand while for superficial neuromasts the number is typically around ten [32]. Being more sensitive they can measure pressure difference with the accuracy in orders of 0.1-1 mPa [32].

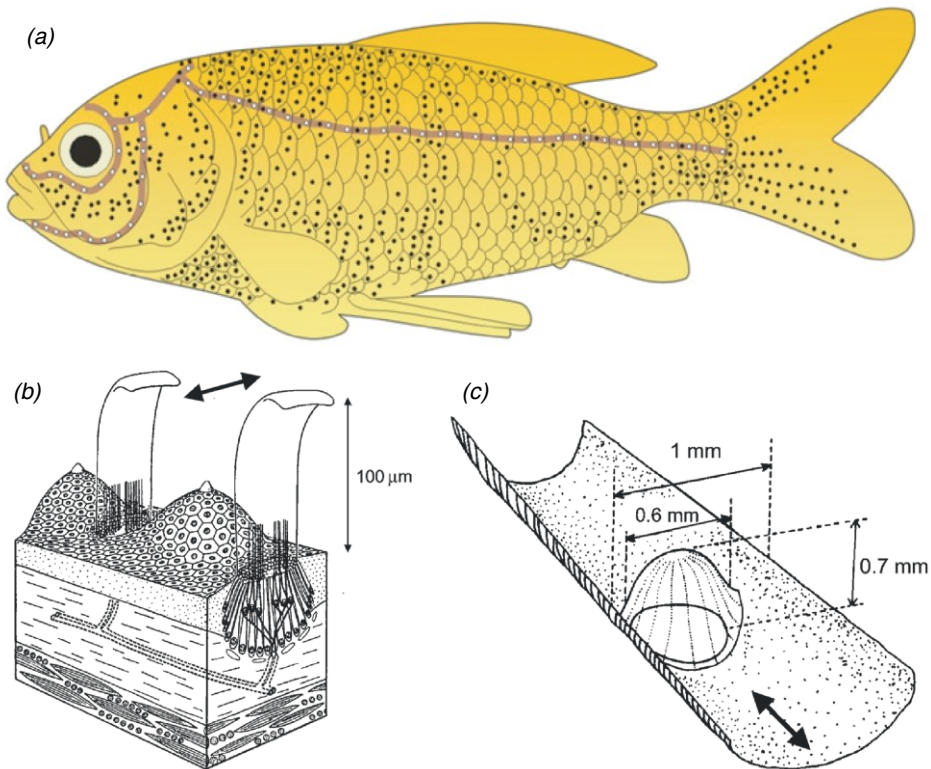


Figure 1.4. (a) Diagram of the lateral line organ of goldfish (*Carassius auratus*), adapted from [35]. Superficial neuromasts are indicated with black dots and canal neuromasts with white dots on brown lines that represent canals. (b) Schematic of superficial neuromasts and (c) schematic of a subepidermal neuromast in a canal, adapted from [32]. The top half of the canal along with the covering skin is not shown. The thick arrows in (b) and (c) indicate the direction of sensitivity of neuromasts.

The two sub-modalities are often used together coupled with vision and inner ear sensing to maximize the perception of the flow field. Fish have found variety of usages where lateral line has a vital role for making decisions or bringing out complex behavioral responses. In order to find out how much the lateral line is being used, biologists have compared fish behaviors in different situations while disabling some of the sensor modalities. For example the rheotactic behavior (behavioral orientation to water currents) is found to be

mediated mainly by the superficial lateral line [36], [37] but with elevated flow velocity these sensors get saturated and lose their ability to sense other hydrodynamic stimuli [38]. The subepidermal neuromasts, however, are not influenced by bulk flow in such a way and preserve their ability to detect a vibration source even with a flow induced background noise [39]. The subepidermal lateral line modality is more sensitive to detecting prey or predators but to complete either of those behaviors fish still needs information about the speed and direction of flow [40]. Other behaviors like schooling [41], object entraining [42], [43] or distant touch mapping of the surroundings [44–48] are similarly making use of both sub-modalities. Disabling either of them will effectively damage the natural behavioral response of the fish.

Fish have different behaviors and they vary even between closely related species. For a more coherent picture fish's behavior needs to be observed in the context of their natural habitation. It has been noticed that the sensitivity of lateral line sub-modalities differ across fish species depending mainly on the conditions of their habitation [49], [50]. Fish that are slow swimmers living in still waters have more superficial neuromasts compared to the closely related species that occupy running waters. High speed swimmers, on the other hand, have more sophisticated canal lateral line system to ensure the survival in running or turbulent waters [49–51].

Another mechanism improving the selective sensitivity is the ability to suppress signals induced by bulk flow or self-motion [52], [53]. Montgomery and Bodznick [54] suggest that fish use adaptive filtering on lateral line sensory signals to cancel sensor stimuli that is coupled with fish's movements to improve their sensitivity to external stimuli.

1.2.2 Artificial flow sensors

The effectiveness of the biological lateral line used by fish has inspired the development of artificial lateral lines with a motivation to give underwater robots an opportunity to tap into the wealth of information available in flow. Several methods like hot-wire anemometry, turbine flow meters, acoustic Doppler-shift velocimetry and particle image velocimetry have been available for a few decades for flow measurements. But sensors for these conventional methods are usually too big and insensitive to be useful on underwater robots [55]. Recent developments in microelectromechanical systems (MEMS) show promise for producing flow sensors comparable with neuromasts, both in size and sensitivity.

Researchers have found several different solutions for producing sensors that either are sensitive to the flow velocity or can measure flow field indirectly through pressure. Some of these sensing methods are mechanically very similar to the hair cells found in a biological lateral line. These are usually flow sensing sensors measuring the change of an electrical resistance in the material that deforms when a cantilever attached to it is deflected by flow [55–57]. An example of a cantilever based resistive flow sensor is shown in Figure 1.5(a). These sensors have been reported to achieve $\sim 7 \text{ mV mm}^{-1} \text{ s}$ sensitivity to water flow but they suffer from the lack of repeatability and robustness. To reinforce

this type of sensors Peleshanko et al. [1] have covered the cantilever structure with a hydrogel cupula. In addition to improved mechanical strength and working range, the sensitivity of the sensor increased due to the suppression of elastic resonance and an extended reach through the boundary layer. Sensitivity threshold of $2.5 \mu\text{m s}^{-1}$ was reported by McConney et al. [2] for a bending cantilever flow sensor covered with a cupula. This sensitivity is in the same order with the sensitivity of biological lateral line sensors.

Similar to piezo-resistive sensors there are also cantilever based strain sensors that measure change in capacity (Figure 1.5(b)). The deflection of the cantilever changes the distance of electrodes on the membrane from the common electrode [58–61]. An advantage of these sensors is that they can be manufactured in densely packed arrays and have a potential to be equally sensitive to tangential flow from any direction. In comparison, the piezo-resistive cantilever based flow sensors are uniaxial and need cluster of multiple sensors to sense directionality [4], [35], [56].

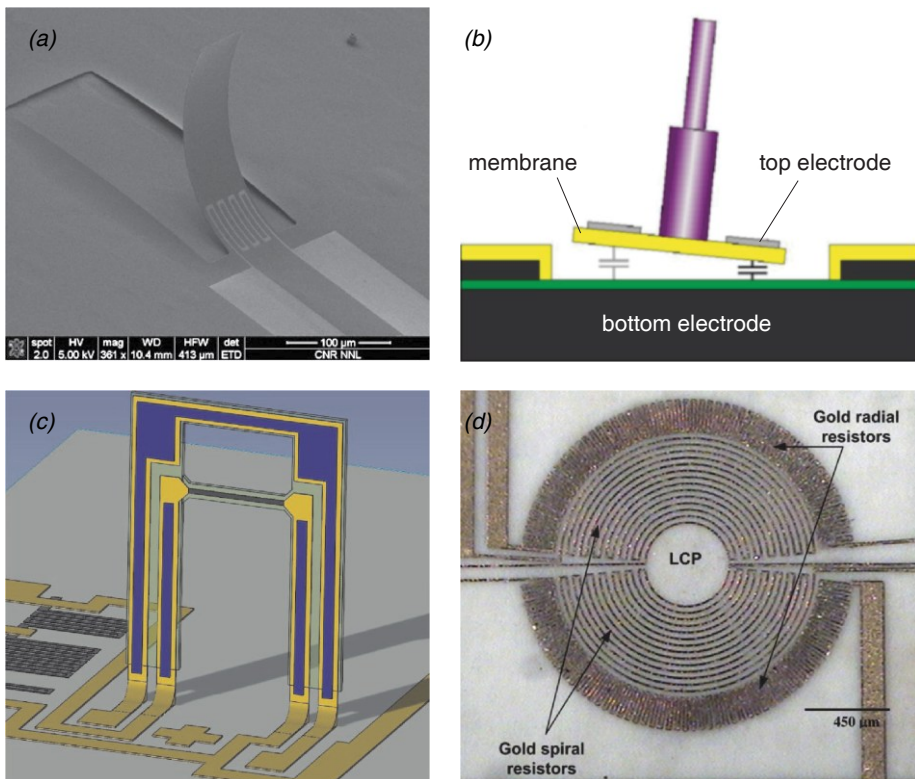


Figure 1.5. MEMS lateral line sensors. (a) Piezo-resistive cantilever-based flow sensor, adapted from [57]. (b) Schematic of the working principle of a capacitive cantilever-based flow sensor, adapted from [62]. (c) Schematic of a hot-wire flow sensor, adapted from [63]. (d) Piezo-resistive membrane based pressure sensor, adapted from [64].

MEMS technology has also advanced hot-wire anemometry sensors reducing the size of a sensing unit (Figure 1.5(c)) and also making it possible to

manufacture them in arrays. For operation of the sensor the hot wire is heated by feeding constant current through it. When the hot-wire element is introduced to the flow it cools the wire down depending on the flow rate and it can be measured as the change of resistance in the heated wire. To measure flow velocity the hot-wire element needs to extend through the boundary layer, making them similar to cantilever based sensors as they are afflicted by the same problems: a complex manufacturing process and a fragile structure [4], [63], [65].

There is another type of sensor that do not need structures extending above the surface and can also be manufactured using MEMS technology. These sensors are based on a piezo-resistive membrane that is deformed under pressure (Figure 1.5(d)). Flow is not affecting these sensors directly as they are level with the surface but the flow field can be estimated from the pressure field. Pressure sensors relate to canal neuromasts on fish but instead of measuring pressure gradient between two points on the surface they can measure pressure with respect to vacuum or an ambient pressure [64], [66].

Pressure sensitive piezo-resistive sensors are also commercially available [67]. These are the sensors we chose for our research, more thorough description of them is given in Chapter 2.2. Although they are less sensitive and they are larger compared to the sensors described above, we chose them because of their robustness and consistent performance between different exemplars. Another feature of these sensors is the standard packaging that made the waterproofing process of an artificial lateral line easier.

1.2.3 Artificial lateral line sensing

With so many different groups putting effort into developing flow sensors, they are making great progress and have demonstrated their achievements by putting their flow sensors through different performance tests. Most of these tests are biologically relevant and the results are often comparable with the performance of the lateral line of marine animals.

The most common benchmark used by sensor developers is the dipole source detection and localization which is similar to fish behavior when they are tracking a prey or hiding from a predator. Pressure waves created by undulating fins of swimming fish can be mimicked well enough with a vibrating sphere to call forth a lateral line mediated feeding response on different fishes [39], [68].

Chen et al. [56] and Peleshako et al. [1] have used a dipole source to quantify a threshold level of sensitivity of a lateral line sensor. Yang et al. [63] demonstrated that a dipole source causes a “Mexican hat” shaped excitation profile over an one-dimensional array of flow sensors. The same result was confirmed later by Yang et al. [35] in 3D when they used cross shape distribution of flow sensors mounted on a cylinder.

Another common biologically relevant test for artificial lateral line sensors is the flow speed measurement [3], [4]. It relates with rheotactic behavior on fishes which has been mimicked in work of Salumäe et al. [69] with a robotic fish that aligns itself with the flow direction based on the feedback from an artificial lateral line. However, usually research groups, developing lateral line

sensors, do not try to implement the biological behavior and show only the response of a single sensor to the flow velocity. These tests may be enough to quantify the sensor's sensitivity but they neglect problems that arise when the sensors are mounted on a moving craft.

An object detection test is another benchmark for flow sensors that has been oversimplified to show if artificial lateral line sensors can detect some object. This test relates to the environment mapping behavior observed in blind Mexican cavefish [70], [71]. This species have no visual sensation but have a well-developed lateral line organ that is used to create a 3D image of its surroundings. For an artificial lateral line, this complex behavior is simplified and approximated with a situation where an object is dragged past an array of sensors that show sequential impulses in their signals [5], [64]. Bouffanais et al. [72] have approached this problem analytically and have suggested a method for building a map of flow environment with a multi-point sensor device.

Another challenge for flow sensing is the detection of turbulent flows and providing information for navigation in them. The task is slightly easier for a Kármán vortex street as it is a periodically turbulent flow regime and thus has predictable features. This phenomenon has been studied thoroughly [73], [74], [75], but little is known about the flow field from the perspective of a fish or an underwater vehicle. Artificial lateral line developers have shown that flow sensors are sensitive enough to detect fluctuations created by alternating vortices [63], [76] but to be able to navigate in a Kármán vortex street the flow sensor measurements need to be related with the structure of the flow regime. First steps in interpreting flow sensor data about a vortex street in the earth frame of reference are presented in [77]. The analysis there is done on particle image velocimetry flow field data to suggest methods for onboard flow characterization.

1.3 Novelty beyond the related work

In this thesis we present the research done with fish inspired artificial lateral line platforms and thus we have described findings and achievements of both biological and artificial lateral lines. In our research we used commercially available miniature pressure sensors because none of the flow sensors in development were ready for use on underwater robots. For more detailed description of these sensors refer to Chapter 2.2. The other flow sensors described in Chapter 1.2.2 may excel with higher sensitivity and smaller size but for underwater robots it is required that they also are reliable and robust in order to get satisfactory results from experiments.

Using these commercially available pressure sensors we investigated three research problems. First we looked how different flows are perceived from the perspective of an underwater robot. This work is extending the research of [77] that estimated fish's sense of flow based on particle image velocimetry data whereas in this thesis we gather flow information by using an underwater sensing platform. In this study we compare Kármán vortex streets with steady

flows and look how different data processing tools can be used to distinguish these flows.

Secondly we investigate how craft's motion data can be used to estimate influence of motion to flow sensor signals. Some behaviors of fish suggest that they use selective filtering on their lateral line signals to cancel out the stimuli that is coupled with self-motion [54]. In our effort to build a similar filter for artificial lateral lines we make use of an analytical model derived in [78] that estimates pressure differences across the front part of a moving streamlined body. Using pressure and motion measurements a model is built that can be used to cancel out the self-motion stimuli in flow sensors data.

Finally we investigate if pressure sensors can be used to synchronize the tail beat of a fishlike robot with vortices in Kármán vortex streets and measure how the synchronization of the tail beat influence thrust and efficiency of the tail fin propulsion. The phenomenon of fish that can save energy with Kármán gaiting swimming mode have been studied thoroughly for past decade [79] but there is still some uncertainty about the role of the lateral line for a Kármán gaiting fish [23]. Meanwhile, it has been shown with hydrofoils that proper timing between a hydrofoil and vortices is essential for increasing efficiency of the propulsion [27]. In previous studies the interaction timing has been tuned by an oscillating cylinder that creates the Kármán vortex street [26]. In our research the vortex synchronization is achieved through artificial lateral line sensing, providing a new method that can be used on underwater robots to increase their swimming efficiency.

2 Materials and methods

This chapter gives an overview of experimental setups, procedures and equipment used for artificial lateral line measurements in steady and turbulent flows. While the research is about fishlike sensing and swimming we decided to use flow tunnels instead of natural waters, as in a flow tunnel the environment is more controllable for data gathering. Altogether three different flow tunnels were used for experiments with lateral line sensors. Two of them are located in University of Bath in UK and one in Centre for Biorobotics in Tallinn University of Technology in Estonia. Henceforth they will be referred as UB1, UB2 and CB1.

We also developed three different artificial lateral line platforms. The first lateral line platform (Platform 1) was a simple craft incorporating two sensing arrays. This platform was made to advance the research of [77] by characterizing Kármán vortex streets from the perspective of a fish. The second platform (Platform 2) is an advancement of the first with its fusiform fishlike body and 3D positioned sensors, covering the head of the platform. The 3D positioning of the sensors on the platform allows to research different flow sensing problems and one of them, presented in this thesis, is a self-motion estimation that can be used to enhance signals of external flow stimuli. The third platform (Platform 3) is an even closer imitation of a fish and in addition to the sensing ability, it can use flow information to control the movement of its tail. This robotic fish was developed to research mechanisms of tail beat synchronization in a Kármán vortex street.

2.1 Requirements for sensing platforms

When we started this research we had little knowledge about different flow features and how they would be felt with artificial lateral line sensors. Thus choosing flow sensors for this research was an experimental procedure driven by task requirements, mostly sensitivity that was required to be sufficient to detect vortices in Kármán vortex streets. When we had found commercial pressure sensors that met this criterion we chose to continue our research with them but at the same time started with development of our own flow sensitive sensors [80] that would supplement or replace the commercial sensors in future. Unfortunately these flow sensitive sensors are still in development as their robustness needs to be improved for the use on underwater robots.

As for flow sensors, there were not many requirements for the lateral line platforms in the beginning and the requirements developed and changed as the work proceeded. Because of that our first artificial lateral line had a modular design, consisting of two pressure sensor arrays that could be assembled into different configurations, allowing us to test different hypothesis and see what improvements this platform needed. In this thesis we present research with one

of the configurations of this artificial lateral line (Platform 1), for detailed description of it refer to Chapter 2.3.

From experiments with Platform 1 we saw that in the electronics design more elaborate methods for the noise suppression were needed as more subtle flow stimuli was often masked with noise from the environment. Secondly we needed to improve the acquisition rate as it would improve accuracy of data processing methods such as frequency analysis and turbulence intensity analysis. From hydrodynamic perspective next sensing platforms needed to be more streamlined to acquire results that are more comparable with the lateral line of a fish. These requirements were fulfilled in the design of Platform 2 described in Chapter 2.4.

After test results with Platform 1 we started to develop another sensing platform (Platform 3) that would also be capable of fin propulsion. While the electronics design of Platform 3 is same as in Platform 1, the improvement is mainly in its shape and actuation. Platform 3 has been designed to research improvement of tailfin propulsion through vortex synchronization in Kármán vortex streets. Before designing Platform 3 we experimented with different compliant tails [81], [82] and saw that in order to use vortices, they need to survive till they have reached to tailfin of the sensing platform. So it was required that the surface of the sensing platform's body would be smooth and continuous even when the tail of the platform is actuated. Secondly it was required that the tailfin of the platform would be flexible enough to react to the forces created by vortices. A detailed description of the sensing platform that meets these criteria is given in Chapter 2.5.

2.2 Lateral line sensors

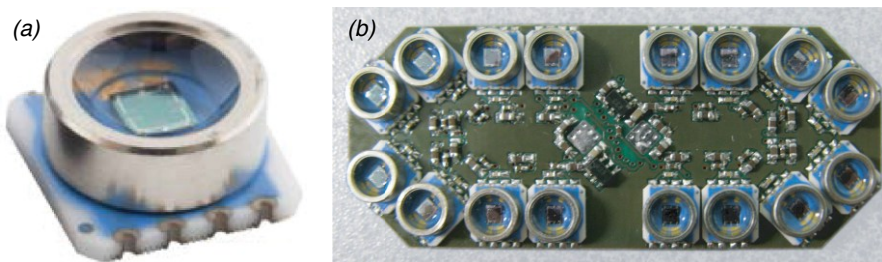


Figure 2.1. (a) MS54XX-AM pressure sensor, adapted from [67]. (b) MS5401-AM pressure sensors mounted on a data acquisition board, assembled for Platform 2.

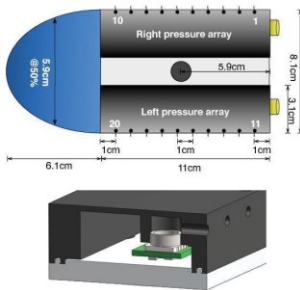
In all three sensing platforms we used the same kind of pressure sensors. When we started with this research we had to find sensors that were small and sensitive enough to be suitable for lateral line sensing. Measurement Specialties TM has developed a series of commercial pressure sensors that are meant to be used in diving watches and other similar devices. These sensors are much bigger than biological neuromasts but for the time being they were the best that could be found to mimic a lateral line mounted on an underwater craft. We

discussed pros and cons of different flow sensors that are developed, including some that are very similar to biological lateral line sensors, but being under development, they all need to be improved before they can be effectively used on an underwater craft. Instead we chose robust and properly packaged commercial pressure sensors, models MS5407-AM and MS5401-AM [67].

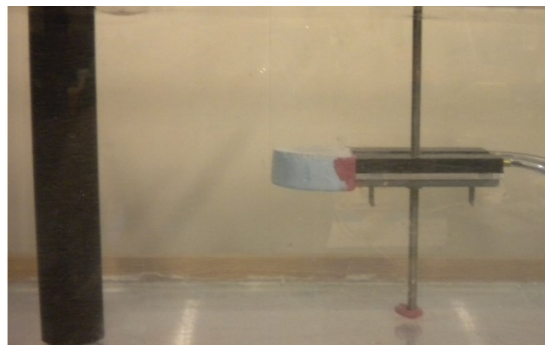
These pressure sensors have a sensing unit that is micromachined from silicon and is mounted on a $6.2\text{ mm} \times 6.4\text{ mm}$ ceramic carrier. Figure 2.1(a) shows a picture of the pressure sensors used in this research. On the ceramic carrier a stainless steel ring is mounted around the sensing unit to make watertight mounting easier. The ring is filled with silicone gel to protect the sensing unit from humidity and water while being easily deformable to mediate pressure changes from the surrounding environment.

The two models of this sensor are identical in terms of packaging but the difference between them is in the measurement range. MS5407-AM is suitable of measuring pressure in the range of 0 to 7 bar and MS5401-AM in the range of 0 to 1 bar. When measuring pressure in water with MS5401-AM there is a risk of going out of the linear measurement range. It is reasonable therefore to use MS5401-AM sensors for low depth experiments as they have 240 mV bar^{-1} sensitivity over sensitivity of 56 mV bar^{-1} for the 7 bar model. The higher sensitivity of a sensor results in less noise in the digitalized signal. These sensors were used with acquisition electronics and were mounted on the sensing platforms to form artificial lateral lines.

2.3 Platform 1



(a) Sensor platform



(b) Snapshot from an experiment

Figure 2.2. (a) A diagram of Platform 1 accommodating two laterally positioned pressure arrays. Below is a cross-section of an array, showing a mounted pressure sensor and a pore that connects it to the environment. (b) A snapshot of the sensor platform tested in a Kármán vortex street

The design of Platform 1 is very simple (Figure 2.2). It consist of two watertight boxes that were mounted on a rectangular aluminum plate. A U-shaped polystyrene section was mounted in the snout of the platform to make it more

streamlined for flow sensing. A 6 mm steel rod, fixed in the middle of the platform, was used to harness the platform in the middle of the water column.

In this design the watertight boxes function as sides of the artificial lateral line. Each of them contains ten pressure sensors along with data acquisition electronics. On one facet, the box has 2 mm pores, one for each pressure sensor to connect them to the surrounding pressure field (Figure 2.2(a)). The boxes were CNC machined to make precise mounting slots for pressure sensors that were tightened in place with silicone grease.

On this platform the MS5407-AM pressure sensors were used. The signal from the sensor's Wheatstone bridge was digitalized without any amplification. Analogue to digital conversion was implemented by using a 22 bit AD converter MCP3553 by Microchip Technology Inc. With the reference voltage 124.5 mV it was possible to achieve an accuracy of ≈ 0.1 Pa for the least significant bit. However, the high noise rate made it irrelevant as the minimum pressure change detectable through the ambient noise was around 1 to 10 Pa. MCP3553 AD converter was chosen because of its small footprint and convenient voltage range but it also limited the digitalized data reading rate to 50 Hz. On the other hand, for quite low data rate this device employs a third order Delta-Sigma modulator and a fourth-order digital decimation filter that along with high oversampling rate minimized the need for any external anti-aliasing filter. To maximize the signal-to-noise ratio, the AD converter was soldered directly on the other side of the PCB opposite to the pressure sensor to achieve the shortest possible wiring for the analog signal. After digitalization, the signal was transmitted over a serial peripheral interface bus to a microcontroller ATmega324 by Atmel Corporation. Data storing was implemented in an external computer coded in LabVIEW (National Instruments, Austin, TX).

2.3.1 Experiments with Platform 1

Platform 1 was meant for stationary pressure field monitoring in both steady and unsteady flows. The experiments were conducted in University of Bath in the flow tunnel UB1. This flow tunnel has a working section with dimensions $100 \times 30 \times 30$ cm³ (length \times width \times height). The upper boundary of the working section is open and inflow and outflow are bounded with collimators. This flow tunnel was built for experiments with live fish but it is also suitable for smaller crafts. The flow tunnel was built to function with a digital particle image velocimetry (DPIV) system. The pictures of flow field are captured using a front-silvered mirror placed at 45° angle to look through the acrylic glass bottom of the tunnel. The DPIV system used in University of Bath consists of a continuous green-light laser (532 nm, Laser Quantum, TSI™), a high speed PCO 1200 hs 177 CCD camera and a synchronizer (TSI™). The DPIV data was used along with pressure measurements from the sensing platform to relate the pressure data with an overhead picture of the flow.

In the experiments we tested 12 different scenarios with Platform 1 in steady and unsteady flow (illustrations of the scenarios are shown in Figure 3.2). With

these experiments we compare Kármán vortex street flow with steady flow to identify how steady flows can be distinguished from Kármán vortex streets.

The flow speed in UB1 flow tunnel was kept at 20 cm s^{-1} for both the steady flow and the Kármán vortex street experiments. The Kármán vortex street was created using a circular cylinder with 4.5 cm diameter. We tested the effect of yaw angle change of the platform with respect to flow orientation. The experiments with clockwise angles 0° , 15° , 30° and 45° were carried out in steady flow and in the Kármán vortex street. In the Kármán vortex street we also tested the effect of the lateral offset from the center of the street with 0 cm , 1 cm , 3 cm , 5 cm and 7 cm offsets to the right. Each of these experiments was performed separately and lasted 4 minutes. During the first and the last minute the platform was kept in still water. The still water pressure level was later used as a reference in pressure data analysis.

2.4 Platform 2

Platform 2 is the more advanced version of Platform 1. An artificial lateral line is mounted on a fish-shaped craft (Figure 2.3) to ensure that the flow fields detected by fish and its replica are similar. Platform 2 can be divided into 3 sections: a sensing head, a watertight middle section and a rigid tail. The most important section is the watertight compartment in the middle, containing 16 pressure sensors and the acquisition electronics. The compartment is machined out of aluminum to shield the acquisition electronics from electromagnetic noise of the environment. The front side of the casing has 2 mm pressure sensing conduits that are connected to pressure taps on the surface of the head with silicone tubing. There are 33 taps that can be either used to be connected to the pressure sensors or left empty. This permits testing lateral lines in different configurations. The head part itself is just a streamlined shell for covering the silicone tubing (Figure 2.3(c)). The cover is manufactured out of polyamide powder, using rapid prototyping, and then finished with a lacquer coating. Rapid prototyping was also used to create a rigid tail that completes the streamlined body.

This lateral line platform was designed for low depth experiments, making it possible to use the MS5401-AM pressure sensors that are meant for 0 to 1 bar measurements. To ensure linear behavior in water, comparative tests against MS5407-AM sensors were carried out, showing 1.2 bar upper limit for the linear working range for MS5401-AM pressure sensors.

When designing the acquisition electronics the noise suppression was taken much more seriously into consideration than in the design of Platform 1. In addition to the electrically shielded case, the PCBs were designed to have shielding layers to separate the digital electronics from the analogue part. Special care was taken when designing the power circuit to provide low noise supply voltage for pressure sensors. An assembled electronics board is shown in Figure 2.1(b).

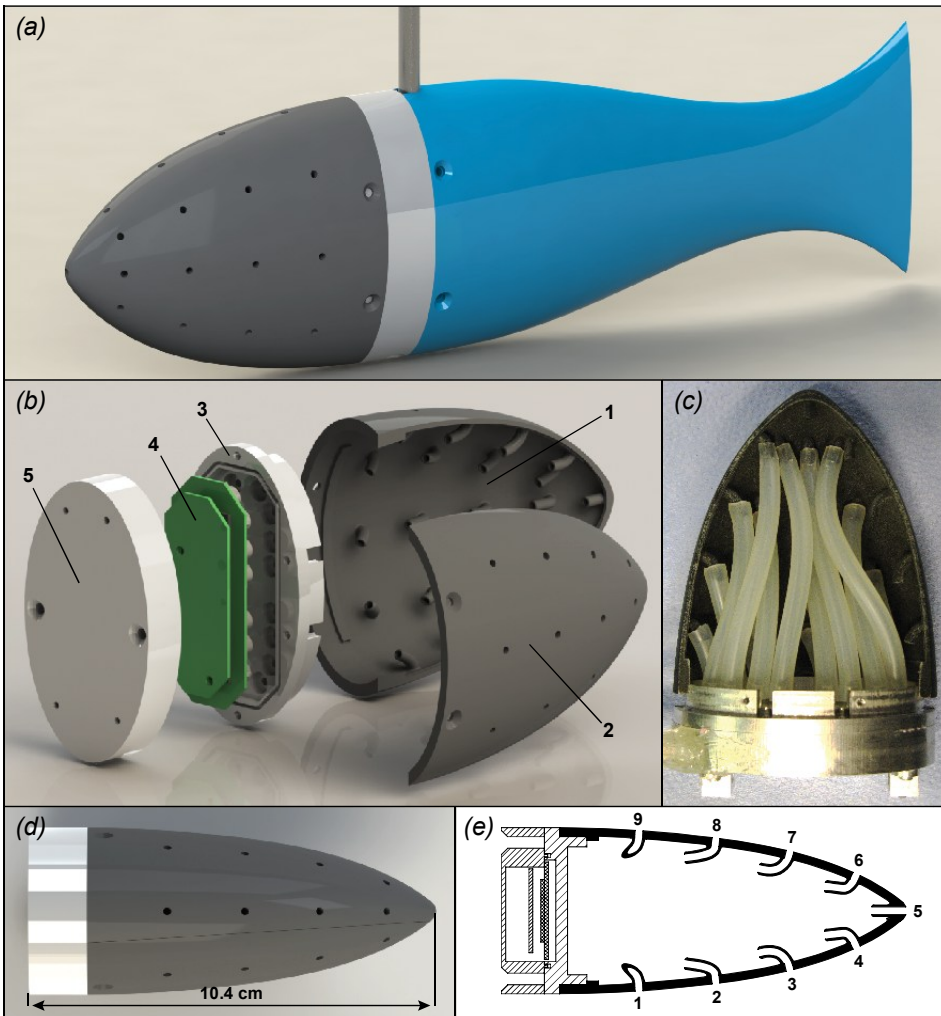


Figure 2.3. (a) A CAD model of Platform 2. (b) An exploded view of Platform 2 where 1 is the left panel of the pressure tapped head, 2 is the right panel of the pressure tapped head, 3 is the front panel of the waterproof housing for the pressure sensors and the electronics, 4 is the circuit boards and 5 is the rear panel of the waterproof housing. (c) A photograph of the inner tubing reaching out from the sensors to the pressure taps. (d) The top view of the fusiform head. (e) A schematic of the cross-section of the pressure tapped head. It shows the tap positions of sensors 1-9.

A diagram of the acquisition process is shown in Figure 2.4. The pressure sensors give out a differential signal that is filtered with a ceramic capacitor between the differential lines, reducing the high frequency noise before transmitting the signal to the amplifier. The signal is amplified 13.67 times with an instrumental amplifier AD8226ARMZ developed by Analog Devices Inc. A single ended signal from the output of the amplifier is sent through a RC filter with the 1 *ms* time constant before sending it for the digitalization. The signal is digitalized using a 16 bit accurate analogue to digital converter

ADS8332IBRGET from Texas Instruments Inc. The digital signal is then passed to microcontroller AT32UC3B1128-AUT (Atmel Corporation) over a serial peripheral interface bus with a sample rate of 10 *k*sps. Within the microcontroller the data was oversampled 50 times and sent to the computer over the RS-232 serial bus with a sample rate of 200 *s*ps. The data was gathered using a custom built code in C#. The amplification and the digitalization of the signal resulted in an accuracy of $\approx 2 Pa$ per least significant bit and the shielding reduced the ambient noise level below that.

At first the amplification stage of the acquisition electronics was designed to shift the measurement range of the pressure sensors in use. The problem with these sensors is that for both 7 *bar* and 1 *bar* model the measurement range below 1 *bar* is never used and thus it reduces the accuracy of digitalization process. However, with some instrumental amplifiers the acquisition range can be shifted so that only a signal in range of 1 *bar* to 1.2 *bar* is digitalized, making the resolution of measurements much greater. Unfortunately, the instrumental amplifier chosen couldn't support such feature, resulting with about 6 times smaller accuracy than planned.

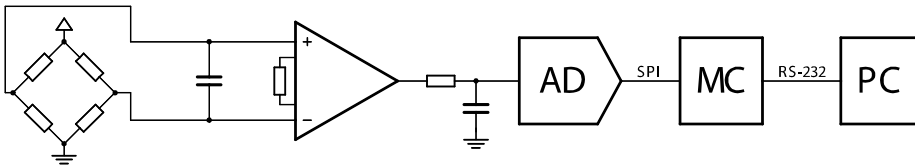


Figure 2.4. A diagram of the pressure data acquisition process in the lateral line electronics of Platform 2.

2.4.1 Experiments with Platform 2

Experiments with the sensor Platform 2 were carried out in the flow tunnel UB2 located in University of Bath. It is similar to UB1, as it has the upper boundary open to the air and also the collimators at the inlet and the outlet of the working section. The size of the working section in UB2 is $93 \times 40 \times 36 \text{ cm}^3$ (length \times width \times height). The same DPIV system that was used with UB1 was also used with UB2, capturing flow images through the acrylic glass wall from below with help of a front silvered mirror.

Platform 2 is suitable for a wider range of research scenarios of hydrodynamic effects but in this thesis we present only the self-motion study. Experiments for this study were conducted to show how the crafts velocity and acceleration affect pressure field around the craft. To move Platform 2 we conducted experiments with a linear motor rig MT480P (Aerotech Inc.). The linear motor rig was mounted above the working section of the UB2 flow tunnel and a manual adjustment of the motion rig's angle in the horizontal plane allowed to choose the movement direction of the motor with respect to the flow direction. The sensing platform was fastened to the motion rig with a 6 *mm* stainless steel rod to reduce flow-induced disturbances. However, the choice of long movement arm resulted in 8 *Hz* small amplitude oscillations of the sensor

platform, but these oscillations, felt by pressure sensors, were filtered out before analyzing the data.

The motor was controlled with a Soloist Motion Controller 3.02 (Aerotech Inc.) that had a computer interface, allowing precision movements along a single translational axis. The controller was capable of recording the position and the velocity data with sample rate 200 *sps*. So the sensing platform didn't swim itself but was moved externally in water. We chose to use oscillatory motion for the experiments as it incorporates both changing speed and acceleration (Figure 2.5). The sensing platform was moved with 12.5 *cm* amplitude and with 0.16 *Hz* frequency in still water and also in steady flows with speeds of 9.2 *cm s⁻¹*, 14.7 *cm s⁻¹*, 18.6 *cm s⁻¹*, 24.1 *cm s⁻¹*, 28 *cm s⁻¹*. Each experiment lasted less than 5 minutes with about 2 minutes of flow data recorded for reference purpose before and after the oscillatory movement. The platform's motion lasted 18.75 *s* in which time it was moved 3 times forward and backward. The oscillation was started by moving the craft forward from the middle position. The pressure data, the DPIV recordings and the motion data were synchronized with a switch that turned on a LED light for the DPIV capture and gave a digital signal to the sensing platform and to the linear motor controller. The synchronization enabled us to find out the relation between the self-motion and the pressure field while the DPIV provided overhead view of the flow structure.

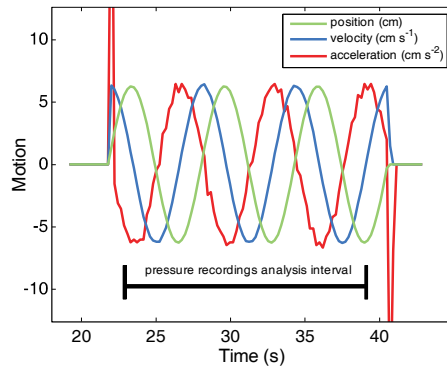


Figure 2.5. The motion data from the linear motor controller. Less than 3 periods of data was used in analysis as we excluded the data that had disturbances in the beginning and in the end of the movement.

2.5 Platform 3

Platform 3 is a fishlike robot (Figure 2.6), designed with a special purpose to test a hypothesis about swimming in Kármán vortex streets. The inspiration for the design of the platform originated from the shape and the swimming kinematics of rainbow trout. Trout was chosen to be an example because of its high swimming speed and acceleration that are characteristic to the body and caudal fin swimmers, especially to the group using the subcarangiform locomotion mode [7], [83], [84]. Subcarangiform swimmers use muscles of the

2/3 of their posterior body to create an undulating wave that is traveling with the speed greater than the resulting swimming speed in the opposite direction.

Instead of using the serial change kinematics to actuate the caudal fin, we decided to imitate the subcarangiform swimming kinematics with the use of a compliant tail that is actuated with a single external motor placed at the 1/3 body length from the nose. The compliant tail reduces the complexity of control algorithms that actuate the tail as opposed to the multi-link design that gives more control over the tail but needs precise manipulation of each link to achieve the desired smooth motion. The robot's compliant tail was casted into a tail-shaped mold using a two-component silicone Dragon Skin (Smooth-On, Inc.). The viscoelastic properties of the tail were tuned to mimic the corresponding properties of rainbow trout by adding 6.2% of Slacker Tactile Mutator additive (Smooth-On, Inc.) into the casting mixture [81], [82]. A backbone of a thin plastic sheet that extended out of the tail to form the rays for tail fin, was casted into the tail. The fin itself was casted separately as a thin membrane from a two-component silicone Elite Double 8 (The Zhermack Group). The design of this compliant tail is a result of a spiral development process that aimed at maximizing the benefit of vortices in a Kármán vortex street.

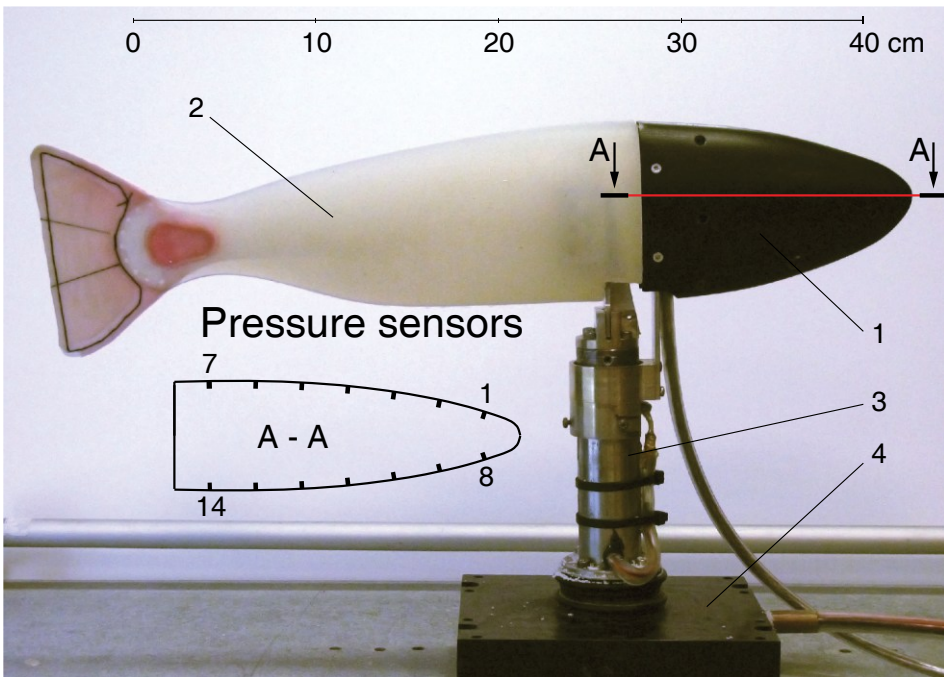


Figure 2.6. Platform 3 for vortex synchronization. 1 – pressure tapped head, pressure sensor positions are shown on a schematic of the cross-section; 2 – compliant tail; 3 – actuator; 4 – force plate.

The propulsive movements were localized at the tail part of Platform 3 by harnessing the head of the robot to the motor's static base. The coupling between the head and the tail was resolved by using stretchable silicon

connection that formed a skin that allowed a fusiform transition between the parts. Performance of the tail fin propulsion was measured with a force measurement system that harnessed the robot to the flow tunnel’s floor. The force measurement system is a custom built device that can measure streamwise and transverse forces on the horizontal plane and also torque around the motor’s axis. The force plate has been calibrated with a force gauge LG-5000A developed by Lutron Electronic Enterprise CO., LTD.

The head part of the robot is rapid prototyped out of polyamide powder and then finished with lacquer coating. The head is assembled from two sides that has a seal in between to create a watertight compartment for pressure sensors and an acquisition electronics. There are 14 pressure sensors in this compartment that are connected to the surrounding environment through taps, arranged in straight lines on both cheeks of the head. The pressure acquisition electronics is similar to the one described in Chapter 2.3, utilizing the MS5407-AM pressure sensors.

2.5.1 Experiments with Platform 3

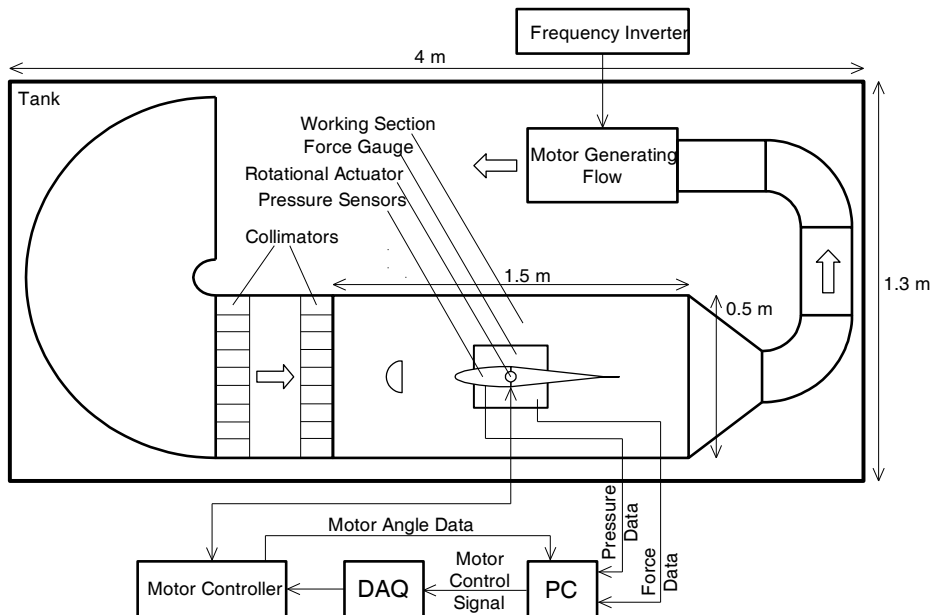


Figure 2.7. A schematic of the CB1 flow tunnel and the experimental setup.

Platform 3 was designed to be used in Kármán vortex streets to enhance the thrust production by synchronizing the tail beat with vortices. The experiments for vortex synchronization were carried out in a flow tunnel located in Centre for Biorobotics in Tallinn University of Technology. The flow tunnel CB1 has a working section with dimensions $150 \times 50 \times 50 \text{ cm}^3$ (length \times width \times height), a schematic of the flow tunnel along with other experimental equipment is shown in Figure 2.7. The flow tunnel has the upper boundary closed with a sheet of transparent acrylic glass that allows to capture DPIV pictures from the above.

The DPIV system used with the tunnel is custom built, using red 808 *nm* wavelength laser diode with 200 *mW* output power [85]. The laser beam is dissipated with a cylindrical lens into a sheet of light that illuminates particles in the flow. The flow images are captured using UI5240HE-M camera developed by IDS Imaging Development Systems GMBH.

The experiments were conducted in a Kármán vortex street that was created with a D-shaped cylinder with a 10 *cm* diameter. The cylinder was placed vertically in the middle of the left and the right wall and 30 *cm* downstream from the collimator at the inlet of the working section. Platform 3 was positioned in the wake of the cylinder, 30 *cm* downstream from the back-side of the cylinder.

The experiments with Platform 3 can be divided into three stages. First, we needed a simple way to prove that the synchronization is affecting the thrust production. The robot's tail was moved with a frequency different from the vortex shedding frequency to show that thrust oscillates with a frequency that corresponds to the difference between the tail beat and the vortex shedding frequency. We used 30 *cm s⁻¹* flow speed to create a vortex street with 0.64 *Hz* shedding frequency and actuated the robot's tail with 0.74 *Hz* frequency to make the thrust production oscillate with 0.1 *Hz* frequency. The same effect can be seen with other frequencies but we chose the tail beat and the shedding frequency close together to produce a low frequency component that can be well distinguished in the frequency analysis.

The next stage was to find the best and the worst phase, in terms of thrust production, between the tail beat and vortices. The experiment was carried out with the same Kármán street conditions as before but the tail beat phase was varied with 30° steps along the entire range from 0° to 360°. Each 3 minutes step of tail movement was preceded by 2 minutes of data gathering with a stationary tail in the neutral position. The data with the stationary tail was used for reference in the thrust calculation.

The last stage consisted of series of experiments for comparison between the thrust production in steady flow and in a Kármán vortex street. We started by measuring the platform's drag in steady flow and used it as a benchmark for the vortex synchronized thrust production. The drag was measured with flow speeds 20 *cm s⁻¹*, 25 *cm s⁻¹*, 30 *cm s⁻¹*, 35 *cm s⁻¹* and 40 *cm s⁻¹*. The thrust production experiments were done with the same flow speeds both in steady flows and in Kármán vortex streets. In steady flows the tail was actuated with the same frequencies as in Kármán vortex streets, where the tail beat frequency was dictated by the vortex shedding frequency. In the Kármán vortex streets there were separate experiments for the best and the worst phase angle (in terms of thrust production). Each phase shift and steady flow experiment at a different flow speed were carried out separately. And to get statistically more relevant results we conducted them in sequences, repeating the same flow speed and phase configuration 5 times. We recorded 4 minutes of data with the tail movement and 4 minutes without at each repetition. Again the data with the stationary tail was used as a reference in the thrust calculations.

2.6 Artificial lateral line calibration and testing

Although the sensors we used are commercially available and have been characterized on the datasheet [67], they still need calibration for the lateral line sensing experiments. From the specification it can be found that in addition to the pressure sensitivity these sensors are subject to light and temperature changes. While the light sensitivity can be overcome simply by covering sensors, the temperature sensitivity is a bigger problem.

2.6.1 Sensitivity to pressure

In the scope of this thesis we have used two different designs of acquisition electronics. The sensing platforms 1 and 3 had their theoretical accuracy $\approx 0.1 Pa$ per least significant bit and Platform 2 had the corresponding value about $2 Pa$. Although the electronics is different, the calibration procedure is the same for all sensing platforms. To find the exact value-unit conversion factor for each sensor we used a change of hydrostatic pressure Δp caused by the change of depth Δh in still water.

$$\Delta p = \rho g \Delta h. \quad (2.1)$$

Here ρ is the density of fresh water at the measured temperature and g is the gravitational acceleration.

The lateral lines were calibrated by alternating between depths that were 10 cm apart and measuring the resulting pressure change. The measurements on the both depths were repeated 5 times. The data was recorded in the single sequence with 5 minutes of data for each change of depth. The value-unit conversion factor was then calculated by dividing the calculated pressure change with the average change in sensor readings.

2.6.2 Sensitivity to temperature

There are two options to handle temperature influence in pressure data. The more elegant option is to design lateral line electronics to accommodate temperature sensors in the close proximity to every pressure sensor, as done in the work of Salumäe et al. [86]. We decided to neglect the temperature effect by letting the sensing platform to stabilize its temperature before every experiment. Unfortunately with this approach the artificial lateral lines still experienced some temperature influence when the flow speed was changed during an experiment. Although the temperature effect was weak as the pressure sensors were not exposed to the flow, it is better to incorporate temperature sensors into a lateral line design to eliminate this problem. It should be considered for any lateral line sensor that uses a resistive sensing element.

2.6.3 Effect of air bubbles in canals

In addition to effects that were stated in the specification of these pressure sensors, we found another one that was caused by the mechanical design of our lateral line systems. The pressure sensors were mounted on all sensing

platforms using the same principle – the sensors were positioned away from the surface to shield them from flow and light, and the pressure around the craft was conveyed to the sensors through canals. However, these canals, having only one open end, do not fill with water when the crafts are submerged and as the air in the canals is compressible, it affects how the pressure changes are perceived from the surface of the craft.

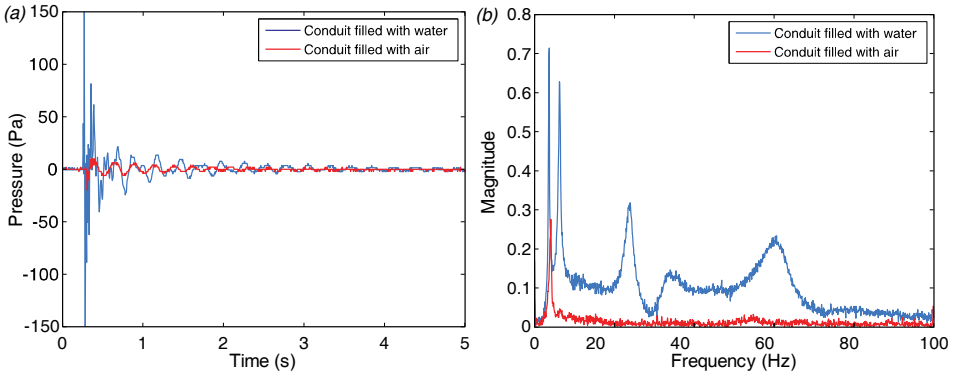


Figure 2.8. (a) Dampened sensitivity of an artificial lateral line sensor, caused by air in the pressure conduit canals. The dampened measurements are compared with an experiment with the conduit canals filled with water. (b) Dampened sensitivity shown in the frequency domain.

Comparative experiments with and without air in the conduit canals show that air in the canals dampens the pressure sensitivity. Figure 2.8 shows pressure measurements from the experiments of a pressure sensing craft that was kicked, creating abating lateral vibrations. The dampened sense of vibration is evident when comparing the sensors readings from canals with and without air bubbles. The canals filled with air reduce sensitivity to pressure fluctuations over 2 times, depending on the frequency of the signal. Thus the experiments presented in the following chapters have been done with the pressure conduits filled with water, ensuring the maximum sensitivity to the pressure field. The canals can be filled using syringe or if the canal system can be taken apart like in case of Platform 2, the air can be removed by assembling the canals while the platform is submerged.

2.7 Flow speed estimation with pressure sensors

As discussed before, fish lateral line organ consists of two sub-modalities. One is mainly responsible for measuring bulk flow speed and the other measures pressure gradient. An artificial lateral line sensing method presented in this thesis is based on pressure sensors which are suitable for sensing flow acceleration and external stimuli like the canal lateral line sensors on fish. However, this artificial lateral line system lacks the flow speed measurement capability so here we present methods to estimate the flow speed based on pressure sensors' data.

2.7.1 Flow speed estimation in steady flow

In irrotational flow, Bernoulli's law ties together pressure and the flow speed, making it possible to predict one through another.

$$p + \frac{\rho v^2}{2} - \rho gh = \text{const.} \quad (2.2)$$

Here p is static pressure that can be measured with pressure sensors while v , in the dynamic pressure term, is the flow velocity at the same measurement point. The third term represents hydrostatic pressure caused by the height h of the fluid column. Bernoulli's law states that the sum of static and dynamic pressure remains constant when measured at the same level of elevation. Writing the Equation (2.2) for two points that are at the same depth gives us:

$$p_1 + \frac{\rho v_1^2}{2} = p_2 + \frac{\rho v_2^2}{2}. \quad (2.3)$$

If one of those points is a stagnation point, the dynamic pressure term disappears as the flow velocity is close to zero at that location, resulting in an Equation (2.4) that makes it possible to estimate the flow velocity from pressure difference between the stagnation point and some freestream location.

$$p_{stag} - p_{fs} = \frac{\rho v_{fs}^2}{2}. \quad (2.4)$$

Objects in flow change the flow around them so it is hard to design an underwater vehicle that can measure freestream pressure directly, however, it can be predicted indirectly based on the pressure profile on a streamlined body. At the most upstream point of the body the flow velocity is zero and when moving along the body the flow velocity increases until at the widest part of the body it is accelerated to maximum, which is higher than the freestream velocity. Because of this continuity, it can be assumed that there is a point between the nose and the widest part of the body where the flow velocity equals with the freestream velocity. Pressure measurements at a location on the body where the flow velocity is equal to the freestream velocity can provide the freestream pressure for use in Equation (2.4) for calculation of the freestream flow speed.

To illustrate it, we have measured pressure with 9 sensors on Platform 2 (Chapter 2.4) in steady flow at 5 different flow speeds. In Figure 2.9(a) the pressure distribution over the streamlined body is shown. We see that for different flow speeds the trend is always the same. Nose sensor senses the highest pressure and the pressure difference with side sensors readings increases as the flow speed grows. It is clearer from Figure 2.9(b) which shows the pressure with respect to the nose sensor's (Sensor 5) value at different flow speeds. Plotting these measurements against the flow speed (Figure 2.9(c)) show that the relationship between the flow speed and the pressure difference is quadratic, as predicted by Bernoulli's law. Figure 2.9(c) shows also the relationship of Equation (2.4) and it is a close match with pressure difference between sensors 5 and 4.

Sensor 4 is not the only sensor that can be used with this method, others that are not in the location of the freestream pressure are just as useful. But for other pressure sensors the pressure difference needs to be compensated. Equation (2.5) shows the compensation for pressure difference where p_1 represents any of the side sensor readings and C_1 is a constant balancing the equation. In Equation (2.5) p_1 can also be an average pressure of all the side sensors. The use of multiple sensors increases accuracy and reliability of this flow speed estimation method.

$$C_1(p_{stag} - p_1) = \frac{\rho v_{fs}^2}{2} \quad (2.5)$$

This method is universal for any steady flow but has one weakness. In order to estimate the flow speed the craft has to be orientated against the flow, as the method requires the nose sensor to measure the stagnation pressure. To get around this restriction, we use another method that does not rely on the pressure measurements at the stagnation point.

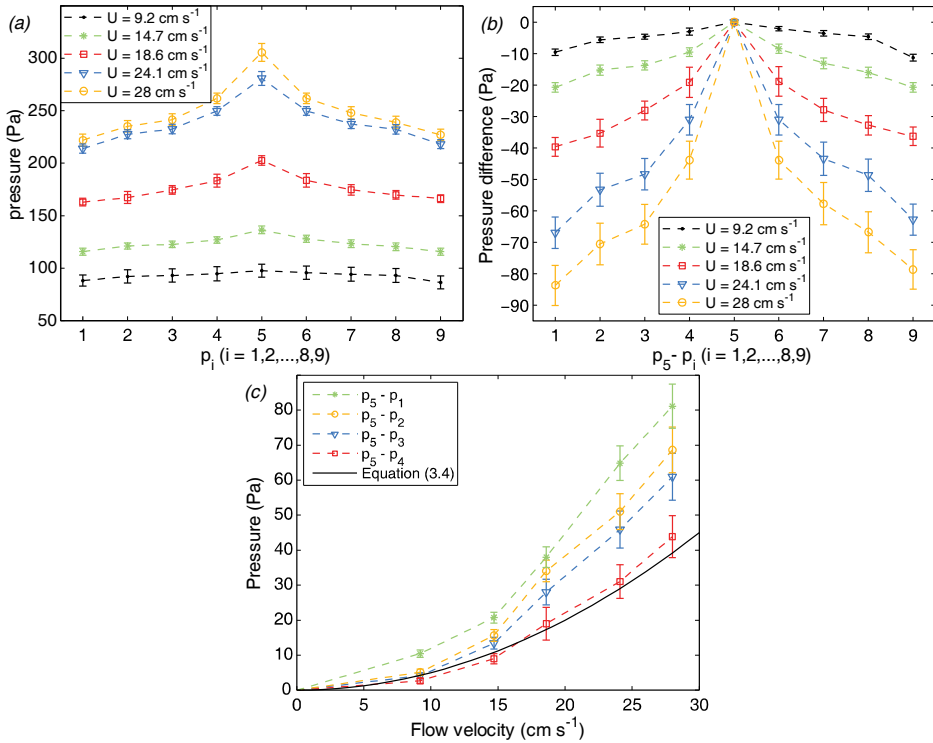


Figure 2.9. (a) Pressure profile measured around the head of the streamlined craft at different flow speeds. (b) The pressure profile presented with respect to the nose sensor's value to eliminate the hydrostatic pressure in the measurements. (c) The relationship between the flow velocity and the pressure difference for different sensors, along with the theoretical prediction from Bernoulli's principle.

We can find the constant in Equation (2.2) experimentally by mapping the relationship between the pressure and the flow speed. Figure 2.10 presents the pressure with respect to the flow speed measured in CB1 flow tunnel as an

average over the side sensors on Platform 3 (Chapter 2.5). Averaging over both sides cancels out the pressure changes that are caused by the change of the orientation in flow. In Figure 2.10 is visible that the relationship between the pressure and the flow speed is quadratic but it is not what we had expected based on Equation (2.2). It is because in a flow tunnel the circulation creates hydrostatic pressure that depends of the flow speed and the relationship is determined by the design of the flow tunnel.

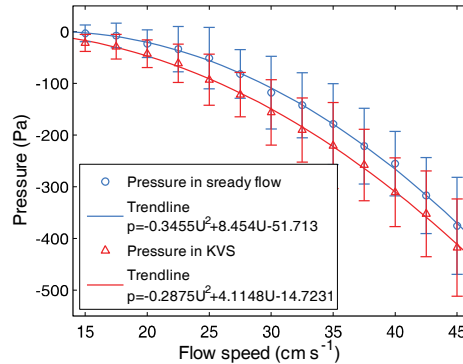


Figure 2.10. The relationship between the flow speed and the hydrostatic pressure in CB1 flow tunnel. The measurements in steady flow and the corresponding trend line is given in blue. The same measurements in a Kármán vortex street are given in red.

This mapping method has both positive and negative aspects. Comparing the pressure changes in Figure 2.9(c) and in Figure 2.10 we see that in the latter case the changes are over 2 times bigger, making the flow speed estimation more accurate. The method doesn't require a pressure reading at the stagnation point and can still give an adequate estimate of the flow speed when the craft is not orientated directly to the flow direction. However, it is also subject to the depth changes that alter the hydrostatic pressure. It is hard to keep a constant depth in natural waters where this extra effort makes the first method more attractive. Thus this mapping method suits better for use in flow tunnels. We are not too concerned about the limits of the method as it is a temporary solution until the miniature flow field sensors are reliable enough to provide the flow sensitive sub-modality for artificial lateral lines.

2.7.2 Flow speed estimation in Kármán vortex street

Bernoulli's law cannot be used for unsteady flows such as Kármán vortex street as the vortices introduce the rotational component in flow. The method using the stagnation pressure is futile in a Kármán vortex street because the vortices are constantly changing the flow and along with it the location of the stagnation point. However, the method, mapping of the flow speeds to pressure change, works also in a Kármán vortex street as shown in Figure 2.10 with red triangles. The hydrostatic pressure is not affected by vortices and the average pressure over several pressure sensors on the both sides of a craft smoothen the local extremes in the signal. However, the mapping method in a Kármán vortex street has the same problems as in steady flow, in a new environment it has to be

recalibrated and the hydrostatic pressure caused by depth needs to be known or kept constant. The effort to make a new mapping for the method can be reduced with an automatic calibration when there is some other method that provides the reference data.

Conveniently, a flow speed estimation method is provided with the periodic nature of a Kármán vortex street. An object in a vortex street is affected by the vortices that change the pressure on the surface of the immersed body periodically. These periodic patterns can be felt with pressure sensors and as the vortices travel downstream the pattern is repeated successively in the signals of the pressure sensors arranged into an array. The vortex traveling velocity can be calculated by dividing the distance between the sensors, given by the lateral line specification, by the traveling time that can be found as a lag between the sensor signals by cross-correlating them [87].

There are several methods to increase the reliability and the accuracy of this method. One option is to add more sensors to the array so that the delay in the signals can be averaged over a higher number of combinations between the sensors. The accuracy of the signal delay measurement increases also with longer distances between the sensors and with a higher sampling rate of the pressure sensors. However, too long intervals between the sensors can also give worse results as the vortices can get distorted over this distance, making the cross-correlation algorithm inaccurate. There is no such problem with increasing the sampling rate of the sensors. The pressure signals can be correlated at smaller time increments, providing more accuracy for the speed calculation while the small intervals between the sensors minimize the vortex distortion.

Conclusion

In this chapter we have discussed how the lateral line platforms were designed and built. We have described this process separately for each platform but actually the development process have been continuous and every new platform supplements the last in order to produce better results.

As we designed new equipment for experiments the requirements for experiments also grew. Experiments had to accommodate different measurement systems and synchronize data between them. Another source for complexity of experiments was the need for reference data acquisition for force and pressure measurements. The reference data was later used in signal analysis to ground the measurements to appropriate levels.

In this chapter we described a method for calibrating the pressure sensors in sensing platforms and discussed measures that needed to be adopted to acquire better flow data. We also describe methods for acquiring flow speed information with an artificial lateral line system that is based on pressure sensors.

In a result we have 3 sensing platforms that allow us to measure flow features from fish perspective. The sensor configurations vary on these

platforms from simple arrays on Platform 1 to 3D sensory system that covers the front part of the fusiform body of Platform 2. Platform 3, however, has been designed to use the flow information as it can move its tail and control its propulsion based on flow features.

3 Pressure sensing lateral line in steady and unsteady flows

Kármán vortex street is a flow condition that is turbulent but at the same time periodic and predictable. Learning to recognize its features by comparing it with steady flow helps the development of control strategies for underwater robots. It is also a suitable condition for learning about biological fish and their flow sensing capabilities. Behaviors of live fish can be very complex and hard to produce in a consistent way but a flow sensing robot mimicking their behaviors could provide useful information about fish.

Kármán vortex street itself has been studied before [73] and it is quite well characterized with velocity field showing vortices as they appear in the horizontal plane from the perspective of an overhead camera. Such images are shown in Figure 3.1, where on the left is steady flow and on the right a Kármán vortex street. It is less known how the vortices are felt by a fish or an underwater vehicle situated in flow.

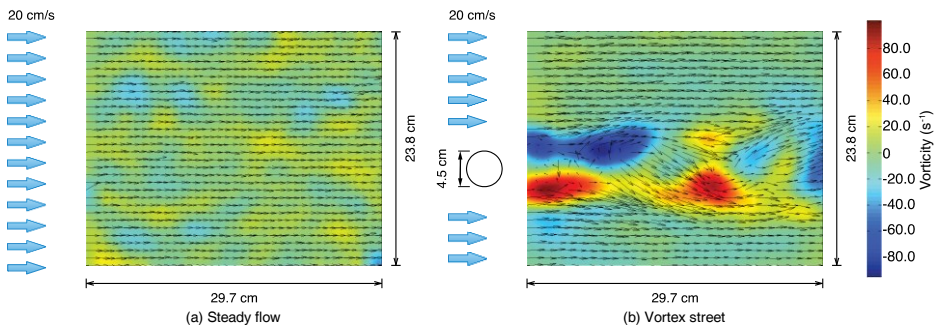


Figure 3.1. DPIV pictures of steady flow (a) and vortex street (b). The vorticity field is shown with a color mapping where blue indicates the clockwise and red the counter-clockwise rotation of the flow. The vorticity field is superimposed with arrows showing the velocity vector field.

The research presented in this chapter is based on results published in [87]. With Platform 1 (Chapter 2.3) we show how a Kármán vortex street is sensed with arrays of pressure sensors while situated in flow. The data about Kármán vortex streets is gathered from 8 scenarios (Figure 3.2(5-12)) which include several lateral offsets and different yaw angles in the wake of a 4.5 cm diameter cylinder. It is compared with data from steady flow at the same 20 cm s^{-1} flow speed (Figure 3.2(1-4)). Using methods that showed promise in analysis of DPIV data [77] we show that spatio-temporal pressure average, average standard deviation over sensor signals and spectral frequency analysis are data processing tools that can achieve following tasks:

- Distinguish between steady flows and Kármán vortex streets.
- Determine sensing platforms orientation with respect to incoming flow.

- Determine sensing platforms lateral deviation from center axis of Kármán vortex street.

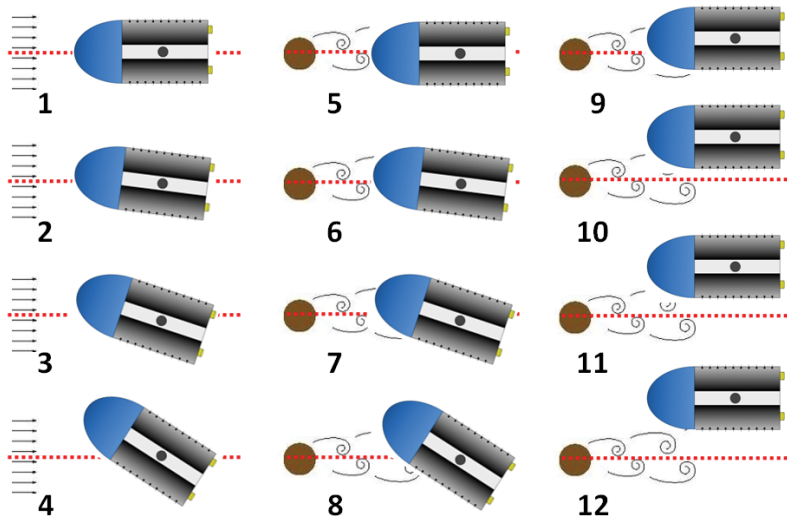


Figure 3.2. Investigated scenarios in steady flow (1–4) and in a Kármán vortex street (5–12). In all experiments the flow speed was 20 cm s^{-1} . A vortex street was generated by placing a 4.5 cm diameter cylinder in the flow. Experiments: 1 - sensor platform aligned parallel to flow (steady flow), 2 - rotated by 15° , 3 - rotated by 30° , 4 - rotated by 45° , 5 - sensor platform aligned parallel to flow (Kármán vortex street), 6 - rotated by 15° , 7 - rotated by 30° , 8 - rotated by 45° , 9 - sensor platform shifted to the right from the center of the Kármán vortex street by 1 cm , 10 - shifted by 3 cm , 11 - shifted by 5 cm and 12 - shifted by 7 cm .

3.1 Characterization of Kármán vortex street

We start with comparison of Experiments 1 and 5 that both have the craft in the default position in the middle of the working section with no lateral or angular offset. The Kármán vortex street is generated with a 4.5 cm cylinder positioned 20 cm upstream from the snout of the craft. In Figure 3.3 the data from the Kármán street experiment and the steady flow experiment has been cascaded. Graph (a) shows the pressure signal from Sensor 5 located in the middle of the right side of the craft. Data is filtered with band-pass filter that removed DC offset and high frequency noise from the signal. The light blue color shows the intervals during the experiments when flow was turned on. In Graph (b) the spatio-temporal average of pressure sensor signals is plotted, the left array is represented by blue circles and the right array by green crosses. The graph shows that flow produces a pressure drop, about 30 Pa , registered both in a Kármán vortex street and in steady flow. The pressure change is caused by the flow circulation and its magnitude is characteristic to the particular flow tunnel

UB1. It is the same hydrostatic pressure dependency that we used before in Chapter 2.7 to predict the flow speed. Unfortunately it cannot be used to differentiate between steady and turbulent flows as it is dependent on the flow speed.

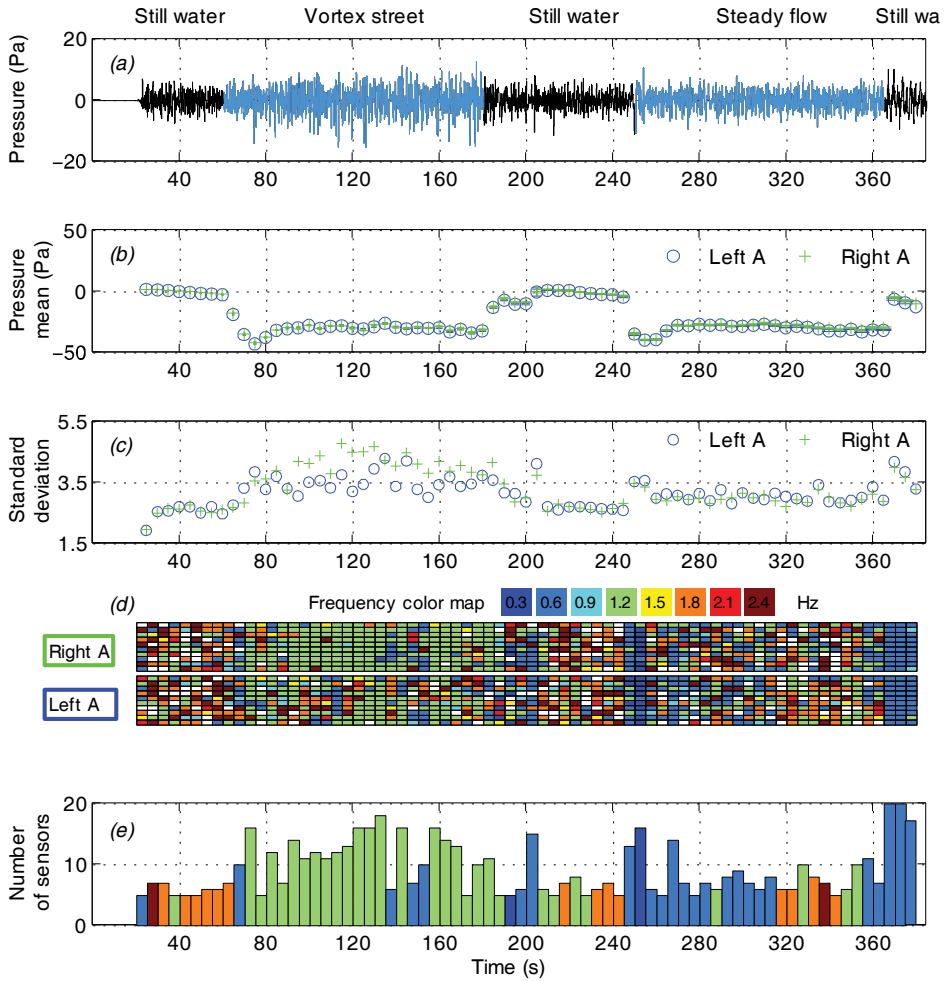


Figure 3.3. Analysis of the pressure readings in a Kármán vortex street ($60 s < t < 180 s$) and in steady flow ($240 s < t < 360 s$). Data were cascaded from Experiments 1 and 5 for illustration purposes. In both flow regimes, the sensor platform was oriented against the flow. (a)–(e): (a) Pressure readings from Sensor 5 (band-pass filtered). (b) Spatio-temporal pressure averages of the right (green) and the left (blue) sensor array. (c) Standard deviation of the pressure signal. (d) Frequency that was sensed dominantly by each sensor. The frequency represented by each color is shown in the key. Green at $1.2 Hz$ is the dominant color/frequency in a vortex street which matched the theoretical vortex shedding frequency. (e) Maximum number of sensors that measured the same frequency. Each data point in (b)–(e) was computed by analyzing the readings over a period of $5 s$.

Returning to the graph (a), there is a noticeable difference in oscillation amplitudes of pressure signals between a Kármán vortex street and steady flow. It is even more evident in Figure 3.3(c), showing the standard deviation with 5 s window, averaged over 10 sensors in each array. In a Kármán vortex street the measurements are about 30% higher than in steady flow, indicating the turbulence of flow. A similar indicator, the turbulence intensity, is used in the velocity field analysis. In calculation of the turbulence intensity the standard deviation is divided by the average flow speed to make the indicator independent of flow speed. The experiments presented in this chapter were all conducted at the same flow speed, therefore the compensation was unnecessary and we used the standard deviation, averaged over sensors in one array, to measure the turbulence of flows.

Using the standard deviation to characterize flows, we saw that in a Kármán vortex street there are fluctuations in the pressure signal. When analyzed further with the Fourier' transform we found that the fluctuations are periodic. Figure 3.3(d) shows color coded dominant frequencies for each pressure sensor and Figure 3.3(e) indicates the number of sensors agreeing on the same dominant frequency. In steady flow the dominant frequencies were very different and in constant flux while in a Kármán vortex street most of the sensors were in consensus at 1.2 ± 0.3 Hz frequency which is the vortex shedding frequency of a Kármán vortex street.

This analysis resulted in definition of empirical thresholds for the standard deviation and the frequency analysis that distinguish a Kármán vortex street from steady flow in our experiments. Flow is classified as turbulent when the standard deviation is over 3.2 and steady when below, but this particular level is appropriate only for the given experimental setup. For the frequency analysis we determined that the sensor platform is in a Kármán vortex street when most of the sensors (more than 50%) detect the same dominant frequency.

3.1.1 Yaw angle offset in a vortex street and in steady flow

Continuing with the comparison of a vortex street and steady flow, we investigate how a change of a yaw angle affect the pressure signal, the standard deviation and the consensus on the dominant frequency by using data from the experiments 1-8. Each data point in following figures represent data from one of these experiments, using 120 s of data to average over an array of 10 pressure sensors.

Figure 3.4(a) and (b) plot the spatio-temporal pressure averages of the left and the right array from the experiments with different yaw angles of the platform in steady flow and in a vortex street. First, the platform was facing towards the flow (0° angle) and the angle was increased by turning the platform clockwise with 15° increments up to 45° angle. Blue circles in the graphs represent the left array and green crosses the right array while the pressure difference between the arrays is shown with black squares.

With the increase in the yaw angle the pressure difference in both flow regimes increased and was slightly larger in a vortex street. Looking at the average pressures on the arrays separately reveals a better distinction between

steady flow and a vortex street. In steady flow the side that was turned towards the flow (the left array) experienced the increase of pressure as the stagnation point was shifted towards the left side. Pressure on the other side (the right array) of the craft stayed unchanged as the flow separation occurred downstream from the pressure sensors. In a Kármán vortex street the pressure was changing on the downstream side of the craft (the right array), decreasing while the yaw angle was increased, and the average pressure on the left array (facing upstream) remained constant.

This result is hard to use for differencing between the flow regimes as it would require a reference measurement to know if the pressure increases on one side or drops on the opposite side. However, the knowledge that in both regimes the pressure is higher on the side that is turned against the flow gives assurance that simple rheotactic controller can be used both in steady flow and in a Kármán vortex street to get a bearing with respect to flow direction.

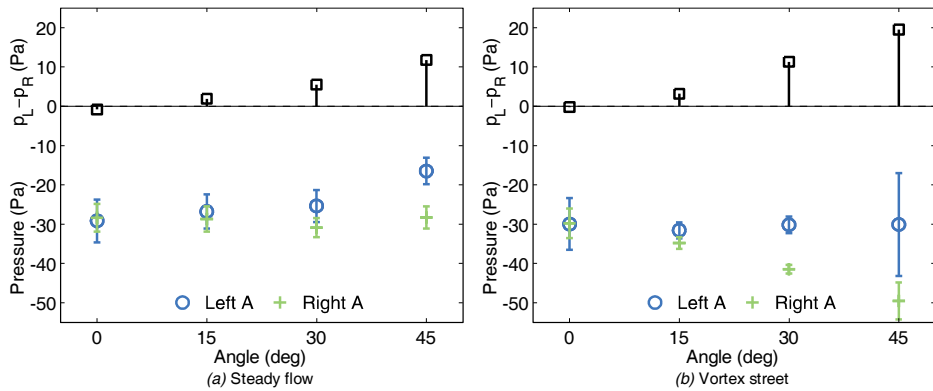


Figure 3.4. Spatio-temporal pressure averages of the right (p_R)/left (p_L) sensor array, where 0 Pa line shows the pressure in still water. Pressure differences ($p_R - p_L$) are shown on top. Each data point was computed based on 120 s long data sets obtained from experiments 1 to 8.

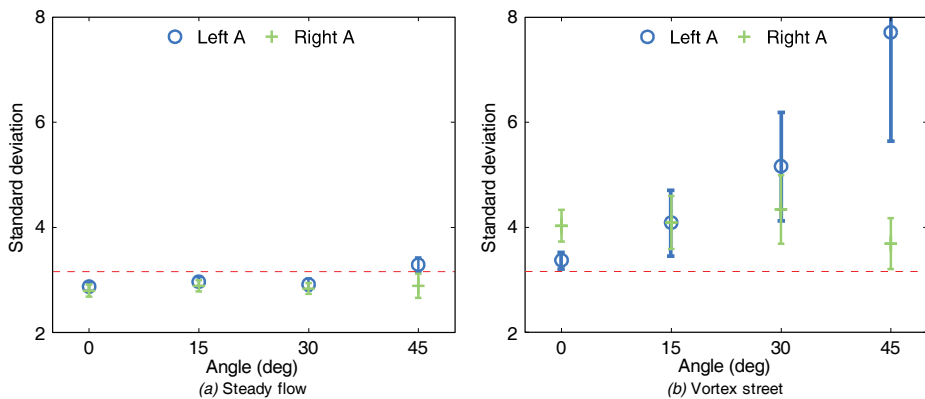


Figure 3.5. Average standard deviation of the right/left pressure array. The red-dashed line marks an empirical threshold level that distinguishes steady flow from turbulent flow.

In Figure 3.3(c) we saw that the standard deviation is minimal in steady flow when the craft is oriented against the flow. In Figure 3.5(a) we see that it changes little even when the craft is at an angle with respect to the flow axis, the increase of the standard deviation of the pressure signal of the left array is barely noticeable at the 45° yaw angle. Changes of the standard deviation are more extreme in a Kármán vortex street where it increases over two times for the left array at the 45° angle with respect to the flow direction (Figure 3.5(b)). It suggests that turbulence can be detected better with pressure sensors that are positioned on the surface perpendicular to the flow direction.

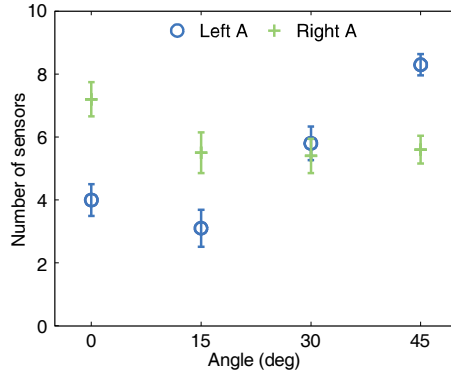


Figure 3.6. Number of sensors detecting the vortex shedding frequency as a function of yaw angle

Pressure sensors' positioning at steeper angles with respect to the flow direction also enhances the detection of the vortex shedding frequency. Figure 3.6 shows that over 80% of sensors in the left array detected the same dominant frequency when the craft's yaw angle was turned to 45° with respect to flow.

Data from experiment with 0° angle suggest that the platform had a lateral offset with the cylinder, causing some imbalance between the left and the right sensor array. On account of which the sensors in the right array had the maximum agreement when the platform was aligned with the flow direction. The increase of the angle decreased the consensus of the right array about 20 percent points, while still maintaining the above 50% agreement when facing downstream with the platform's angle turned to 45°.

3.1.2 Lateral offset in Kármán vortex street

Now that we know how to distinguish a Kármán vortex street from steady flow we investigate how the average pressure, the standard deviation and the detection of vortex shedding frequency behave in the transition zone between the two. The experiments 5 and 9-12 with increasing offsets from the center of the Kármán vortex street are analyzed. The spatio-temporal average of pressure, the standard deviation and the detection of the vortex shedding frequency is shown accordingly in Figure 3.7(a), (b) and (c).

Previously we had steady flow and Kármán vortex street data from separate experiments and when comparing the average pressures we saw that the

pressure dropped 30 Pa in both flow regimes, compared to the pressure in still water (Figure 3.3(b)). Now we investigate data from the same Kármán vortex street but with the sensing platform moved incrementally away from the center of the Kármán vortex street. In Figure 3.7(a) the pressure drops another 30 Pa when the craft is moved into the steady flow region near the right wall of the flow tunnel. This pressure drop comes from accelerated flow on the sides of a Kármán street. The difference between steady flow, we had before, and the steady region at the edge of the Kármán vortex street is that the cylinder reduces the cross-section of the flow tunnel and makes the flow on both sides of it to go faster than the freestream flow. The effect continues downstream, balancing the slower flow region in the wake of the cylinder. It is more noticeable in flow tunnels where a cylinder can block a considerable area from the cross-section of a working section. But even in open waters we can expect a pressure drop just before entering a Kármán vortex street.

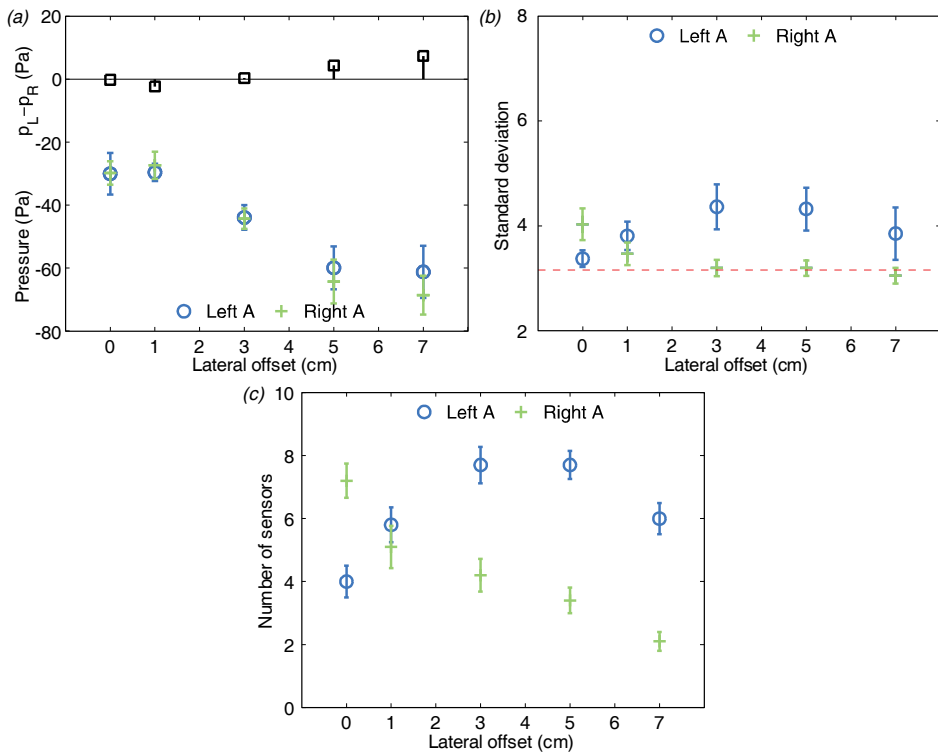


Figure 3.7. Lateral offsets in a Kármán vortex street. (a) Spatio-temporal pressure averages of the sensor arrays, including pressure differences ($p_R - p_L$) on top. 0 Pa line indicate the pressure in still water. (b) Standard deviation of the pressure data. The red-dashed line marks an empirical threshold level that is used to distinguish steady flow from turbulent flow. (c) Number of sensors detecting the vortex shedding frequency.

The standard deviation of the pressure readings, plotted in Figure 3.7(b), show that the offset of 3 cm was enough to have the right sensor array out of the vortex street. The further increase of the offset had no effect to the standard

deviation that remained near the threshold level of steady flow. However, the standard deviation of the left array first increased and then declined, indicating the center of the Kármán vortex street with a peak at the offset of 3 *cm*. With offsets 5 *cm* and 7 *cm* the standard deviation decreased but stayed above the threshold level, indicating the influence of turbulence.

A quite similar behavior can be noticed with the detection of the vortex shedding frequency. In Figure 3.7(c) the number of sensors agreeing on the same dominant frequency decreases below 50% with a lateral offset of 3 *cm*. Here the value continues falling with an increase of the lateral offset, resulting in only 2 sensors detecting the same frequency at 7 *cm* offset. The dominant frequency detection of the left array first climbed and then fell with greater offsets, just like the standard deviation in Figure 3.7(b). The maximum agreement between the sensors of the left array was almost 80% with offsets 3 *cm* and 5 *cm*.

The data analysis shows that the transition between steady and turbulent flows is continuous and that the side closer to a Kármán vortex street detects the cues of it earlier. In that respect, it is reasonable to pay more attention to sensors that are on the side that leads when making transverse movements.

Conclusion

Typically, flows are visualized in the earth frame of reference but autonomous robots can't perceive flow from that perspective. Instead they can be equipped with an artificial lateral line that gives information about the immediate flow field around them. In this chapter we used the spatio-temporal pressure average, the standard deviation and the agreement on dominant frequency between the sensors to investigate differences between steady flows and Kármán vortex streets.

We discovered that the spatio-temporal pressure average over the sensors on the sides of the craft is not very useful for distinguishing a Kármán vortex street from steady flows. However, the experiments with the craft's yaw angle at 45° with respect to the flow direction indicated that sensors in positions where the craft's surface is more perpendicular to the flow can detect the difference. A pressure sensor positioned in such a way would experience an increase of pressure in steady flows and a decrease of pressure in Kármán vortex streets, when compared to the pressure in still water. It shows that an underwater robot should also have pressure sensors positioned in the snout of the craft to take advantage of this simple indicator.

The standard deviation was effective in detecting turbulent flows even when used on sensors positioned on the sides of a craft. However, with a steeper angle with respect to flow the value of the standard deviation increased, suggesting that sensors positioned in the snout of a craft can be more sensitive for turbulence.

The standard deviation indicates fluctuations in the flow but it does not conclusively determine that the surrounding flow is a Kármán vortex street.

Kármán vortex streets are periodic and to be sure that the surrounding flow is not just any turbulence, a frequency analysis should be conducted. We have determined that there is a high probability for a Kármán vortex street when over 50% of sensors agree upon the same dominant frequency.

Using the spatio-temporal pressure average, the spatial average of standard deviation and the sensor agreement on dominant frequency we were able to distinguish between steady flow and a Kármán vortex street, determine sensor platforms orientation with respect to incoming flow and estimate sensor platform's lateral deviation in a Kármán vortex street. Although the data analysis was done on offline data the data processing tools we presented can also be adjusted for the online usage. The standard deviation and the frequency analysis lose their accuracy with a reduction of the sample size but they are still useful for the first estimation in search for flow features. In a real time data processing a more elaborate and time consuming analysis should be done only when less expensive tools give positive results.

4 Sensing self-motion with artificial lateral line

As the flow sensors are developed their performance is measured based on hydrodynamic test that show sensors sensitivity, but those tests in controlled environments are still a long way from situations fish experience in natural environments in terms of their complexity. One of the modifiers that make the extraction of the flow information harder is self-motion sensed by an artificial lateral line. Motion alters the flow field by superimposing external flow signals with the signals mediated by the velocity and acceleration of the vehicle. Artificial lateral lines are usually tested in a controlled environment with a stationary sensor platform exposed to external stimuli. However, before underwater vehicles can rely on flow sensors a method is needed that can separate the self-induced signals from external stimuli.

The research presented in this chapter is based on results published in [88]. Here we investigate how an artificial pressure sensing lateral line is affected by the movement of the sensing platform. The fusiform sensing platform described in Chapter 2.4 was moved externally forward and backward in a sinusoidal pattern. The effect of motion on pressure sensor signals was recorded both in still water and in steady flow. We used data from 9 pressure sensors along with movement data to build a model describing their relationship. The model was then used to predict the pressure changes caused by the platform's velocity and acceleration.

4.1 Forward and backward motion of the craft

In this section we concentrate on the relationship between pressure field and the velocity field around the fusiform craft (Figure 2.3) that is moved harmonically in x-direction with a frequency of 0.16 Hz and with an amplitude of 12.5 cm . The same movement sequence was repeated in still water and in steady flow with 18.6 cm s^{-1} flow velocity. As the x position of the craft was changed as a sinusoidal function of time, the velocity and acceleration were also sinusoidal functions with 90° phase shift (Figure 4.1(a)).

In still water experiments the pressure field changed in phase with acceleration. Vertical lines in Figure 4.1-left help to notice the phase match between the acceleration and pressure signals. In Figure 4.1-left(b) it is visible that the acceleration of the craft is felt strongest by the Sensor 5 positioned in the nose of the craft. The influence to the pressure field decreases with the distance from the nose as the surface of the fusiform platform curves and is almost parallel with the direction of motion in locations of Sensor 1 and Sensor 9 (the sensors furthest away from the nose). The amplitude of the pressure differences between the adjacent sensors in Figure 4.1-left (d) is the same for every sensor pair along the sides, suggesting that the pressure dependency from the acceleration decreases gradually along the surface of the fusiform head.

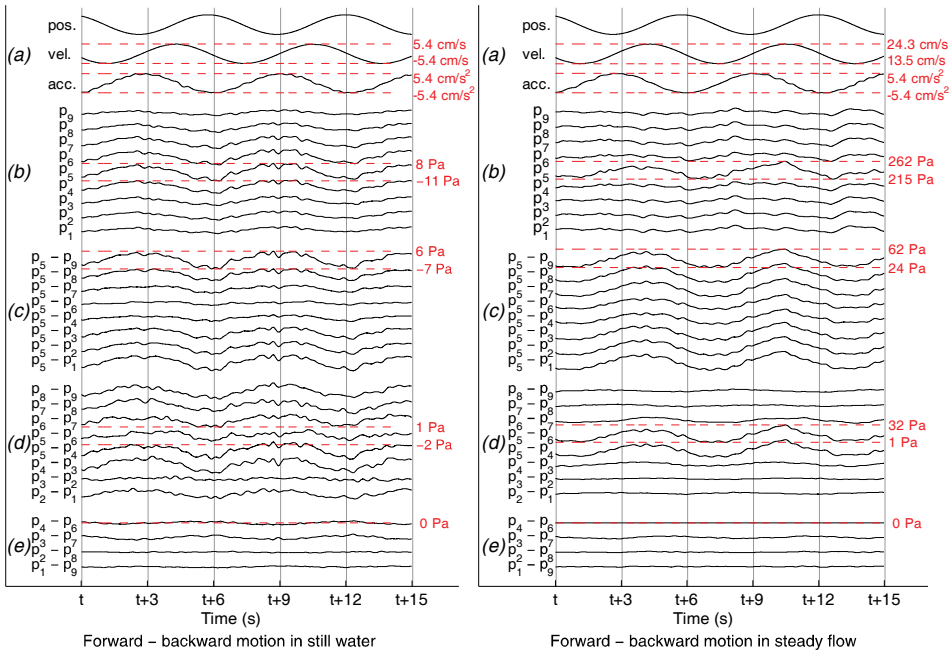


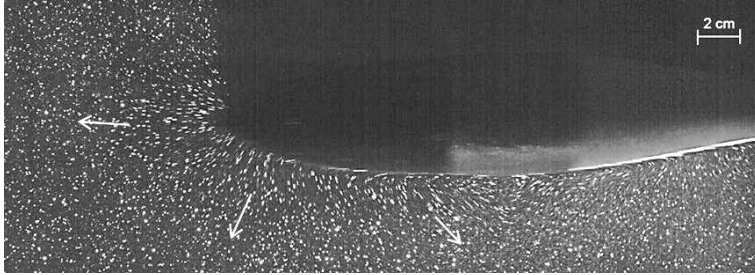
Figure 4.1. Forward –backward motion in still water (left) and in 18.6 cm s^{-1} steady flow (right). In both diagrams (a) shows crafts motion data, (b) displays pressure data captured with 9 pressure sensors synchronized with motion data. (c) shows the pressure difference with respect to Sensor 5 in the nose, and (d) is the pressure difference between adjacent sensors (pressure gradient). (e) is the pressure difference between sensors on the opposite sides of the fusiform head.

In steady flow (Figure 4.1-right) the effect of the acceleration to the pressure field is minimal and pressure sensor signals change more in phase with the velocity of the craft. Again the motion is felt strongest by the sensor in the nose but in steady flow the pressure gradient from the nose decreases much more rapidly (Figure 4.1-right (d)). The amplitude of the pressure differences p_4-p_3 and p_6-p_7 are much smaller compared to the pressure differences between Sensor 5 in the nose and Sensor 4 and Sensor 6 adjacent to it.

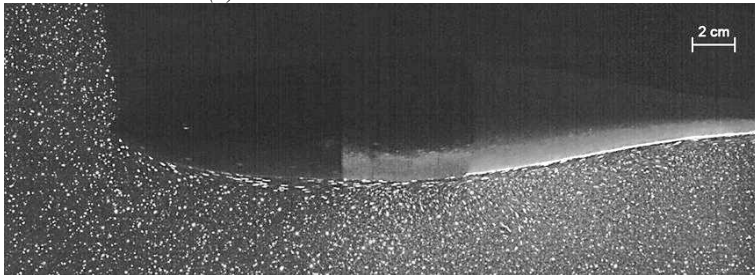
Both in still water and in steady flow the pressure differences between the sides resulted in minimal oscillation and no offset (Figure 4.1(e)), which was expected as the craft and the flow moved only in the x-direction.

To get a better understanding of the flow field around the moving craft, the experiments were recorded with a DPIV setup. Images were captured with long exposure time settings, so that the illuminated particles left tracks, indicating the velocity of the fluid. Figure 4.2(a)–(c) shows the craft movement in still water. In Figure 4.2(a) the craft is moved forward and the streaklines show how the fluid is pushed forward and sideways. In Figure 4.2(b) the craft has stopped and is reversing the motion. Particles on the side of the craft indicate that the fluid carried within the boundary layer still has some momentum and is moving forward, creating a pressure drop. In Figure 4.2(c) the craft is moving

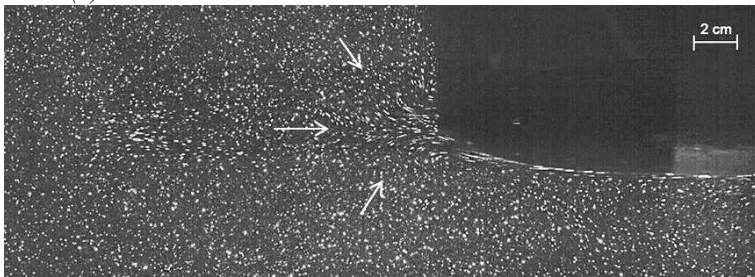
backwards, sucking the fluid in to fill the volume left void in the wake of the retreating craft.



(a) Forward motion in still water



(b) In between forward and backward motion in still water



(c) Backward motion in still water



(d) Forward - backward motion in steady flow 18.6 cm s^{-1}

Figure 4.2. Flow visualization of the craft moving forward and backward in still water (a)–(c) and in the steady flow (d).

In Figure 4.2(d), craft's motion in steady flow is shown. The flow speed ($U = 18.6 \text{ cm s}^{-1}$) was over 2 times higher compared to the highest speed of the craft. Even though Figure 4.1-right indicated that the pressure changes were

caused by velocity oscillations, the craft's forward and backward motion could not be distinguished from the streaklines.

4.2 Theoretical model

As the movement of the sensor platform was limited to only one dimension along the x-direction, the velocity of the craft U can be defined as the rate of change in position along the x direction,

$$U = \frac{dx_0}{dt}. \quad (4.1)$$

Lighthill discussed in [78] that in irrotational flow and with no boundary layer effects, the pressure distribution on the surface of a streamlined body can be approximated by the Bernoulli's equation,

$$P = -\rho \frac{\partial \phi}{\partial t} - \frac{1}{2} \rho |\text{grad} \phi|^2, \quad (4.2)$$

where P is the pressure distribution without the hydrostatic pressure component. ρ is the density of water and ϕ is the velocity potential that can be given by

$$\phi = U \phi_x(x - x_0, y - y_0, z) \quad (4.3)$$

where ϕ_x is the velocity potential in terms of position relative to (x_0, y_0) , associated with the sensing platform's movement at unit velocity in the x-direction (Figure 4.3).

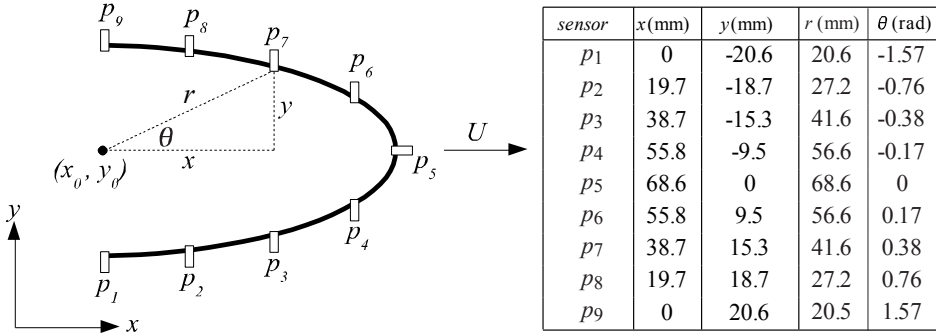


Figure 4.3. Distribution of nine pressure sensors around the head. U is the velocity of the craft in the x direction, with positive value indicating forward motion. The position of each sensor both in the Cartesian and polar coordinates is given in the table.

To derive $\frac{\partial \phi}{\partial t}$ in the first term of Equation (4.2) both velocity U and its rate of change need to be accounted, which gives us

$$\frac{\partial \phi}{\partial t} = \frac{dU}{dt} \phi_x - U^2 \frac{\partial \phi_x}{\partial x}. \quad (4.4)$$

Deriving also the velocity field gradient through ϕ_x we get

$$|\text{grad}\phi|^2 = |U\text{grad}\phi_x|^2 = U^2 \left(\frac{\partial\phi_x}{\partial x} \frac{\partial\phi_x}{\partial x} + \frac{\partial\phi_x}{\partial y} \frac{\partial\phi_x}{\partial y} + \frac{\partial\phi_x}{\partial z} \frac{\partial\phi_x}{\partial z} \right). \quad (4.5)$$

Now Equation (4.2) together with Equation (4.4) and (4.5) gives

$$P = -\rho \frac{dU}{dt} \phi_x - \frac{1}{2} \rho U^2 \left(\frac{\partial\phi_x}{\partial x} \frac{\partial\phi_x}{\partial x} + \frac{\partial\phi_x}{\partial y} \frac{\partial\phi_x}{\partial y} + \frac{\partial\phi_x}{\partial z} \frac{\partial\phi_x}{\partial z} - 2 \frac{\partial\phi_x}{\partial x} \right). \quad (4.6)$$

Equation (4.6) can be represented in the form of

$$P = C_1 \frac{dU}{dt} + C_2 U^2 + C_3 \quad (4.7)$$

where

$$C_1 = -\rho \phi_x, \quad (4.8)$$

$$C_2 = -\frac{1}{2} \rho \left(\frac{\partial\phi_x}{\partial x} \frac{\partial\phi_x}{\partial x} + \frac{\partial\phi_x}{\partial y} \frac{\partial\phi_x}{\partial y} + \frac{\partial\phi_x}{\partial z} \frac{\partial\phi_x}{\partial z} - 2 \frac{\partial\phi_x}{\partial x} \right). \quad (4.9)$$

The first term characterizes the acceleration of the craft and the second term is related to the square of the relative velocity of the flow and the craft. The coefficients $C1$ and $C2$ depend on the geometry of the craft and the term $C3$ is incorporated into the model to account for any other relations which we were unaware of. An analytical solution for this equation can be very complex depending of the shape of the craft, so we decided to find the coefficients by using experimental measurements from artificial lateral line sensors.

4.3 Mapping motion to pressure sensing

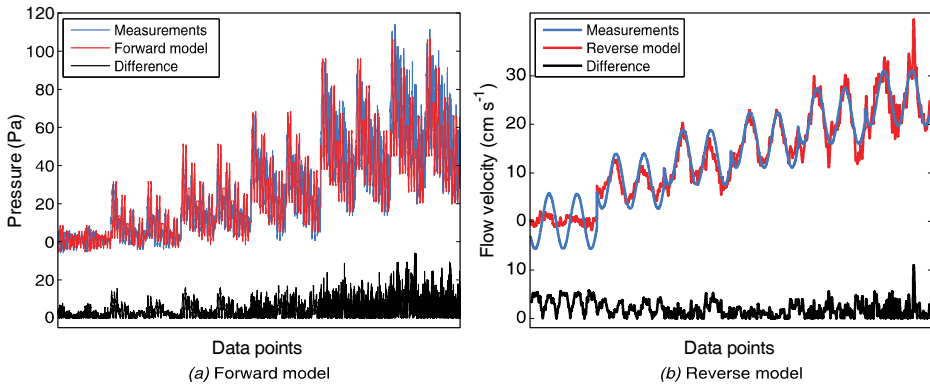


Figure 4.4. (a) Comparison of the forward model with the measured pressure data. (b) Comparison of the reverse model with the measured flow velocity. In both graphs data is cascaded from experiments with 6 different flow speeds, where the leftmost dataset is from still water and the rightmost dataset from 28 cm s^{-1} flow. The real measurements are overlaid with the predictions generated by the forward model detailed in Equation (4.10) and the reverse model detailed in Equation (4.13). The difference between the real and modelled data is plotted below them in black.

For the system identification each of the pressure sensor signals were subtracted from the signal of Sensor 5 in the nose, thus removing the hydrostatic component from the data. The sensor positions were converted into polar coordinates resulting in each sensor being represented by $i (r_i, \sin(\theta_i))$, where $i = (1, \dots, 9)$. The position of each sensor along with the crafts motion data (position, velocity and acceleration) were fed into the NARMAX method to produce a model for pressure terms $p_5 - p_i$. For detailed description of how the NARMAX method was used refer to [88]. In the system identification process the radius r_i was removed from the system as a nonessential parameter and as there was also a symmetry between the sides of the platform's head, $|\theta_i|$ was used instead of θ_i .

To train and validate the model, the data from different flow speeds were divided into two parts. The training data was used to estimate the parameters of the model which were then evaluated using the validation data. The coefficient of determination (R^2) and the mean absolute error (MAE) between real and predicted pressures – were computed to measure the performance. The resultant model is a second-order polynomial

$$p_5 - p_i = (20.4 \sin(|\theta_i|) + 4.7) \frac{dU}{dt} + 68.9U^2 + (21.1 \sin(|\theta_i|) - 18.0)U + 2.7 \sin(|\theta_i|) - 1.6. \quad (4.10)$$

Figure 4.4(a) shows the experimental pressure data and the pressure data predicted by the forward model. Close match between the two is indicated by $R^2 = 0.84$ and $MAE = 7.71 \pm 0.03 Pa$. The difference between experimental and predicted data is shown with black and it indicates that the model performed well but is less accurate when turbulent noise or high acceleration create peaks in pressure readings.

We analyzed the sensitivity of the forward model to get a better understanding of the relationship between the motion parameters and the pressure signals. We defined the sensitivity as a derivative of the pressure differences with respect to the velocity U and to the acceleration $\frac{dU}{dt}$.

$$\frac{\partial(p_5 - p_i)}{\partial U} = 137.8U + 21.1 \sin(|\theta_i|) - 18.0. \quad (4.11)$$

$$\frac{\partial(p_5 - p_i)}{\partial \frac{dU}{dt}} = 20.4 \sin(|\theta_i|) + 4.7. \quad (4.12)$$

In Equation (4.11) and Equation (4.12), $\sin(|\theta_i|)$ can be determined by choosing a sensor. It is apparent that the sensitivity coefficient of the velocity in Equation (4.11) increases proportionally with the increasing velocity, whereas the coefficient of acceleration in Equation (4.12) remains constant. It shows again that at low flow speeds the acceleration of the craft is dominating the pressure changes around the craft, but when the flow speed is increased the effect of acceleration diminishes compared to that of the flow speed. With the constant flow speed, however, the pressure level also remains constant so it

would not affect detection of external stimuli if it were not for turbulence that increases proportionally with flow speed. Unfortunately, turbulence causes unpredictable changes in pressure sensor signal and our model can't help with them.

$$U = 0.01(p_5 - p_1) - 0.09(p_5 - p_3) + 0.04(p_5 - p_6) + 0.03(p_5 - p_8) + 0.03(p_5 - p_9) - 0.06. \quad (4.13)$$

We used the NARMAX method also to obtain a reverse model, linking the pressure readings to the velocity of the craft. The resultant model is given in Equation (4.13). Figure 4.4(b) illustrates the measured and predicted velocities as well as their difference with $R^2 = 0.92$ and $MAE = 2.16 \pm 0.027 \text{ cm s}^{-1}$. The model performed well for higher flow speed but lacked the accuracy when the resultant velocity was below 5.4 cm s^{-1} . In chapter 4.1 we saw that the pressure changes from the experiment in still water were mostly related to the acceleration of the craft. However, for simplicity the reverse model was designed to describe a linear relationship between the pressure sensor signals and the flow velocity. The model can also accommodate the relationship with the acceleration but it requires time lagged pressure terms, making the model much more complex.

Conclusion

We have created the forward model that can predict self-movement signals for pressure sensors and the reverse model, predicting relative swimming speed based on pressure measurements. With the forward model a craft equipped with an accelerometer can use the model to generate a signal from acceleration measurements and subtract it from signals of lateral line sensors, enhancing the lateral line sensitivity to external stimulation sources. The reverse model can be used the other way around, it can predict craft's relative speed with respect to flow.

Both the forward and reverse model was derived using the pressure sensor position in the head of the craft as one of the parameters. This measure helped to make the model more accurate but also made it unusable on crafts with a different shape or sensor positioning. For other fusiform crafts, a similar model can be built based on their pressure sensor and movement data.

While creating these models we found that with low flow speeds the self-movement signal in pressure sensors was mostly created by the acceleration of the craft but as the flow speed increased the sensitivity to it also increased. Whereas flow speed itself is not disturbing detection of external stimuli, it creates turbulence that increases noise and therefore makes signal detection harder. These results suggest that moving at low and constant velocity is preferable as a sensing strategy to focus on external stimuli when it is not possible to suppress the self-motion signal.

This observation has also a biological relevance, helping to explain why fish tend to swim quietly using burst and coast swimming when watching out for

predators. It can be interpreted as an effort to minimize self-motion effects and increase the sensitivity of the lateral line to external stimuli. Some sources however suggest that fish are capable of reducing the influence of self-movement to lateral line signals while processing flow field information [52–54]. So quiet swimming is either used to reduce turbulence created with higher speeds or by fish who try to reduce their signature in the flow field to stay less detectable by other fish.

5 Improving efficiency of tail fin propulsion

In previous chapters we described data processing tools for flow data and how to predict self-motion signals in artificial lateral line sensors, but the information was not used for anything other than analysis. As flow sensors and methods of flow sensing are still in the early stage of development, using them for vehicle control is very rare. Few examples [86] show that this noisy and complex flow information can be useful for choosing between swimming strategies and implementing them.

One very complex swimming mode known from biology is Kármán gaiting. Fish Kármán gait to reduce their energy consumption in vortex streets. The gait is known by its increased lateral movement and reduced tail beat frequency that match the frequency of a vortex street. For further details about Kármán gaiting refer back to Chapter 1.1. Most of the studies about Kármán gaiting suggest that thrust generation in Kármán gaiting is mostly passive and that fish's control over the process is minimal, using lateral line sensing only for stabilization [23].

The research presented in this chapter is based on results published in [89]. In this chapter we look what kind of flow information is necessary and sufficient to synchronize the tail beat of a robotic fish (Chapter 2.5) with vortices. Though the lateral movement is characteristic to a Kármán gaiting fish, we here investigate only one component of this motion pattern – the tail beat synchronization with vortices. The lateral movement and the change of yaw angle were restrained by harnessing the robotic fish on a force plate to measure the performance of the tail propulsion. The performance of the vortex synchronized propulsion is compared with the propulsion in steady flow showing the thrust and efficiency of the fishlike robot.

5.1 Swimming in Kármán vortex street

As described in Chapter 1.1, fish use their body as a hydrofoil to generate thrust in laterally alternating flows. Forces generated on the fish's body make it slalom between the vortices, resulting in the 180° interaction phase for center of the mass of the fish. The 180° phase angle means that a laterally oscillating fish's body is in maximum displacement away from the vortex that is in the same streamwise position.

In our experiments of vortex synchronized propulsion we used a fishlike robot (Platform 3) described in Chapter 2.5. The robot is harnessed to the floor of the flow tunnel and can move its tail. When compared to Kármán gaiting fish, the robot can't move laterally or change its angle and thus the passive thrust production used by fish is not working on this robot's body. However, if we look only at the tail fin we see that the fin can be considered as a hydrofoil that is moved laterally and is changing also its yaw angle. The thrust production by the fin can be seen as analogous to thrust production in experiments of Gopalkrishnan et al. [26] and in the model of Streitlien et al. [28] that predicted

highest thrust and efficiency when the hydrofoil is actuated with the interaction phase between 0° to 90° with respect to vortices. In Figure 5.1 we have an illustration of Platform 3 propulsion with 0° phase in the picture above and 180° phase in the picture below.

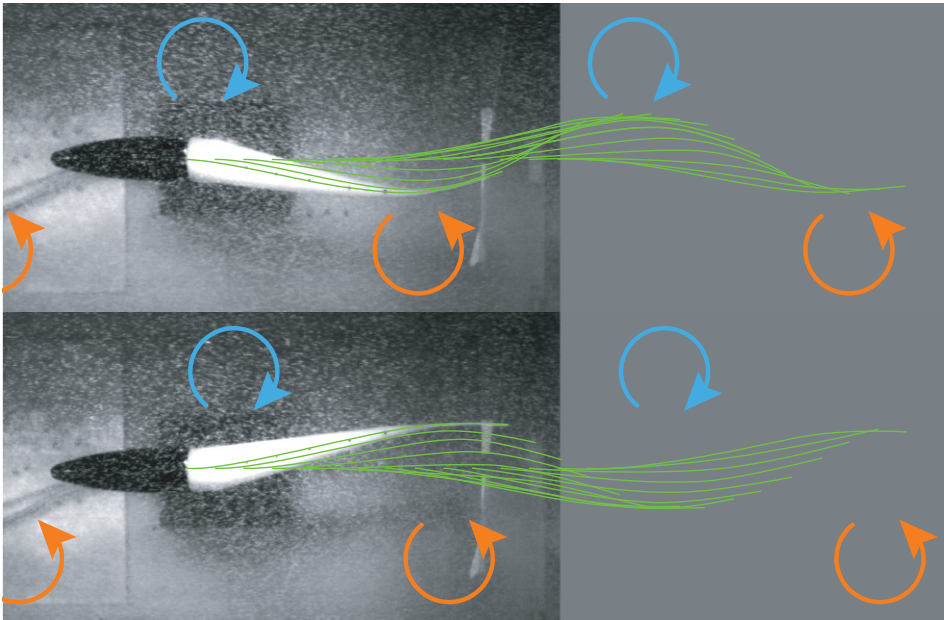


Figure 5.1. Platform 3 propulsive movements in a Kármán vortex street. Here the vortex street is taken as a frame of reference and clockwise vortices are represented as blue circular arrows while counter-clockwise vortices are represented with orange circular arrows. Green lines represent the center line of the robot's tail as it is moving with respect to vortices. The picture on top illustrates the interaction phase 0° , where the tail sweeps closer to vortices in their streamwise positions. The picture below illustrates an opposite phase angle, where the tail is moved furthest away from vortices.

5.2 Vortex synchronization

In the experiment of [26] the hydrofoil's synchronization with vortices was achieved through vortex shedding manipulation with an oscillating cylinder. However, the manipulation of an environment is not an option when the purpose of vortex synchronization is to make underwater robots swim more efficiently by using alternating flow regimes. A swimming robot does not have control over the oncoming flow but it can be equipped with sensors that provide the information necessary for synchronization.

In Chapter 3.1 we showed that the pressure sensors could sense vortices of a Kármán street as oscillations in their signal. We have also demonstrated that the vortex shedding frequency can be derived from pressure fluctuations. But as discussed in [27], the frequency matching is not enough to make the swimming in a Kármán vortex street efficient. Instead, the crucial part is the timing of the interaction with vortices.

In our study we confirmed the importance of the tail beat timing with a simple experiment where the tail of the robotic fish was actuated with a frequency slightly different from the vortex shedding frequency. This way the interaction timing was changing continuously and the effect could be seen as low frequency oscillations in thrust production. It is similar to the aliasing effect known to occur in a sampling process of a signal. The frequency analysis from the force signal shows that there is a strong frequency component matching the difference between the vortex shedding frequency and the tail beat frequency (Figure 5.2(a)). The measurement suggest that when the frequencies are different the trust production oscillates and is highest whenever the tail is in a proper phase with respect to vortices and lowest when opposite. Having proved that the timing of interactions between the tail beat and vortices influences the thrust production of our robotic fish, we set ourselves to find the timing that is most efficient.

In order to do that, the robot needs to know where the vortices are. In a regular Kármán street behind a cylinder, vortices create a high pressure zone on an object in a Kármán vortex street. It precedes each vortex as it moves past an object in the flow. These fluctuations of pressure can be identified in pressure sensor signals and enhanced by subtracting signals of sensors that are at the same position along the robot's length but on the opposite sides. In the enhanced signal the maximums and minimums can be used to predict the arrival of the vortex to the streamwise position next to the tailfin. An algorithm finding the extremes in the signal can be made reliable by filtering the signal with an appropriate low pass filter, chosen to suppress noise above the vortex shedding frequency (Figure 5.2(b)).

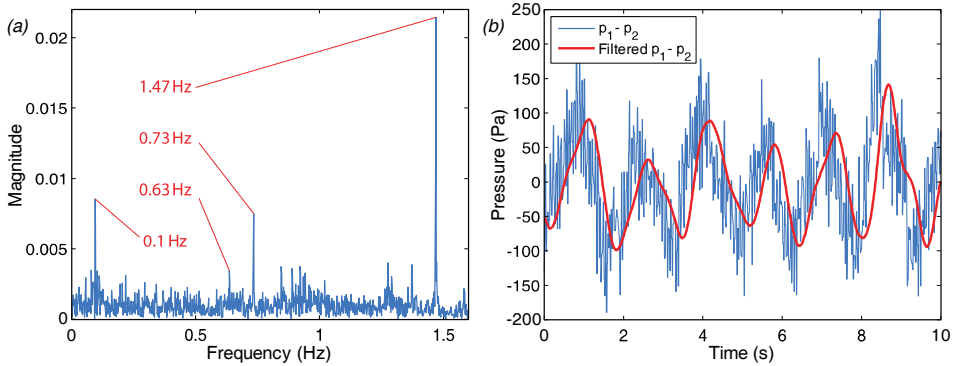


Figure 5.2. (a) Thrust of the tail beat shown in the frequency domain indicating the aliasing frequency at 0.1 Hz that is produced by the actuation of the tail with frequency 0.73 Hz in a vortex street with the vortex shedding frequency 0.63 Hz. The dominant frequency in thrust is twice the frequency of the tail beat as the thrust is produced by each tail sweep. Energy in the frequency components that represents the tail beat frequency and the vortex shedding frequency is much smaller. (b) Enhanced pressure signal produced by subtracting signals of sensors on opposite sides of Platform 3. The actual signal in blue is superimposed with its low pass filtered signal in red.

Knowing the time when a vortex created a pressure maximum on a pressure sensor enables finding the time delay at which the tail beat gives the best thrust. But to adjust with the change in the flow speed, the delay is divided into two parts. The first part is the time it takes for a vortex to travel from the nose to the tailfin and the second part is for adjusting the phase shift with respect to the vortex shedding period, allowing to make observations with different phase shifts that are comparable between different flow speeds.

The control of the tail beat is accomplished through sinusoidal half-period sweeps that move the tail from one maximum deflection angle to the opposite. Each sweep is determined by its start and end. A new sweep begins at the end of the last one, determining its starting time. The end of a new sweep is calculated from the time of the detection of a maximum in the pressure signal by adding appropriate delays. This method eliminates the need for frequency matching as it happens anyway when the sweeps match the pressure maximums. It also gives freedom to change the phase shift angle during an experiment, resulting in smooth transitions without fast movements of the tail that could affect the thrust measurements.

5.3 Performance of the vortex synchronized tail beat

In Figure 5.2(a) the aliasing frequency component indicated that our robot's thrust production depends on the interaction phase between the tail beat and the vortices. To determine the best interaction phase we conducted an experiment, measuring thrust for different interaction phases. The phase was changed with 30° increments, where in each increment we recorded 2 minutes of reference data without tail movement and 3 minutes of data with movement. In the experiment the change of phase covered the whole 0° to 360° sweep.

Drag and thrust are not separable at swimming so we chose a reference force for thrust measurements. The reference force was measured in a Kármán vortex street while the tail of the robot was straight and stationary. The thrust force was calculated by subtracting the reference force from the force that was measured while the tail was actuated. To make the results comparable with other studies we calculated the thrust coefficient C_{th} that compensates thrust force F_{th} with fluid density ρ , flow speed U and the robot's projection area A on the plane perpendicular to the flow direction (Equation (5.1)).

$$C_{th} = \frac{2F_{th}}{\rho U^2 A} \quad (5.1)$$

The change of thrust coefficient with respect to the phase between the tail beat and vortices is plotted in Figure 5.3(a). Each data point on that graph represents the average value of thrust calculated over 120 seconds of data. Only 2 minutes of data from each 3 minute phase step was used to avoid using data from the transitions between the steps. In the graph the thrust coefficient changed from -0.03 to 0.34 with the maximum at 0° for the tail's tip of the robot and the minimum at 180° phase shift angle. These measurements are not

directly relatable to other studies such as [27], [28], [30] because the phase of the tail of our robot is shown with respect to the high pressure zone that can be detected with pressure sensors, while the studies mentioned above measure the phase with respect to the vortex core. Converting the results would shift the curve in the graph, making the peak of the maximum thrust appear between 45° and 90° .

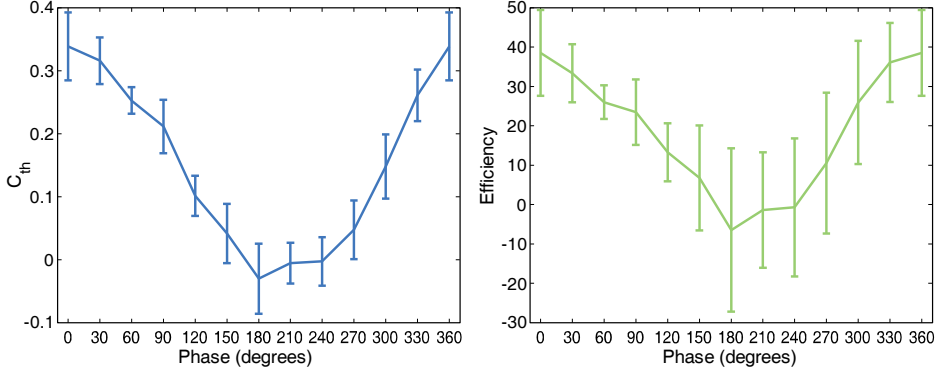


Figure 5.3. (a) Thrust coefficient C_{th} with respect to the interaction phase. Error bars show the standard deviation of C_{th} . (b) Propulsion efficiency η with respect to the interaction phase. Error bars show the standard deviation of η .

The results in Figure 5.3(b) need the same treatment to be comparable to other studies of propulsion in alternating flows. Figure 5.3(b) shows the efficiency of the tail beat propulsion. The efficiency is calculated by dividing the useful power P_{th} that creates thrust with total power P_{tot} . Using angular feedback from the motor, the total power is calculated as a product of torque τ and angular speed ω of the tail. The corresponding equation of efficiency is the following:

$$\eta = \frac{P_{th}}{P_{tot}} = \frac{F_{th} * U}{\tau * \omega}. \quad (5.2)$$

The peak and the trough of the efficiency appear at the same phase angles as for the thrust coefficient. Changing the phase resulted in the 45 percent point difference between the maximum efficiency at 38.5% and the minimum efficiency at -6.5%. The difference of 45 percent points in efficiency is considerable even if the maximum efficiency is quite low compared to Kármán gaiting fish.

In these experiments we noticed that the increase of propulsion efficiency comes from reducing the lateral forces acting on the tail. To show this, we conducted experiments at five flow speeds in a Kármán vortex street and for each flow speed we measured the thrust and the lateral force at two opposite interaction phase angles between the tail beat and vortices: one for minimum thrust and the other for maximum thrust.

Figure 5.4(a) shows how the average thrust force changed with respect to the flow speed for both phase shift angles. It can be seen that the thrust force

generated with the best interaction phase increase linearly with the flow speed. The increase can be explained with vortices that grow stronger at higher speeds. In the same figure, however, the worst interaction phase produces constantly low thrust irrespective of the flow speed. Exactly the opposite can be seen in Figure 5.4(b) that shows the average lateral forces acting on Platform 3. The experiments with the interaction phase, that produced low thrust on the previous graph, have also a higher lateral force production and it increases linearly with flow speed. On the other hand the experiments with high thrust production show only minimal lateral forces.

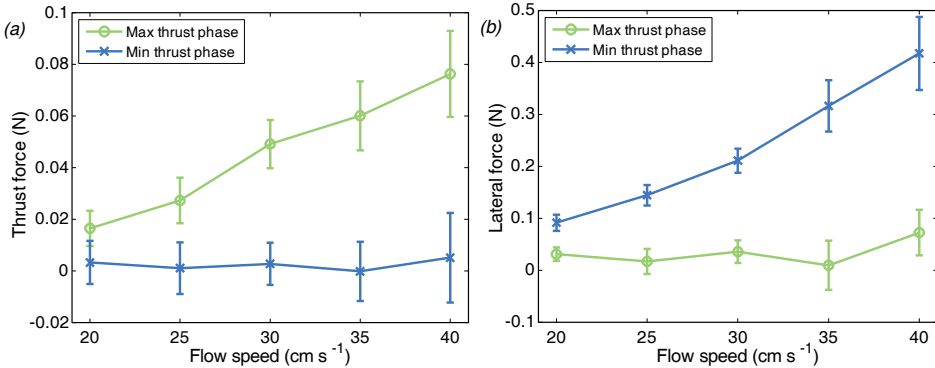


Figure 5.4. (a) Thrust force with respect to the flow speed for the interaction phases that produce minimum and maximum thrust. (b) An absolute value of the lateral force with respect to the flow speed for the same interaction phases. Each data point represents an average value calculated from 5 minutes of data and the error bars show the standard deviation over these datasets.

It means that with only little change in the total power consumption most of the efficiency increase comes from using the energy that is otherwise wasted for the production of lateral forces. When the tail is actuated the largest lateral forces act on the tail when the tail is in the edge position and the motor is reversing its movement. The reduction of lateral forces can be explained with the tail beat timing. Pressure forces created by vortices can reduce the motor's effort by slowing down the tail when it reaches to the edge position, allowing to increase the speed of the tail faster for the next sweep. The forces reducing the momentum of the tail also act on the tail fin, bending it to a steeper angle and increasing the trust force generated on it. The difference in tail fin angles is visible in Figure 5.1 where the green midlines in the picture on top are more bent than in the picture below.

Using the results from the experiments with 5 different flow speeds we calculated thrust coefficients and efficiencies and compare them with the corresponding results in steady flows. In the steady flow experiments the tail was actuated with the same frequency as in the Kármán vortex street with the corresponding flow speed. In Figure 5.5(a) it is shown how the thrust coefficient changes with the flow speed. The red line in the graph represent the magnitude of the drag coefficient of Platform 3 in steady flows. The figure

shows that the tail beat frequency, dictated by the vortex shedding frequency of the Kármán vortex street, would not be enough for a free swimming robot to hold station in steady flows. However, the vortex synchronization maximizing the thrust manage to cross that threshold. As the magnitude of the drag coefficient is measured in steady flows, the robot would need even less power to hold station in a Kármán vortex street, making the vortex synchronization an even more attractive choice over swimming in steady flow.

Under the same Kármán street conditions the minimum thrust synchronization shows very poor performance, well below the thrust coefficients from steady flows. Considering that the arbitrary tail beat frequency would result in average thrust between the best thrust (green line) and the worst thrust (blue line) shown in this graph, the resulting thrust production would give about the same amount of the thrust as the same tail beat frequency in steady flows.

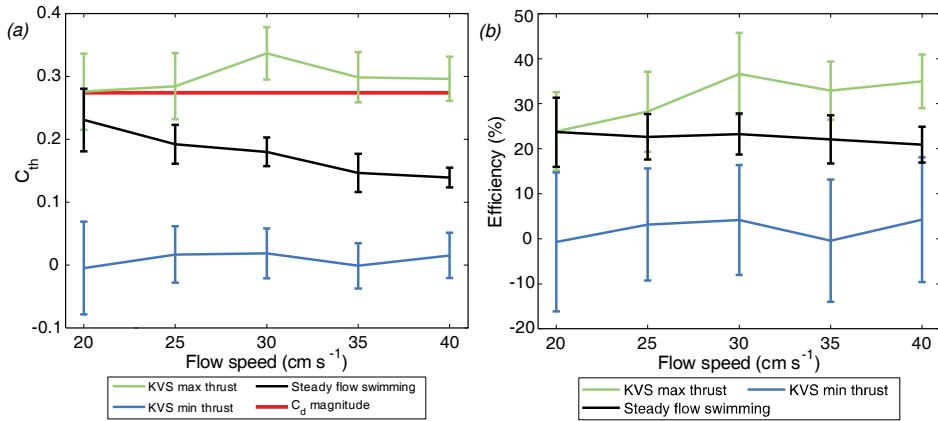


Figure 5.5. (a) Thrust coefficient with respect to the flow speed. The red line represents the magnitude of the drag coefficient in steady flows. (b) Efficiency of the tail beat propulsion with respect to the flow speed. The interaction phases for minimum and maximum thrust experiments correspond respectively to 180° and 0° as found from the results presented in Figure 5.3(a).

Efficiency for the tail beat propulsion is shown in Figure 5.5(b). Here we see that at a low speed the vortices are weak and the vortex synchronization does not improve the propulsion efficiency when compared to the results in steady flow. Again, the reduced drag in the Kármán vortex street is not shown here and that aspect may have a considerable effect when choosing between these flow regimes. At higher speeds, however, the decision is obvious as the maximum thrust synchronization surpasses the efficiency in steady flows with about 10 percent points.

Conclusion

In this chapter we described our results from experiments where we harnessed a robotic fish, longer than wavelength of Kármán vortex street, into a flow tunnel

and measured thrust production of the robot with different interaction phases between the tail fin and vortices. We synchronized the tail beat with vortices by using flow information gathered with pressure sensors mounted inside the head of a robotic fish. Even though it is believed that fish don't need lateral line for Kármán gaiting [23], [25], it helps robots, incapable of Kármán gaiting, to synchronize with vortices in a Kármán vortex street.

The performance measurements of our robotic fish show that a correct timing between the tail beat and vortices increase thrust considerably compared to the steady flow swimming. When comparing the performances of the best and the worst interaction phase propulsion in a Kármán vortex street, a difference of 45 percent points in efficiency was measured between the two. Further experiments showed that with a correct timing the robot reduces its lateral forces so that more power is spent for thrust production, while in the opposite phase of the tail beat, most of power is wasted for production of lateral forces. It shows that without flow information a fin based robot uses only half of its potential in a Kármán vortex street.

We have noticed that fish that choose to Kármán gait have usually the body length below the wavelength of a Kármán vortex street [18]. One reason for why a specimen, too large compared to the wavelength of a Kármán vortex street, choose not to Kármán gait may be the reduced efficiency of the passive thrust production. In our experiments the robotic fish was harnessed to the flow tunnel but regardless of that the results should apply also for free swimming robots that are oversized for the vortex street they are swimming in. In that case the mass of the robot acts as a harness and the tail of the robot can use the vortices to increase its thrust production. In that light an underwater robot needs to choose how it behaves in alternating flows. If it is small compared to the flow features it may want to implement swimming strategy similar to Kármán gaiting and let the flow produce the thrust passively. However, a larger craft that can ignore the lateral forces may want to implement the tail beat control that has been shown here.

Conclusions and future work

While artificial flow sensors for lateral line systems are still in development and need some maturing for improved accuracy and durability, we have decided to start developing tools for analysis and interpretation of flow data. Flow sensing in this thesis have been performed with 3 different lateral line platforms. The artificial lateral lines were built using commercially available miniature pressure sensors. One of these platforms is capable of sampling pressure field in three dimensions around the head of a fishlike body while the other one is capable of using information from its artificial lateral line to adjust its fin propulsion.

Along with descriptions of sensing platforms this thesis also provides experimental results from pressure field analysis. We show that by using pressure sensitive artificial lateral line it is possible to distinguish Kármán vortex streets from steady flows, determine craft's orientation with respect to incoming flow and measure craft's lateral deviation from center axis of a Kármán vortex street. We demonstrate that the standard deviation of pressure sensor signals and the agreement on dominant frequency between the pressure sensors are valuable methods for detecting Kármán vortex streets. Both of them may seem time consuming and more suitable for offline analysis, however, we suggest that the response time for these methods can be reduced by sacrificing some of the accuracy. The data processing methods that help distinguish between flows and can determine underwater robot's orientation and position with respect to flow features are valuable tools in making underwater robots more efficient and successful in their missions. By using artificial lateral lines future marine vehicles will be able to modify their propulsion strategy based on the flow information.

While an underwater robot measures its surrounding flow field it can't stay motionless with respect to the flow. At the same time, the robot's motion makes the detection of external stimuli harder as it affects the flow field around the craft. To suppress these self-induced signals we suggest a method that can be used to train a model that can predict the influence of motion on the pressure signal. The model accounts for the shape of the craft and pressure sensor positions to predict self-induced signals for pressure sensor data. The method presented in this thesis is a part of the self-motion research, taking into account only forward-backward movement of the craft. In future work we plan to supplement the model to account for lateral and rotational movements. Using this kind of model with onboard accelerometers would be very useful for example for a free swimming robot in a Kármán vortex street as it would allow the craft to separate flow mediated oscillations from the oscillations created with the undulating body.

In the last chapter of this thesis we presented a study of vortex synchronization for fin propelled robots. We took Kármán gaiting fish that match their tail beat with the vortex shedding frequency as an example to save

energy in Kármán vortex streets. In this study we have considered only the tail beat component of Kármán gaiting, neglecting the lateral motion and yaw angle change that are also characteristic to fish swimming in a Kármán vortex street. With this study we showed that a pressure sensing lateral line can provide enough information for tail beat synchronization with vortices. The relation between thrust and vortex interaction phase has been shown before by Gopalkrishnan et al. [26], they did it with a rigid 2 dimensional hydrofoil and synchronized it by manipulating a vortex street with an oscillating cylinder. The synchronization method using information from an artificial lateral line has an advantage here, as it can be used on autonomous underwater vehicles. With flow characterization methods and adaptive self-motion filtering on artificial lateral line, new flow negotiation methods can be developed for underwater robots, making them able to manage energy rich turbulent flows.

For now we suggest the tail fin synchronization method for fishlike robots that swim in vortex streets with the wavelength below their body length. With a robotic fish harnessed in flow we have shown that for a big enough robot that can use its mass as an anchor, it is beneficial to choose a synchronized Kármán vortex street swimming over a steady flow swimming. The swimming method is not as efficient as Kármán gaiting as it creates the propulsion with an active tail beat, but it enables to save energy compared to the steady flow swimming. Development of robotic Kármán gaiting is still our future goal as passive propulsion is most efficient for fishlike crafts with the body length below the wavelength of a Kármán vortex street.

References

- [1] S. Peleshanko, M. D. Julian, M. Ornatska, M. E. McConney, M. C. LeMieux, N. Chen, C. Tucker, Y. Yang, C. Liu, J. A. C. Humphrey, and V. V. Tsukruk, "Hydrogel-Encapsulated Microfabricated Haircells Mimicking Fish Cupula Neuromast," *Advanced Materials*, vol. 19, no. 19, pp. 2903–9, Oct. 2007.
- [2] M. E. McConney, N. Chen, D. Lu, H. A. Hu, S. Coombs, C. Liu, and V. V. Tsukruk, "Biologically inspired design of hydrogel-capped hair sensors for enhanced underwater flow detection," *Soft Matter*, vol. 5, no. 2, pp. 292–5, 2009.
- [3] F. Jiang, Y. Tai, C. Ho, R. Karan, and M. Garstenauer, "Theoretical and experimental studies of micromachined hot-wire anemometers," in *Electron Devices Meeting*, 1994, pp. 139–42.
- [4] J. Chen, Z. Fan, J. Zou, J. Engel, and C. Liu, "Two-dimensional micromachined flow sensor array for fluid mechanics studies," *Journal of Aerospace Engineering*, vol. 16, no. 2, pp. 85–97, 2003.
- [5] V. I. Fernandez, S. M. Hou, F. S. Hover, J. H. Lang, and M. S. Triantafyllou, "Lateral-line-inspired MEMS-array Pressure Sensing for Passive Underwater navigation," in *15th Int. Symp. on Unmanned Untethered Submersible Technology (Durham, NH)*, 2007.
- [6] C. C. Lindsey, "Form, function and locomotory habits in fish," in *Fish Physiology Vol. VII Locomotion*, W. S. Hoar and D. J. Randall, Eds. New York: Academic, 1978, pp. 1–100.
- [7] M. Sfakiotakis, D. M. Lane, and J. B. C. Davies, "Review of fish swimming modes for aquatic locomotion," *IEEE Journal of Oceanic Engineering*, vol. 24, no. 2, pp. 237–52, Apr. 1999.
- [8] J. C. Montgomery, S. Coombs, and C. F. Baker, "The mechanosensory lateral line system of the hypogean form of *Astyanax fasciatus*," *Environmental Biology of Fishes*, vol. 62, pp. 87–96, 2001.
- [9] R. Bainbridge, "The speed of swimming of fish as related to size and to the frequency and amplitude of the tail beat," *Journal of Experimental Biology*, vol. 35, pp. 109–33, 1958.

- [10] B. C. Jayne and G. V. Lauder, "Speed effects on midline kinematics during steady undulatory swimming of largemouth bass, *Micropterus salmoides*," *The Journal of Experimental Biology*, vol. 198, pp. 585–602, Jan. 1995.
- [11] P. W. Webb, P. T. Kostecki, and E. D. Stevens, "The effect of size and swimming speed on locomotor kinematics of rainbow trout," *Journal of Experimental Biology*, vol. 109, pp. 77–95, 1984.
- [12] P. W. Webb, "Is the high cost of body/caudal fin undulatory swimming due to increased friction drag or inertial recoil?," *Journal of Experimental Biology*, vol. 162, pp. 157–66, 1992.
- [13] E. G. Drucker and G. V. Lauder, "Locomotor forces on a swimming fish: three-dimensional vortex wake dynamics quantified using digital particle image velocimetry," *The Journal of Experimental Biology*, vol. 202, no. Pt 18, pp. 2393–2412, Jan. 1999.
- [14] G. V. Lauder, "Function of the Caudal Fin During Locomotion in Fishes: Kinematics, Flow Visualization, and Evolutionary Patterns," *American Zoologist*, vol. 40, pp. 101–22, 2000.
- [15] C. Eloy, "Optimal Strouhal number for swimming animals," *Journal of Fluids and Structures*, vol. 30, pp. 205–18, Apr. 2012.
- [16] U. K. Müller, B. L. E. van den Heuvel, E. J. Stamhuis, and J. J. Videler, "Fish foot prints: morphology and energetics of the wake behind a continuously swimming mullet (*Chelon labrosus* Risso)," *The Journal of Experimental Biology*, vol. 200, pp. 2893–906, Jan. 1997.
- [17] P. W. Webb, "Body form, locomotion and foraging in aquatic vertebrates," *American Zoologist*, vol. 24, no. 1, pp. 107–20, 1984.
- [18] J. C. Liao, D. N. Beal, G. V. Lauder, and M. S. Triantafyllou, "Fish exploiting vortices decrease muscle activity," *Science (New York, N.Y.)*, vol. 302, no. 5650, pp. 1566–9, Nov. 2003.
- [19] P. W. Webb, "Entrainment by river chub *Nocomis micropogon* and smallmouth bass *Micropterus dolomieu* on cylinders," *Journal of Experimental Biology*, vol. 201, pp. 2403–12, 1998.
- [20] C. L. Cook and D. J. Coughlin, "Rainbow trout *Oncorhynchus mykiss* consume less energy when swimming near obstructions," *Journal of Fish Biology*, vol. 77, no. 7, pp. 1716–23, Nov. 2010.

- [21] A. Przybilla, S. Kunze, A. Rudert, H. Bleckmann, and C. Brücker, “Entraining in trout: a behavioural and hydrodynamic analysis,” *Journal of experimental biology*, vol. 213, pp. 2976–86, Sep. 2010.
- [22] J. C. Liao, D. N. Beal, G. V. Lauder, and M. S. Triantafyllou, “The Kármán gait: novel body kinematics of rainbow trout swimming in a vortex street,” *The Journal of Experimental Biology*, vol. 206, pp. 1059–73, Mar. 2003.
- [23] J. C. Liao, “The role of the lateral line and vision on body kinematics and hydrodynamic preference of rainbow trout in turbulent flow,” *The Journal of Experimental Biology*, vol. 209, pp. 4077–90, Oct. 2006.
- [24] K. D. Fausch, “Profitable stream positions for salmonids: relating specific growth rate to net energy gain,” *Canadian Journal of Zoology*, vol. 62, no. 3, pp. 441–51, 1984.
- [25] D. N. Beal, F. S. Hover, M. S. Triantafyllou, J. C. Liao, and G. V. Lauder, “Passive propulsion in vortex wakes,” *Journal of Fluid Mechanics*, vol. 549, pp. 385–402, Feb. 2006.
- [26] R. Gopalkrishnan, M. S. Triantafyllou, G. S. Triantafyllou, and D. Barrett, “Active vorticity control in a shear flow using a flapping foil,” *Journal of Fluid Mechanics*, vol. 274, pp. 1–21, 1994.
- [27] M. S. Triantafyllou, A. H. Techet, Q. Zhu, D. N. Beal, F. S. Hover, and D. K. P. Yue, “Vorticity Control in Fish-like Propulsion and Maneuvering,” *Integrative and Comparative Biology*, vol. 42, no. 5, pp. 1026–31, Nov. 2002.
- [28] K. Streitlien, G. S. Triantafyllou, and M. S. Triantafyllou, “Efficient foil propulsion through vortex control,” *AIAA Journal*, vol. 34, no. 11, pp. 2315–19, 1996.
- [29] S. Alben, “On the swimming of a flexible body in a vortex street,” *Journal of Fluid Mechanics*, vol. 635, pp. 27–45, Sep. 2009.
- [30] S. Alben, “Passive and active bodies in vortex-street wakes,” *Journal of Fluid Mechanics*, vol. 642, pp. 95–125, Dec. 2010.
- [31] T. Teyke, “Morphological Differences in Neuromasts of the Blind Cave Fish *Astyanax hubbsi* and the Sighted River Fish *Astyanax mexicanus*,” *Brain, Behavior and Evolution*, vol. 35, no. 1, pp. 23–30, 1990.

- [32] S. M. van Netten, “Hydrodynamic detection by cupulae in a lateral line canal: functional relations between physics and physiology,” *Biological Cybernetics*, vol. 94, no. 1, pp. 67–85, Jan. 2006.
- [33] M. J. McHenry and S. M. van Netten, “The flexural stiffness of superficial neuromasts in the zebrafish (*Danio rerio*) lateral line,” *The Journal of Experimental Biology*, vol. 210, pp. 4244–53, Dec. 2007.
- [34] A. Schmitz, H. Bleckmann, and J. Mogdans, “Organization of the superficial neuromast system in goldfish, *Carassius auratus*,” *Journal of Morphology*, vol. 269, no. 6, pp. 751–61, Jun. 2008.
- [35] Y. Yang, N. Nguyen, N. Chen, M. Lockwood, C. Tucker, H. Hu, H. Bleckmann, C. Liu, and D. L. Jones, “Artificial lateral line with biomimetic neuromasts to emulate fish sensing,” *Bioinspiration & Biomimetics*, vol. 5, no. 1, pp. 016001:1–9, Mar. 2010.
- [36] J. C. Montgomery, C. F. Baker, and A. G. Carton, “The lateral line can mediate rheotaxis in fish,” *Nature*, vol. 389, pp. 960–3, 1997.
- [37] C. F. Baker and J. C. Montgomery, “The sensory basis of rheotaxis in the blind Mexican cave fish, *Astyanax fasciatus*,” *Journal of Comparative Physiology A*, vol. 184, no. 5, pp. 519–27, 1999.
- [38] J. Engelmann, W. Hanke, J. Mogdans, and H. Bleckmann, “Neurobiology: Hydrodynamic stimuli and the fish lateral line,” *Nature*, vol. 408, pp. 51–2, Sep. 2000.
- [39] J. Engelmann, W. Hanke, and H. Bleckmann, “Lateral line reception in still- and running water,” *Journal of Comparative Physiology A*, vol. 188, no. 7, pp. 513–26, Aug. 2002.
- [40] J. C. Montgomery, F. Macdonald, C. F. Baker, and A. G. Carton, “Hydrodynamic Contributions to Multimodal Guidance of Prey Capture Behavior in Fish,” *Brain, Behavior and Evolution*, vol. 59, no. 4, pp. 190–8, 2002.
- [41] B. L. Partridge and T. J. Pitcher, “The sensory basis of fish schools: relative roles of lateral line and vision,” *Journal of Comparative Physiology A*, vol. 135, pp. 315–25, 1980.
- [42] A. M. Sutterlin and S. Waddy, “Possible Role of the Posterior Lateral Line in Obstacle Entrainment by Brook Trout (*Salvelinus fontinalis*),”

Journal of the Fisheries Research Board of Canada, vol. 32, no. 12, pp. 2441–6, 1975.

- [43] J. C. Montgomery, F. McDonald, C. F. Baker, A. G. Carton, and N. Ling, “Sensory integration in the hydrodynamic world of rainbow trout,” *Proc. R. Soc. Lond. B*, vol. 270, pp. 195–7, Nov. 2003.
- [44] T. Teyke, “Flow field, swimming velocity and boundary layer: parameters which affect the stimulus for the lateral line organ in blind fish,” *Journal of Comparative Physiology A*, vol. 163, no. 1, pp. 53–61, 1988.
- [45] E. S. Hassan, “Hydrodynamic imaging of the surroundings by the lateral line of the blind cave fish *Anoptichthys jordani*,” in S. Coombs, P. Gorner & H. Münz (ed.) *The Mechanosensory Lateral Line Neurobiology and Evolution*, 1989, pp. 217–28.
- [46] E. S. Hassan, H. Abdel-Latif, and R. Biebricher, “Studies on the effects of Ca^{2+} and Co^{++} on the swimming behavior of the blind Mexican cave fish,” *Journal of Comparative Physiology A*, vol. 171, no. 3, pp. 413–19, 1992.
- [47] S. P. Windsor, S. E. Norris, S. M. Cameron, G. D. Mallinson, and J. C. Montgomery, “The flow fields involved in hydrodynamic imaging by blind Mexican cave fish (*Astyanax fasciatus*). Part I: open water and heading towards a wall,” *Journal of Experimental Biology*, vol. 213, pp. 3819–31, Nov. 2010.
- [48] S. P. Windsor, S. E. Norris, S. M. Cameron, G. D. Mallinson, and J. C. Montgomery, “The flow fields involved in hydrodynamic imaging by blind Mexican cave fish (*Astyanax fasciatus*). Part II: gliding parallel to a wall,” *Journal of Experimental Biology*, vol. 213, pp. 3832–42, Nov. 2010.
- [49] S. Dijkgraaf, “The functioning and significance of the lateral-line organs,” *Biological Reviews*, vol. 38, no. 1, pp. 51–105, 1963.
- [50] H. A. Visher, “The morphology of the lateral line system in 3 species of Pacific cottoid fishes occupying disparate habitats,” *Experientia*, vol. 46, no. 3, pp. 244–50, 1990.
- [51] H. Bleckmann and H. Münz, “Physiology of Lateral-Line Mechanoreceptors in a Teleost with Highly Branched, Multiple Lateral Lines,” *Brain, Behavior and Evolution*, vol. 35, no. 4, pp. 240–50, 1990.

- [52] T. C. Tricas and S. M. Highstein, "Action of the octavolateralis efferent system upon the lateral line of free-swimming toadfish, *Opsanus tau*," *Journal of Comparative Physiology A*, vol. 169, no. 1, pp. 25–37, 1991.
- [53] K. E. Feitl, V. Ngo, and M. J. McHenry, "Are fish less responsive to a flow stimulus when swimming?," *The Journal of Experimental Biology*, vol. 213, pp. 3131–7, Sep. 2010.
- [54] J. C. Montgomery and D. Bodznick, "An adaptive filter that cancels self-induced noise in the electrosensory and lateral line mechanosensory systems of fish," *Neuroscience Letters*, vol. 174, no. 2, pp. 145–8, 1994.
- [55] Z. Fan, J. Chen, J. Zou, D. Bullen, C. Liu, and F. Delcomyn, "Design and fabrication of artificial lateral line flow sensors," *Journal of Micromechanics and Microengineering*, vol. 12, no. 5, pp. 655–61, Sep. 2002.
- [56] N. Chen, C. Tucker, J. M. Engel, Y. Yang, S. Pandya, and C. Liu, "Design and Characterization of Artificial Haircell Sensor for Flow Sensing With Ultrahigh Velocity and Angular Sensitivity," *Journal of Microelectromechanical Systems*, vol. 16, no. 5, pp. 999–1014, Oct. 2007.
- [57] A. Qualtieri, F. Rizzi, M. T. Todaro, A. Passaseo, R. Cingolani, and M. De Vittorio, "Stress-driven AlN cantilever-based flow sensor for fish lateral line system," *Microelectronic Engineering*, vol. 88, no. 8, pp. 2376–8, Aug. 2011.
- [58] J. J. van Baar, M. Dijkstra, R. J. Wiegerink, T. S. J. Lammerink, and G. J. M. Krijnen, "Fabrication of arrays of artificial hairs for complex flow pattern recognition," in *2010 IEEE Sensors*, 2003, pp. 332–6.
- [59] M. Dijkstra, J. J. van Baar, R. J. Wiegerink, T. S. J. Lammerink, J. H. de Boer, and G. J. M. Krijnen, "Artificial sensory hairs based on the flow sensitive receptor hairs of crickets," *Journal of Micromechanics and Microengineering*, vol. 15, no. 7, pp. 132–8, Jul. 2005.
- [60] A. M. K. Dagamseh, C. M. Bruinink, H. Droogendijk, R. J. Wiegerink, T. S. J. Lammerink, and G. J. M. Krijnen, "Engineering of biomimetic hair-flow sensor arrays dedicated to high-resolution flow field measurements," in *2010 IEEE Sensors*, 2010, pp. 2251–4.
- [61] N. Izadi, M. J. de Boer, J. W. Berenschot, and G. J. M. Krijnen, "Fabrication of superficial neuromast inspired capacitive flow sensors,"

Journal of Micromechanics and Microengineering, vol. 20, no. 8, pp. 085041:1–9, Aug. 2010.

- [62] C. M. Bruinink, R. K. Jaganatharaja, M. J. de Boer, E. Berenschot, M. L. Kolster, T. S. J. Lammerink, R. J. Wiegerink, and G. J. M. Krijnen, “Advancements in technology and design of biomimetic flow-sensor arrays,” *IEEE International Conference on Micro Electro Mechanical Systems*, no. 1, pp. 152–5, Jan. 2009.
- [63] Y. Yang, J. Chen, J. Engel, S. Pandya, N. Chen, C. Tucker, S. Coombs, D. L. Jones, and C. Liu, “Distant touch hydrodynamic imaging with an artificial lateral line,” *Proceedings of the National Academy of Sciences of the United States of America*, vol. 103, no. 50, pp. 18891–5, Dec. 2006.
- [64] A. G. P. Kottapalli, M. Asadnia, J. M. Miao, G. Barbastathis, and M. S. Triantafyllou, “A flexible liquid crystal polymer MEMS pressure sensor array for fish-like underwater sensing,” *Smart Materials and Structures*, vol. 21, no. 11, pp. 115030:1–13, Nov. 2012.
- [65] J. Chen, J. Engel, N. Chen, S. Pandya, S. Coombs, and C. Liu, “Artificial Lateral Line And Hydrodynamic Object Tracking,” *19th IEEE International Conference on Micro Electro Mechanical Systems*, pp. 694–7, 2006.
- [66] V. I. Fernandez, S. M. Hou, F. S. Hover, J. H. Lang, and M. S. Triantafyllou, “Development and application of distributed MEMS pressure sensor array for AUV object avoidance,” in *16th Int. Symp. on Unmanned Untethered Submersible Technology (Durham, NH)*, 2009.
- [67] Measurement Specialties, “MS54XX miniature SMD pressure sensor,” 2012. [Online]. Available: <http://www.meas-spec.com/downloads/MS54XX.pdf>.
- [68] R. A. Conley and S. Coombs, “Dipole source localization by mottled sculpin. III. Orientation after site-specific, unilateral denervation of the lateral line system,” *Journal of Comparative Physiology A*, vol. 183, no. 3, pp. 335–44, Sep. 1998.
- [69] T. Salumäe, I. Ranó, O. Akanyeti, and M. Kruusmaa, “Against the flow: a Braitenberg controller for a fish robot,” in *IEEE International Conference on Robotics and Automation*, 2012, pp. 4210 – 15.

- [70] T. Teyke, “Collision with and avoidance of obstacles by blind cave fish *Anoptichthys jordani* (Characidae),” *Journal of Comparative Physiology A*, vol. 157, no. 6, pp. 837–43, 1985.
- [71] H. Abdel-Latif, E. S. Hassan, and C. von Compenhausen, “Sensory performance of blind mexican cave fish after destruction of the canal neuromasts,” *Naturwissenschaften*, vol. 77, no. May, pp. 237–239, 1990.
- [72] R. Bouffanais, G. D. Weymouth, and D. K. P. Yue, “Hydrodynamic object recognition using pressure sensing,” *Proc. R. Soc. Lond. A*, vol. 467, no. 2125, pp. 19–38, Jun. 2010.
- [73] P. W. Bearman, “On vortex street wakes,” *Journal of Fluid Mechanics*, vol. 28, no. 4, pp. 625–41, 1967.
- [74] M. M. Zdravkovich, “Smoke observations of the formation of a Kármán vortex street,” *Journal of Fluid Mechanics*, vol. 37, no. 3, pp. 491–6, 1969.
- [75] A. Ongoren and D. Rockwell, “Flow structure from an oscillating cylinder Part 1. Mechanisms of phase shift and recovery in the near wake,” *Journal of Fluid Mechanics*, vol. 191, pp. 197–223, 1988.
- [76] A. Klein and H. Bleckmann, “Determination of object position, vortex shedding frequency and flow velocity using artificial lateral line canals,” *Beilstein Journal of Nanotechnology*, vol. 2, pp. 276–83, Jan. 2011.
- [77] O. Akanyeti, R. Venturelli, F. Visentin, L. Chambers, W. M. Megill, and P. Fiorini, “What information do Kármán streets offer to flow sensing?,” *Bioinspiration & biomimetics*, vol. 6, no. 3, pp. 036001:1–12, Sep. 2011.
- [78] J. Lighthill, “Estimates of pressure differences across the head of a swimming clupeid fish,” *Phil. Trans. R. Soci. Lond. B*, vol. 341, no. 1296, pp. 129–40, 1993.
- [79] J. C. Liao, “A review of fish swimming mechanics and behaviour in altered flows,” *Philosophical transactions of the Royal Society of London. Series B, Biological sciences*, vol. 362, pp. 1973–93, Nov. 2007.
- [80] A. Quattieri, F. Rizzi, G. Epifani, A. Ernits, M. Kruusmaa, and M. De Vittorio, “Parylene-coated bioinspired artificial hair cell for liquid flow sensing,” *Microelectronic Engineering*, vol. 98, pp. 516–19, Oct. 2012.

- [81] T. Salumäe, “Design of a compliant underwater propulsion mechanism by investigating and mimicing the body of a rainbow trout (*Oncorhynchus mykiss*),” Master Thesis, Tallinn University of Technology, 2010.
- [82] K. Kaarlep, “The effect of material viscoelasticity on the performance of biomimetic tail fin actuators,” Master Thesis, Tallinn University of Technology, 2012.
- [83] C. M. Breder, “The locomotion of fishes,” *Zoologica*, vol. 4, pp. 159–297, 1926.
- [84] P. W. Webb, “The biology of fish swimming,” in *Mechanics and Physiology of Animal Swimming*, 1994, pp. 45–62.
- [85] G. Toming, “Development and characterization of a hydrodynamic test bed and a digital particle image velocimetry system,” University of Tartu, 2010.
- [86] T. Salumäe and M. Kruusmaa, “Flow-relative control of an underwater robot,” *Proc. R. Soc. A*, vol. 469, no. 2153, pp. 1–19, 2013.
- [87] R. Venturelli, O. Akanyeti, F. Visentin, J. Ježov, L. D. Chambers, G. Toming, J. Brown, M. Kruusmaa, W. M. Megill, and P. Fiorini, “Hydrodynamic pressure sensing with an artificial lateral line in steady and unsteady flows,” *Bioinspiration & Biomimetics*, vol. 7, no. 3, pp. 036004:1–12, Apr. 2012.
- [88] O. Akanyeti, L. D. Chambers, J. Ježov, J. Brown, R. Venturelli, M. Kruusmaa, and W. M. Megill, “Self-motion effects on hydrodynamic pressure sensing. Part I: Forward backward motion,” *Bioinspiration & Biomimetics*, vol. 8, no. 2, pp. 026001:1–10, 2013.
- [89] J. Ježov, O. Akanyeti, L. D. Chambers, and M. Kruusmaa, “Sensing oscillations in unsteady flow for better robotic swimming efficiency,” in *IEEE International Conference on Systems, Man, and Cybernetics*, 2012, pp. 91–96.

Appendix A

R. Venturelli, O. Akanyeti, F. Visentin, J. Ježov, L. D. Chambers, G. Toming, J. Brown, M. Kruusmaa, W. M. Megill, and P. Fiorini, “Hydrodynamic pressure sensing with an artificial lateral line in steady and unsteady flows,” *Bioinspiration & Biomimetics*, vol. 7, no. 3, pp. 036004:1–12, 2012.

Hydrodynamic pressure sensing with an artificial lateral line in steady and unsteady flows

Roberto Venturelli¹, Otar Akanyeti¹, Francesco Visentin¹, Jaas Ježov², Lily D Chambers³, Gert Toming², Jennifer Brown³, Maarja Kruusmaa², William M Megill³ and Paolo Fiorini¹

¹ Department of Informatics, University of Verona, 37134 Verona, Italy

² Centre of Biorobotics, Tallinn University of Technology, 12618 Tallinn, Estonia

³ Department of Mechanical Engineering, University of Bath, Bath BA2 7AY, UK

E-mail: otarakanyeti@yahoo.com

Received 13 October 2011

Accepted for publication 17 February 2012

Published 12 April 2012

Online at stacks.iop.org/BB/7/036004

Abstract

With the overall goal being a better understanding of the sensing environment from the local perspective of a situated agent, we studied uniform flows and Kármán vortex streets in a frame of reference relevant to a fish or swimming robot. We visualized each flow regime with digital particle image velocimetry and then took local measurements using a rigid body with laterally distributed parallel pressure sensor arrays. Time and frequency domain methods were used to characterize hydrodynamically relevant scenarios in steady and unsteady flows for control applications. Here we report that a distributed pressure sensing mechanism has the capability to discriminate Kármán vortex streets from uniform flows, and determine the orientation and position of the platform with respect to the incoming flow and the centre axis of the Kármán vortex street. It also enables the computation of hydrodynamic features which may be relevant for a robot while interacting with the flow, such as vortex shedding frequency, vortex travelling speed and downstream distance between vortices. A Kármán vortex street was distinguished in this study from uniform flows by analysing the magnitude of fluctuations present in the sensor measurements and the number of sensors detecting the same dominant frequency. In the Kármán vortex street the turbulence intensity was 30% higher than that in the uniform flow and the sensors collectively sensed the vortex shedding frequency as the dominant frequency. The position and orientation of the sensor platform were determined via a comparative analysis between laterally distributed sensor arrays; the vortex travelling speed was estimated via a cross-correlation analysis among the sensors.

(Some figures may appear in colour only in the online journal)

1. Introduction

In nature, Kármán vortex streets often occur in running water when a steady flow is obstructed by obstacles such as stones and pillars. They appear as a columnar array of vortices, shed alternately in a periodic fashion which is quantified by the vortex shedding frequency (number of vortices shed per unit time) and wake wavelength (the average downstream distance between two consecutive vortices with the same

rotational direction). In underwater locomotion studies, vortex streets offer benchmark hydrodynamic challenges as they provide energy-saving opportunities for fish [1–3] and they can be realized in laboratory conditions [4]. On the one hand, biologists are interested in understanding the underlying principles that enable fish to utilize the oncoming vortices to possibly minimize their energy consumption [1]. On the other hand, roboticists are keen to apply these principles to develop

underwater technologies with higher propulsion efficiency and stability in the presence of turbulent flows [5–7].

When a bluff cylinder is placed in the flow, a base suction region develops directly downstream, where the flow recirculates towards the object, thereby forming a favourable region for entraining fish [8, 9]. It has been reported that fish expend less energy when swimming near obstructions [2]. Further downstream the vortex formation region occurs, in which the vortices are generated and then detached at the vortex shedding point forming a ‘street’ of alternately rotating vortices.

The pioneering work of Liao *et al* [10] showed that the behaviour of a rainbow trout in the Kármán vortex street differed from steady swimming in uniform flows, when the size of the vortices was comparable with the size of the fish. Trout matched their tail beat frequency with the vortex shedding frequency and slalomed between the vortices in such a way that their centre of mass was moving in anti-phase with the vortices [11]. This correlated with a reduction in oxygen consumption [12].

With the purpose of developing low-drag energy harvesting devices, Anderson demonstrated that an oscillated rigid high aspect-ratio foil actively used less power when its motion was synchronized with the incoming vortices [13]. Beal *et al* [3] showed that a dead fish, before rigour mortis had set in, could still maintain its position in the vortex street, at least for a short period of time before being sucked into the suction zone. In the same work, subsequent experiments with a flexibly mounted hydrofoil—passively moving upstream through interaction with the available vortices without requiring any mechanical input—confirmed that the passive motion induced by the flow could produce self-propulsion.

Building on previous studies, a fish-like robot is being developed which is capable of recognizing and characterizing Kármán vortex streets through flow sensing, and of adapting its tail beat to synchronize. The mechanical design of the robot is given in [14]. On the grounds that adaptation to environmental changes is the key for autonomy, it is expected that an underwater robot should change its control strategy to enhance effective swimming with reference to the surrounding flow regime. It could possibly reduce drag by orienting itself towards the incoming flow and staying behind an obstructing object. It would also be able to adjust its control parameters, such as the tail beat frequency and amplitude, based on the detected flow speed, vortex shedding frequency and wake wavelength.

The flow-sensing capabilities of animals provide a wealth of inspiration for adaptive strategies to unsteady flow. Natural hydrodynamic receptors have an operating range of 1–150 Hz [15]. The main flow-sensing mechanism on a fish is the lateral line organ. It is composed of an array of mechano receptors, called neuromasts. These neuromasts are arranged on the surface of the fish as superficial neuromasts and in subsurface networks as canal neuromasts; they exist on both the anterior and posterior regions of the fish [16]. The combination of velocity detection by the superficial neuromasts and pressure difference by the canal neuromasts allows the animal to detect a

range of water flows. This is an interesting biological capability whose potential is worth investigating to aid the navigation systems of underwater vehicles.

In this work we focus on a flow-sensing mechanism that can be relevant to our underwater robot in unsteady flows. We present off-line methods for the analysis of the surrounding steady and unsteady flows to extract control-related information. The methods are tested by deploying off-the-shelf pressure sensors in two parallel arrays, to provide a simplistic mimic of the fish’s posterior lateral line organ. The overall goal is to better understand the sensing environment from the local perspective of a situated agent. Four sensing tasks are investigated, in particular:

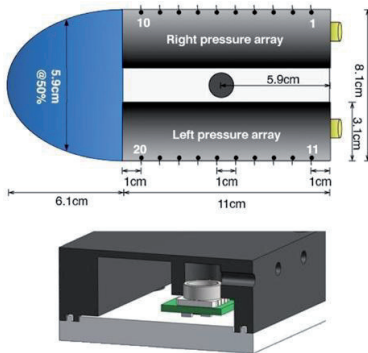
- Task 1: differentiating between steady and unsteady flows in particular the Kármán vortex street,
- Task 2: determining the orientation of the robot with respect to the incoming flow,
- Task 3: determining the lateral deviation of the robot from the centre axis of the Kármán vortex street and
- Task 4: computing hydrodynamically relevant features of the vortex street: the vortex travelling speed, the shedding frequency and the wake wavelength.

Inspired by the lateral line organ of fish, flow and pressure sensor technology is progressing rapidly to be able to measure flow-related information [17–21]. With the maturation of artificial lateral line technology, navigation in turbulent flows may become easier. In this context, what we present here is a first step towards developing on-line methods to guide underwater vehicles in unsteady flows, such as the Kármán vortex street.

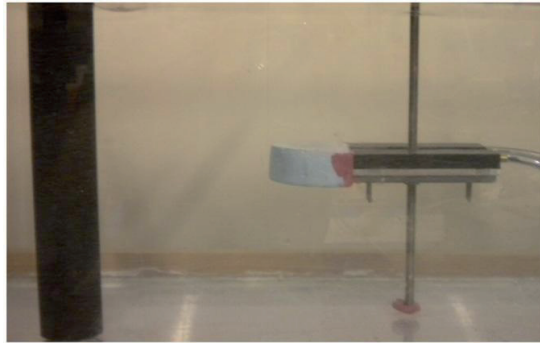
2. Material and methods

2.1. Pressure sensors

The off-the-shelf pressure sensors MS5407-AM [22] developed by Measurement Specialties TM were adapted for use in our experiments. They have a sensing unit that is micromachined from silicon, mounted on a 0.62 cm × 0.64 cm ceramic carrier and protected with a metal cap. The sensor is gel protected against humidity and water. The sensing unit is connected as a Wheatstone bridge that provides pressure readings within the range of 0–7 bar full scale and a sensitivity of 56 mV/bar. We used a 22 bit analogue to digital (AD) converter MCP3553 of Microchip Technology Inc. because of the small footprint. This choice limited the sampling rate of the sensor readings to 50 Hz. The reference voltage was 124.5 mV corresponding to ≈0.1 Pa for the least significant bit. This device employs a third-order Delta–Sigma modulator and a fourth-order digital decimation filter. High oversampling frequency of the modulator minimizes the need for any external anti-aliasing filter. To increase the signal-to-noise ratio, the AD converter was soldered directly on the printed circuit board holding the sensor without an amplification. The digital signal was carried from the AD converter to a microcontroller (ATmega324) over a serial peripheral interface bus. Data acquisition was performed using code written in LabVIEW (National Instruments, Austin, TX).



(a) Sensor platform



(b) Snapshot from an experiment

Figure 1. (a) A schematic diagram of the sensor platform. It accommodated two pressure arrays laterally distributed. Each array had ten pressure sensors measuring absolute pressure. The sensors were not interconnected; every sensor had a separate compartment with a corresponding hole. (b) A snapshot when the sensor platform was tested in the Kármán vortex street.

The sensor platform. Ten sensors were mounted in a watertight box to form a pressure array. The sensors interacted with the flow through 0.2 cm diameter holes on the side of the box which were 1 cm apart. The sensors were not interconnected; each sensor was placed in a separate compartment. To ensure water tightness, the steel rim of the sensor was pressed tightly into a machined hole in the plastic case of the array and was sealed with silicon grease. The arrays were mounted on a thin plastic plate. A U-shaped polystyrene section was mounted on the front section of the platform to achieve a more streamlined body. Figure 1 shows the experimental sensor platform and the cross section of the watertight box which contains one sensor and its electronics.

2.2. Sensor calibration

We performed a series of calibration tests in still water to estimate the value–unit (pascal) conversion factor for each sensor. We took recordings from the sensor platform at 5 and 15 cm below the water surface and measured the conversion factor by relating the theoretical pressure difference to the difference in the sensor readings at the two levels. We repeated the same set of experiments five times and obtained consistent results. For all sensors, the factor was ≈ 0.1 .

The recordings taken in still water were used as a control reference for each experimental data set. We computed the mean and the standard deviation of each sensor signal and subtracted the mean from the readings to remove the offset. In this way all pressure readings were relative to the readings in still water. By multiplying the standard deviation with the value–unit conversion factor, we estimated the pressure variance of each sensor to be around 1 Pa, a similar value to that reported by Fernandez [18]. In some experiments we observed a slight drift in the sensor readings ($\approx 0.05 \text{ Pa s}^{-1}$). This might be due to the electronics or environmental changes, for example temperature or atmospheric pressure. To ensure that the amount of drift between the start and end of the experiment was tolerable, we checked whether the sensor readings at the beginning were consistent with the readings at the end (both

in still water conditions). If there was a discrepancy of more than 5%, we repeated the experiments.

2.3. Experimental setup

The experiments were carried out in a flow channel (open to air) with a working section of $100 \times 30 \times 30 \text{ cm}^3$ (length \times width \times height). The flow was driven in a recirculating tank by a propeller with diffusers before and after the working section to generate a uniform, steady flow. A Nylatron cylinder with a diameter of 4.5 cm was placed 30 cm downstream from the diffuser that was placed at the start of the working section to generate a Kármán vortex street. In all experiments the flow speed was fixed at 20 cm s^{-1} .

Investigated scenarios. Twelve test scenarios were considered, four in the uniform flow and eight in the Kármán vortex street (figure 2). In all experiments the sensor platform was harnessed with a vertical rod and its position and orientation were adjusted manually. The depth of operation was 12 cm below the water surface at the centre of the water column. During the Kármán vortex street experiments, the nose of the sensor platform was placed 20 cm downstream from the cylinder, beyond the vortex shedding point.

Pressure readings were logged every 0.02 s (sampling rate of 50 Hz). Each experiment started with data acquisition in still water (60 s). It continued with recordings in the chosen flow regime (120 s), and after switching off the water pump, an extra minute of data was recorded to provide background and noise data.

3. Flow characterization

Before the experiments with the sensor platform, we visualized each flow regime in the Earth frame of reference using digital particle image velocimetry (DPIV). The DPIV setup has been described previously in [23], but for these experiments the field of view was $30 \times 25 \text{ cm}^2$ and a frame rate of 200 Hz was used. In the Kármán vortex street setup the cylinder was at a

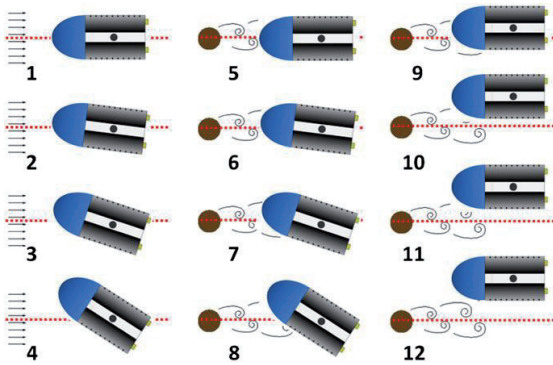


Figure 2. Investigated scenarios in the uniform flow (1–4) and in the Kármán vortex street (5–12). In all experiments the flow speed was 20 cm s^{-1} . Vortex streets were generated by placing a 4.5 cm diameter cylinder in the flow. Experiments: 1. sensor platform aligned parallel with the flow (uniform flow), 2. rotated by 15° , 3. rotated by 30° , 4. rotated by 45° , 5. sensor platform aligned parallel with the flow (Kármán vortex street), 6. rotated by 15° , 7. rotated by 30° , 8. rotated by 45° , 9. sensor platform deviated to the right from the centre by 1 cm, 10. deviated by 3 cm, 11. deviated by 5 cm and 12. deviated by 7 cm.

distance of 10 cm upstream from the leading edge of the field of view. This global analysis was useful to reveal the differences between the uniform flow and the Kármán vortex street. Furthermore, it highlighted the hydrodynamically significant features which, on the one hand, allowed us to determine a possible placement of the sensor platform (to ensure its placement downstream of the vortex shedding point), and on the other hand, offered benchmark data to evaluate the performance of the pressure sensing as presented in section 5. Figures 3(a) and (b) present a sample flow field in the uniform flow and the Kármán vortex street from the DPIV measurements.

Each flow regime was studied using a post-DPIV analysis toolbox [24]. The vorticity was minimal (observed only in 5% of the total area of the field of view) in the uniform flow. However, well-formed vortices travelling downstream were observed in the Kármán vortex street. Table 1 summarizes the characterization outcome.

Table 1. The flow features describing the Kármán vortex street through the DPIV flow analysis. The theoretical vortex shedding frequency was computed as in [25]. The spacing ratio was computed by dividing the width of the street to the average wake wavelength [26].

Setup	
Flow speed	20 cm s^{-1}
Cylinder diameter	4.5 cm
Vortex shedding frequency (theoretical)	1.1 Hz
Investigated hydrodynamic features	
Base suction length	$(5.3 \pm 0.4)\text{ cm}$
Vortex formation length	$(10.5 \pm 0.4)\text{ cm}$
Vortex shedding point	$(16.8 \pm 0.4)\text{ cm}$
Kármán vortex street width	$(6.3 \pm 0.8)\text{ cm}$
Average downstream flow speed	
Inside Kármán vortex street	$(16 \pm 1)\text{ cm s}^{-1}$
Outside Kármán vortex street	$(23 \pm 1)\text{ cm s}^{-1}$
Average vortex travelling speed	$(20 \pm 1)\text{ cm s}^{-1}$
Min/Max average vorticity	$-80/80\text{ s}^{-1}$
Vortex shedding frequency	$(1.2 \pm 0.2)\text{ Hz}$
Average wake wavelength	$(18 \pm 4)\text{ cm}$
Spacing ratio	0.35 ± 0.12
Strouhal number	0.22 ± 0.05

3.1. Recognizing a Kármán vortex street through analysis of the flow field

We propose that a Kármán vortex street can initially be distinguished from a uniform flow by analysing how the flow changes over time. We used a measure called turbulence intensity, computed as the standard deviation of the flow velocity divided by the mean flow velocity at each point [27]. The spatial distribution of the turbulence intensity is illustrated for the uniform flow in figure 4(a) and the Kármán vortex street in figure 4(b). The degree of turbulence was very low in the uniform flow, whereas in the Kármán vortex street it was high, reaching a maximum at the vortex formation point. It decayed quadratically with the distance from this point. The flow outside the Kármán vortex street was steady, as in the uniform flow.

Turbulence intensity provides information on the presence of a turbulent wake. Further information is required to distinguish the Kármán vortex street from other wakes. This

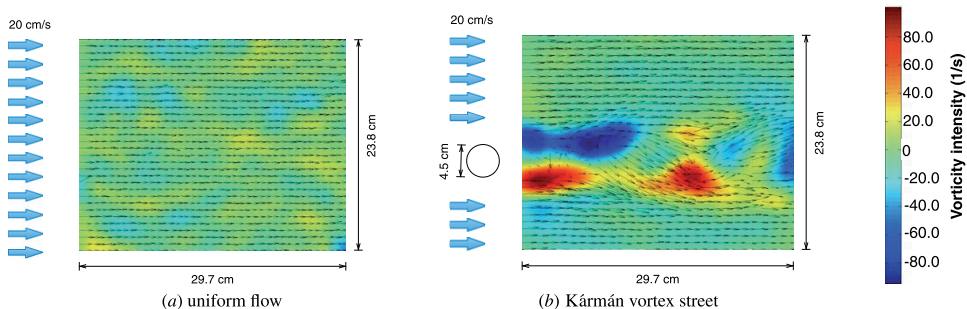


Figure 3. The velocity vector field superimposed on the vorticity field. The colour bar illustrates the vorticity where blue tones indicate the clockwise rotation and red tones the counter-clockwise rotation. (a) The flow is steady in the uniform flow. (b) Two vortex rows are visible in the Kármán vortex street.

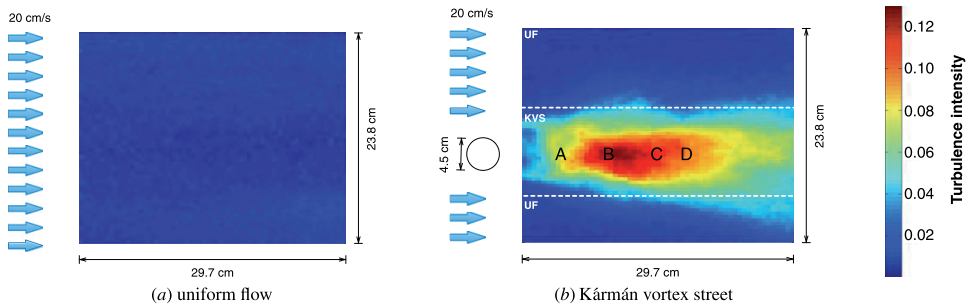


Figure 4. Turbulence intensity calculated from DPIV vectors highlights the spatial distribution of an unsteady versus a steady flow. The colour bar encodes the magnitude of the turbulence. (a) There was negligible turbulence in the uniform flow. (b) A significant amount of turbulence was detected in the Kármán vortex street, reaching a maximum at the vortex formation point. Key locations obtained by the DPIV analysis are highlighted: A. end of the base suction zone, B. vortex formation point, C. vortex shedding point and D. downstream position of the sensor platform.

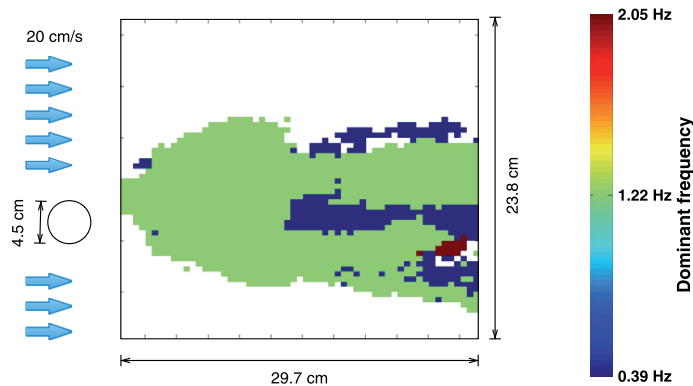


Figure 5. Regions in which the temporal behaviour of the flow was characterized by a single frequency. The colour bar specifies the frequency value of each region. The green regions with 1.2 Hz occupied the largest area. This value matched the expected vortex shedding frequency. In blue regions we still detected the vortex shedding frequency but it was not as strong as the low-frequency component. This could be due to the short observation window of the DPIV analysis in time. In white areas no dominant frequency was detected.

can be resolved using the frequency domain. The distinctive feature of the Kármán vortex street is the repeating pattern of the flow which is characterized by the vortex shedding frequency. If the temporal behaviour of the flow at a certain location can be represented by a periodic function, the probability is high for that location being a part of the Kármán vortex street. Figure 5 shows the frequency spectrum analysis performed in the Kármán vortex street. The time window for fast-Fourier-transform (FFT) analysis was 3 s. Locations in which the temporal behaviour of flow agreed with the vortex shedding frequency are highlighted in green. A Kármán corridor is clearly visible.

Overall, we can see that an approximate flow regime classification would be possible on the basis of turbulence intensity and frequency analysis; if the turbulence intensity of the flow is above a certain threshold and its temporal behaviour can be characterized by a distinct frequency, it can be labelled as a Kármán vortex street.

4. Methods to process pressure signals

In the previous section the flow features were detected and described in the Earth coordinate system. In this section we now turn to the local frame and use the onboard sensors. In each experiment, we segmented the recorded signals into 5 s observation intervals using a running window. For each observation window, we analysed the following features:

Pressure difference across sides. We computed spatio-temporal pressure averages for each pressure array. We compared the averages of the two arrays to evaluate whether the sensor platform was aligned against the flow stream and whether it was positioned at the centre of the Kármán vortex street. We postulated that when symmetry was broken either by turning or deviating from the centre, the pressure readings from the two arrays would differ.

Turbulence intensity. The turbulence intensity of the flow was estimated by looking at the fluctuations in the sensor readings.

We expected that the higher the fluctuations, the more turbulent the flow would be. For each sensor, the turbulence intensity was computed as the ratio of standard deviation of the sensor reading to the mean value over a 5 s period. We used the mean turbulence intensity on each array as the final measure. The orientation and position of the sensor platform were deduced by comparing the averages from the two pressure arrays.

Frequency spectrum analysis. The pressure signals in the frequency domain were analysed using FFT (normal bin distribution, bin size 0.2 Hz). In our preliminary investigations, it was observed that the vortex shedding frequency dominated the pressure readings obtained in the Kármán vortex street. The harmonics of the vortex shedding frequency did not appear in the frequency spectrum. We therefore proposed a method to classify the sensor signal as periodic when the frequency component with the maximum amplitude contained at least 40% of the energy of the whole signal. Here the percentage 40% was chosen intuitively depending on the strength of the Kármán vortex street and the signal-to-noise ratio of the sensors. We determined that the sensor platform was in the vortex street if the majority of sensors (more than 50%) agreed on the same frequency; this dominant frequency was then regarded as the vortex shedding frequency.

Two factors interfered with the spectral analysis; high-frequency components (around 8 Hz and its harmonics) originated from the water pump and low-frequency components (0–0.5 Hz) due to the bulk water movements. To remove these frequencies we filtered each sensor signal using a band-pass filter with the cutoff frequencies 0.5 and 5 Hz. The vortex shedding frequency was in the pass frequency range.

We note that there was a trade-off between narrow frequency selectivity and responsiveness of the frequency detection method. As the duration of the signal used in the FFT analysis increased, the frequency resolution increased enabling us to distinguish between neighbouring frequencies. However, observing a signal for longer periods increased the reaction time. We therefore chose the minimum observation window (5 s) as three periods of the lowest frequency component in our range (0.6 Hz).

Cross-correlation analysis. We evaluated a cross-correlation among sensors (a measure of the similarity of two waveforms as a function of time lag applied to one of them) to estimate the vortex travelling speed. We chose two sensors along the same pressure array and computed the time difference from the first to the second sensor that provided the maximum correlation. We assumed that the difference would represent the time needed for a vortex to travel from one sensor to the other. The ratio between the spacing of the sensors and the time delay would provide an estimate of the travelling speed. For statistical verification, we repeated the same procedure for all the combinations of sensor pairs with spacing bigger than 3 cm. The average speed and its confidence intervals were evaluated based on the histogram analysis.

The choice of sensor spacing depended on the interaction between the sampling rate of the sensors and the range of flow speeds. In the range of 15–30 cm s⁻¹ with 0.02 s time

resolution, working with the sensors less than 3 cm apart would introduce errors greater than 20%. The speed estimation improved with increasing distance between the pairs. We explored the whole range varying from 3 to 9 cm (maximum available distance between the first and the last sensor in each array). The maximum distance was acceptable for the correlation analysis as it remained smaller than the wake wavelength and so prevented spatial aliasing.

Wake wavelength. After evaluating the flow speed and the vortex shedding frequency, the wake wavelength was computed by dividing the travelling speed by the vortex shedding frequency. It was estimated at 30 cm downstream from the cylinder.

5. Results

This section presents the analysis of pressure signals obtained by the two sensor arrays.

5.1. Task 1: comparison between the Kármán vortex street and uniform flow

We first qualitatively highlight the differences between the uniform flow and the Kármán vortex street by comparing the spacetime representation of the pressure signals as perceived by the sensor platform (figure 6). In both circumstances the sensor platform was oriented towards the flow.

For both pressure arrays, large irregular patterns were detected in the uniform flow. The patterns, on the contrary, were more organized in the Kármán vortex street; low- and high-pressure regions alternated sequentially, as inclined regions. For each sensor, the horizontal distance between the two consecutive regions indicated the recurrence period, which was in accordance with the vortex shedding frequency (≈ 1.2 Hz; see table 1). Also, each region had a negative gradient suggesting that an event, presumably associated with an oncoming vortex, was first felt by the sensors at the anterior parts (s_1 and s_{11}). Subsequently, it was detected by the other sensors in an orderly fashion as it travelled along the array. The delay in the detection time was related to the travelling speed. It was computed from the gradient as 20 cm s⁻¹ matching the incoming flow speed.

Hydrodynamic features—spatio-temporal pressure average, turbulence intensity and dominant frequency—were compared in figure 7. The data sets of the uniform flow and the Kármán vortex street were cascaded for illustration purposes. The average pressure readings in both flow regimes were 30 Pa lower than the ones in still water. In either case no pressure difference was observed between the right and left arrays (figure 7(b)).

The turbulence intensity measured in the Kármán vortex street was $\approx 30\%$ higher than that measured in the uniform flow (figure 7(c)). This favours turbulence intensity as a valid marker to differentiate steady from unsteady flow. In general, the average flow fluctuations on both sides of the sensing platform were similar except during the period of $100 \text{ s} < t < 140 \text{ s}$ where the turbulence intensity measured by the right pressure array was significantly higher.

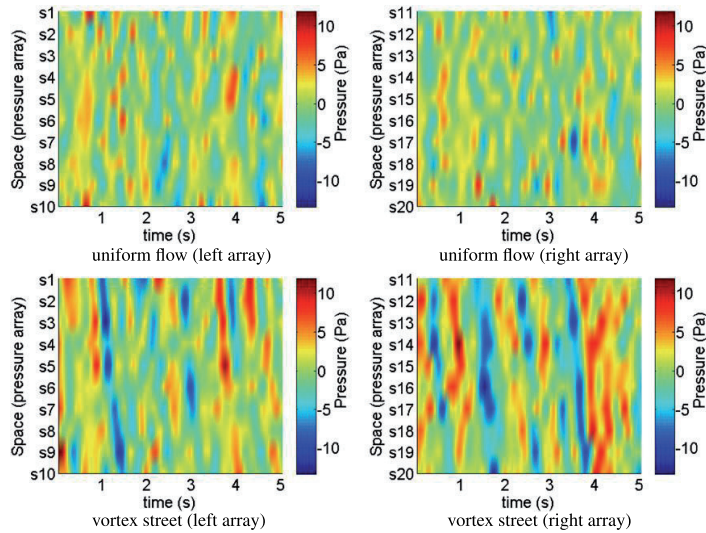


Figure 6. Snapshots of the pressure readings as they were observed in a 5 s interval: the vortex street and the uniform flow. The readings were band-pass filtered. The red tones highlight the regions where the instantaneous pressure was positive and the blue tones highlight the regions where the instantaneous pressure was negative. The colour bar shows the encoding between the colour and the pressure. One can recognize the vortex street as low- and high-pressure regions arranged in an order, alternating slightly quicker than every second.

Figure 7(d) shows the colour-encoded dominant frequency measured by each sensor. Green, corresponding to 1.2 ± 0.3 Hz, was the dominant colour/frequency in the Kármán vortex street which matched the vortex shedding frequency. The number of sensors detecting the vortex shedding frequency at a time was usually higher than 10 (more than 50%, 17/24 times of 5 s observation windows, figure 7(e)). The colour distributions, on the other hand, were quite random in the still water and the uniform flow (figure 7(d)). No established sensor consensus over time was observed in either flow regime. The number of sensors in agreement was usually less than 10 (<50%) (figure 7(e)). The results validate the method of dominant frequency analysis to recognize the Kármán vortex street.

Yet, when the flow was in a transient state (changing from still water to a vortex street/uniform flow and vice versa), there were occasions in which the sensors measured 0.6 Hz as the dominant frequency. This is due to the gradual change in the magnitude of the sensor measurements as the flow regime was changed from one to another.

5.2. Task 2: turning the sensor platform away from the flow axis

Pressure difference. Figures 8(a) and (b) compare the pressure averages of the right and left pressure arrays in the uniform flow and the Kármán vortex street, as the sensor platform was turned away from the flow axis. The rotations were clockwise from an angle of 0° (oriented towards the flow) to 45° with a step of 15° .

In the uniform flow the pressure difference increased as the platform was rotated through an increased angle. With the assumption that the flow around the platform remained

uniform, the flow velocity and pressure, in the boundary layer, were inversely related (Bernoulli’s law). When the platform was facing the flow, the flow streamlines around the body were symmetric and the pressure on both sides of the body was equal. By turning the platform, the streamlines of the flow were forced to curve around the body by differing amounts for each side. This curving of the streamlines gave faster flow on the right side of the body, and slower flow on the left side of the body, leading to higher pressure on the left-hand side. This resulted in the pressure difference across the two sides of the platform (figure 8(a)). The higher the turning angle, the bigger the pressure difference. The difference was around 10 Pa at an angle of 45° .

In the Kármán vortex street the pressure difference on the platform increased with the turning angle (figure 8(b)). However, this time at every angle the difference was twice as large as that in the uniform flow (i.e. 20 Pa at an angle of 45°).

Turbulence intensity. Figures 9(a) and (b) show the average turbulence intensity measured by the pressure arrays in both of the flow regimes with respect to the turning angle. In the uniform flow, the degree of turbulence did not change with the orientation of the platform; it was always lower than 3.8×10^{-5} , which was recognized as an empirical threshold. There was also no difference in the measured turbulence by the right and left pressure arrays. In contrast, the turbulence intensity in the Kármán vortex street was consistently above 3.8×10^{-5} , allowing us to distinguish between the two flow regimes. At the same time, more turbulence was detected by the pressure array on the left-hand side. The difference in turbulence increased proportionally with the rotation angle. The higher turbulence on the left-hand side can be explained by having sensors on the left which were more exposed to the oncoming vortices.

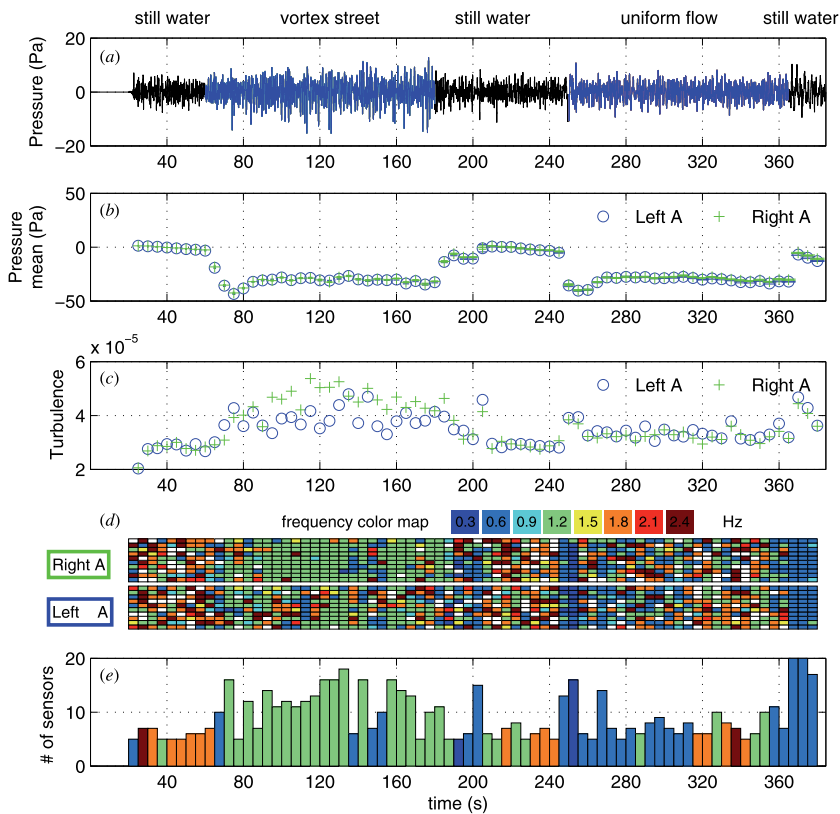


Figure 7. Analysis of pressure readings in the Kármán vortex street ($60\text{ s} < t < 180\text{ s}$) and in the uniform flow ($240\text{ s} < t < 360\text{ s}$). The data were cascaded from experiments 1 and 5 for illustration purposes. In both flow regimes, the sensor platform was oriented against the flow. (a)–(e): (a) Pressure readings from sensor 5 (band-pass filtered). (b) Spatio-temporal pressure averages of right (green) and left (blue) sensor arrays. (c) Turbulence intensity. (d) Frequency that was sensed most by each sensor. The frequency represented by each colour is shown in the key. Green at 1.2 Hz is the dominant colour/frequency in the vortex street which matched the theoretical vortex shedding frequency. (e) Maximum number of sensors that measured the same frequency. Usually, more than 10 sensors detected the vortex shedding frequency at the same time. Each data point in (b)–(e) was computed by analysing the readings over a period of 5 s.

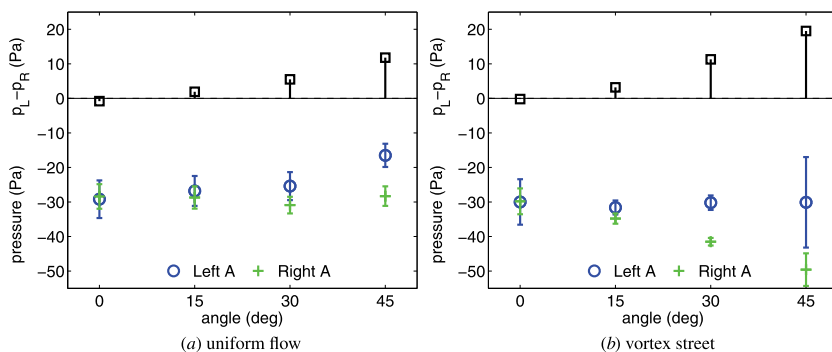


Figure 8. Spatio-temporal pressure averages of the right (p_R)/left (p_L) sensor arrays. Pressure differences ($p_R - p_L$) are also shown on top. Each data point was computed based on 120 s data sets obtained from experiments 1 to 8.

Number of sensors detecting the vortex shedding frequency. The number of sensors detecting the vortex shedding frequency also changed as the platform rotated (figure 10(a)). The number on the left increased gradually depending on the angle of

rotation (after an angle of 15°). An increase in both the turbulence intensity and sensor agreement suggests that the sensors of the left pressure array detected the vortex street more intensely as the platform was rotated.

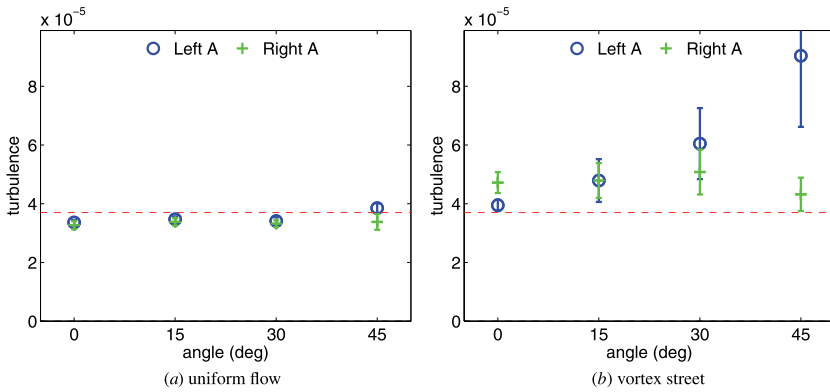


Figure 9. Average turbulence intensity of the right/left pressure arrays. The red-dashed line points to an empirical threshold to differentiate the uniform flow from the vortex street.

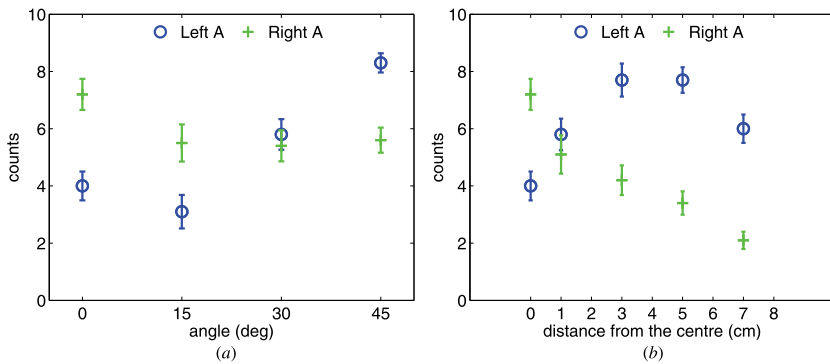


Figure 10. (a) Number of sensors detecting the vortex shedding frequency as a function of rotation angle. (b) Number of sensors detecting the vortex shedding frequency as a function of deviation from the centre axis of the vortex street.

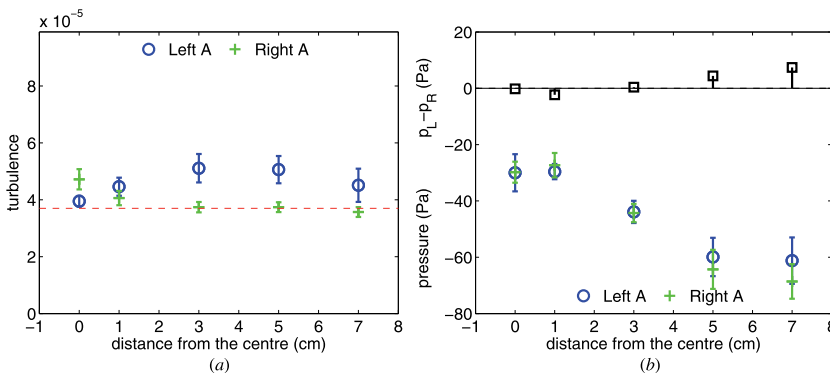


Figure 11. (a) Turbulence intensity and (b) pressure response of the arrays as a platform moved to the right from the centre axis of the vortex street. The red-dashed line points to an empirical threshold to differentiate the uniform flow from the vortex street.

5.3. Task 3: moving the sensor platform away from the centre line of the Kármán vortex street

We investigated the number of sensors detecting the vortex shedding frequency as the sensor platform deviated from the centre axis of the vortex street (figure 10(b)). The sensor

agreement on the right-hand side decreased with the distance. When the centre of the platform was 3 cm away, the number was already less than half suggesting an exit from the vortex street. After this point the degree of turbulence also dropped into the uniform flow range (figure 11(a)). Overall, the width

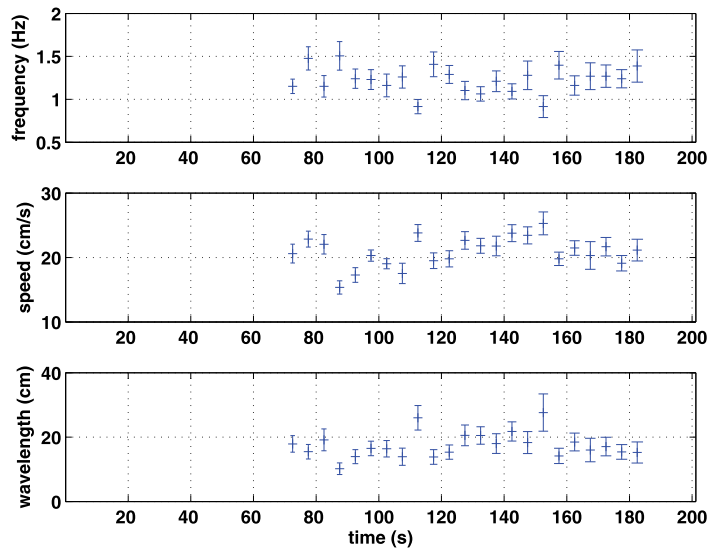


Figure 12. Vortex shedding frequency, vortex travelling speed and wake wavelength estimations over the course of the Kármán vortex street ($60\text{s} < t < 180\text{s}$, experiment 5). The sensor platform was oriented parallel with the flow stream. Each data point was estimated over a 5 s observation window. The measurements corresponded to the part of the Kármán vortex street between 20–30 cm away from the cylinder.

of the Kármán vortex street was roughly estimated as 6 cm, which agreed with the DPIV measurement.

The trend for the left sensors was parabolic, both for the number of sensors detecting the vortex shedding frequency and the turbulence intensity. In both figures 10(b) and 11(a), the maximum values were measured when the sensor platform was 3 to 5 cm away from the centre. In this range, the position of the sensors on the left-hand side corresponded to the middle of the street.

Figure 11(b) shows the average pressure measured by the pressure arrays. Both arrays sensed lower pressure as the platform was deviated from the centre. After a deviation distance of 3 cm, the pressure dropped faster on the right side. This could be related to the faster flow in the free-stream flow outside the Kármán vortex street.

5.4. Task 4: estimating the vortex shedding frequency, the travelling speed and the wake wavelength

Previously in task 1, we demonstrated that the vortex shedding frequency can be measured via the dominant frequency analysis using FFT and the value was 1.2 ± 0.3 Hz. In this section, we focused on estimating the vortex travelling speed and the wake wavelength. The vortex travelling speed was computed by the cross-correlation analysis between the sensor pairs. The wake wavelength was determined by dividing the estimated travelling speed by the vortex shedding frequency. Figure 12 shows the vortex shedding frequency, the travelling speed and the wake wavelength over the course of the entire data set, when the sensor platform was in the middle of the Kármán vortex street. For each data point, we used a 5 s time window to calculate the correlations. Both arrays estimated

a similar speed with an average of 21 ± 5 cm s^{-1} . This resulted in an average wavelength of 18 ± 5 cm. Both values matched the results from the DPIV analysis (table 1). When we rotated the sensor platform, we were still able to calculate the aforementioned features accurately, especially on the left side where the fluctuations were still high.

6. Discussion

Typically, flow is visualized in the Earth frame of reference (as for example in figure 3). A robot, fish or other agent operating within the flow does not have access to this perspective, and so it requires a system which converts local information (onboard sensing) into a global understanding in order to facilitate active control. Developing the capability of an underwater vehicle to navigate in a wake is motivated in part by the following: drafting in the wakes of objects provides a shelter from the bulk flow and positions the craft to potentially exploit any useful hydrodynamic features.

In a previous study [23], we showed how a linear array of virtual sensors could be used as a local proxy for the global DPIV-derived velocity vector field. In this paper we implemented a real sensor array. Inspired by the lateral line of fish, we built a simple artificial lateral line using a bilateral linear array of low-cost pressure sensors. These were distributed laterally on the sides of a streamlined rigid body to sample the hydrodynamic environment. Using this device, and comparing its readings to the velocity vector field of the same flow, we have investigated the pressure fluctuations for sensing information. We have demonstrated that it is possible to detect complex flow structures, and specifically to detect the presence of the Kármán vortex street within the bulk flow

(task 1), recover the position and orientation of the sensor platform (tasks 2 and 3) and compute the vortex shedding frequency, travelling speed and average downstream distance between two consecutive vortices of the same rotation (task 4).

The method used here to identify the Kármán vortex street is based on measures of turbulence intensity and sensor consensus on the dominant frequency. Estimated from the pressure data, the average turbulence intensity in the Kármán vortex street was 30% higher than its counterpart in the uniform flow and at least 50% of the sensors were simultaneously detecting the vortex shedding frequency as the dominant frequency.

We can determine the orientation of the sensor platform relative to the oncoming flow by analysing the pressure difference across the sides. This is possible as the physical presence of the sensor platform itself reconfigures the flow around the sensors. When the platform was aligned into the flow, the spatio-temporal pressure averages measured by each array were equal. When we turned the platform in a clockwise direction, a pressure difference proportional to the turning angle was observed. In both flow regimes the larger the angle, the larger the pressure difference.

Finally, we determined the vortex travelling speed by analysing cross-correlations among the sensors on each array. A similar technique was proposed in biological studies to analyse lateral line afferent signals with the purpose of estimating the flow speed [28]. The average downstream distance between the vortices was then calculated by dividing the estimated speed by the vortex shedding frequency. We see that even though the key hydrodynamic features exhibit changes over the entire observation window (the vortex shedding frequency and travelling speed change by 24% and the wake wavelength changes by 33%), they can still be identified using our bilateral pressure sensing array.

This study has certain limitations. The analysis was narrowed to specific flow conditions in order to accommodate the low resolution, sampling rate and the signal-to-noise ratio of the sensors. The methods presented are off-line methods requiring a certain amount of processing time, which can be an issue in real-time applications.

Furthermore, there are other periodic, single frequency wakes available to sense in the underwater environment. For example, dipole sources and reverse Kármán vortex streets would be identified using the same markers. Although we can detect a wake and the bulk flow movement, the ability to discriminate local directionality in the flow is limited with only a pressure array. Our information processing provides us with the knowledge about the flow features, but our ability to discriminate between different types of events is restricted. In the biological lateral line this may be achieved through their combined velocity and pressure gradient sensing capability [29]. The lateral line organ is organized with many hundreds to thousands of sensors that are distributed in a specific pattern providing directional sensitivity [30]. Some of these shortcomings could be overcome in future by the development of a better biomimetic artificial lateral line using velocity detection flow sensors (e.g. [17, 19, 20]) coupled with the pressure sensor array.

The term ‘distant touch’ [16] has been used to describe the role of the lateral lines of fish and its ability to localize hydrodynamic stimulus sources [29, 31]. Previous researchers have deployed flow-sensing, artificial lateral line arrays to realize this sensing mechanism. Surface flow sensors in a single array have been shown to be capable of locating an underwater vibrating source in the near field and hydrodynamic wakes further afield [32]. A bilateral artificial lateral line canal with optical sensors inside has been proven to be sufficient to detect objects passing by, bulk flow velocity and vortices caused by an upstream cylinder [21], while a linear pressure array has been shown to be capable of object identification and vortex tracking [18]. The bilateral arrangement used in this study, coupled with the sensor consensus and signal processing, expands on this and provides information on the sensor platform orientation relative to the wake, and on the absolute and changing pressure distribution over the body as it is rotated in both steady and unsteady flows.

Complementary to the obvious engineering applications, the results we present here provide a tool for testing hypotheses about how a fish might use its lateral line to sense the features of its environment. One of the challenges that has been identified in lateral line research is the perception of signal in noise [29]. We have shown here that frequency patterns in the wake of an object can be detected by pressure sensors alone and it is possible to detect these patterns even in noisy real-world flows. We also show that consensus between multiple parallel sensors aids in the identification of the hydrodynamic signal in the fluid noise. Further research into these two aspects of our artificial sensor system may help to explain the complex distribution and abundance of neuromasts in the fish lateral line system.

We demonstrate here that our device, based on robust pressure sensors, is able to extract features from the flow such as the vortex shedding frequency, travelling speed and wake wavelength, even in a real-world, particle-laden, flowing water environment, which are useful for identifying objects upstream. This was partially realized on a free-swimming fish-like robot composed of a head and actuated flexible tail. A closed-loop controller was built into the robot which used the pressure difference across the head as sensor feedback to orient the robot towards the incoming uniform flow [33]. By using two of our modified pressure sensors, distributed either side of the head, an orientating response to the flow was achieved. The preliminary results are encouraging and they favour Montgomery’s assertion that the lateral line organ can mediate rheotaxis in fish [34].

We conclude that a spatially distributed sensing system is advantageous for underwater robot navigation. Compared to measurements from a single sensor, collective sensing reduces the amount of computational uncertainty. Moreover, we find that spatial and temporal analysis of pressure measurements leads to accurate estimation of flow speed and vortex shedding frequency. Comparative analysis, especially between laterally distributed sensors, provides useful information to determine the position and orientation of the platform.

Acknowledgments

This work is carried out under the FILOSE project, supported by the European Union, seventh framework programme (FP7-ICT-2007-3).

References

- [1] Liao J C 2004 Neuromuscular control of trout swimming in a vortex street: implications for energy economy during the Kármán gait *J. Exp. Biol.* **206** 3495–506
- [2] Cook C L and Coughlin D J 2010 Rainbow trout *Oncorhynchus mykiss* consume less energy when swimming near obstructions *J. Fish Biol.* **77** 1716–23
- [3] Beal D N, Hover F S, Triantafyllou M S, Liao J C and Lauder G V 2006 Passive propulsion in vortex wakes *J. Fluid Mech.* **549** 385–402
- [4] Zdravkovich M M 1997 *Flow Around Circular Cylinders Vol. 1: Fundamentals* (Oxford: Oxford University Press)
- [5] Read D A, Hover F S and Triantafyllou M S 2003 Forces on oscillating foils for propulsion and maneuvering *J. Fluids Struct.* **17** 163–83
- [6] Bandyopadhyay P R, Beal D N and Menozzi A 2008 Biorobotic insights into how animals swim *J. Exp. Biol.* **211** 206–14
- [7] Epps B P, Valdivia A P, Youcef-Toumi K and Techet A H 2009 Swimming performance of a biomimetic compliant fish-like robot *Exp. Fluids* **47** 927–39
- [8] Webb P W 1998 Entrainment by river chub *Nocomis micropogon* and smallmouth bass *Micropterus dolomieu* on cylinders *J. Exp. Biol.* **201** 2403–12
- [9] Przybilla A, Kunze S, Rudert A, Bleckmann H and Brücker C 2010 Entraining in trout: a behavioural and hydrodynamic analysis *J. Exp. Biol.* **213** 2976–886
- [10] Liao J C, Beal D N, Lauder G V and Triantafyllou M S 2003 The Kármán gait: novel body kinematics of rainbow trout swimming in a vortex street *J. Exp. Biol.* **206** 1059–73
- [11] Liao J C 2007 A review of fish swimming mechanics and behaviour in altered flows *Phil. Trans. R. Soc. B* **362** 1973–93
- [12] Taguchi M and Liao J C 2011 Rainbow trout consume less oxygen in turbulence: the energetics of swimming behaviours at different speeds *J. Exp. Biol.* **214** 428–1436
- [13] Anderson J M 1996 Vorticity control for efficient propulsion *PhD Thesis* (Cambridge, MA: Massachusetts Institute of Technology)
- [14] Daou E H, Salumäe T, Ristolainen A, Toming G, Listak M and Kruusmaa M 2011 A bio-mimetic design and control of a fish-like robot using compliant structures *Proc. IEEE Int. Conf. on Advanced Robotics* pp 563–8
- [15] Bleckmann H 1994 Reception of hydrodynamic stimuli in aquatic and semiaquatic animals *Progress in Zoology* vol 41 ed W Rathmayer (Jena: Gustav Fischer-Verlag) pp 1–115
- [16] Dijkgraaf S 1963 The functioning and significance of the lateral-line organs *Biol. Rev.* **38** 51–105
- [17] Chen J and Liu C 2003 Development and characterization of surface micromachined, out-of-plane hot-wire anemometer *J. Microelectromech. Syst.* **12** 979–88
- [18] Fernandez V I 2011 Performance analysis for lateral-line-inspired sensor arrays *PhD Thesis* (Cambridge, MA: Massachusetts Institute of Technology)
- [19] Yang Y, Nguyen N, Chen N, Lockwood M, Tucker C, Hu H, Bleckmann H, Liu C and Jones D L 2010 Artificial lateral line with biomimetic neuromasts to emulate fish sensing *Bioinspir. Biomim.* **5** 016001
- [20] Quattieri A, Rizzi F, Todaro M T, Passaseo A, Cingolani R and De Vittorio M 2011 Stress-driven AlN cantilever-based flow sensor for fish lateral line system *Microelectron. Eng.* **88** 2376–8
- [21] Klein A and Bleckmann H 2011 Determination of object position, vortex shedding frequency and flow velocity using artificial lateral line canals *Beilstein J. Nanotechnol.* **2** 276–83
- [22] Measurement Specialties, MS54XX miniature SMD pressure sensor, datasheet available online at <http://www.meas-spec.com/downloads/MS54XX.pdf>
- [23] Akanyeti O, Venturelli R, Visentin F, Chambers L, McGill M W and Fiorini P 2011 What do Kármán streets offer to flow sensing? *Bioinspir. Biomim.* **6** 036001
- [24] Visentin F, Fiazza M C, Akanyeti O, Venturelli R and Fiorini P 2011 Towards Flow-sensing robots: situated analysis for PIV flow imaging *Proc. IEEE Int. Conf. on Advanced Robotics* pp 606–12
- [25] Chagnaud B P, Bleckmann H and Hofmann M 2007 Kármán vortex street detection by the lateral line *J. Comp. Physiol. A* **193** 753–63
- [26] Vogel S 1996 *Life in Moving Fluids: The Physical Biology of Flow* (Princeton, NJ: Princeton University Press)
- [27] Webb P W and Cotel A J 2010 Turbulence: Does vorticity affect the structure and shape of body and fin propulsors? *Integr. Comp. Biol.* **50** 1155–66
- [28] Chagnaud B P, Brücker C, Hofmann M and Bleckmann H 2008 Measuring flow velocity and flow direction by spatial and temporal analysis of flow fluctuations *J. Neurosci.* **28** 447–4487
- [29] Bleckmann H and Zelick R 2009 Lateral line system of fish *Integr. Zool.* **4** 13–25
- [30] Schmitz A, Bleckmann H and Mogdans J 2008 Organization of the superficial neuromast system in goldfish *Carassius auratus* *J. Morphol.* **269** 751–61
- [31] Coombs S 1994 Nearfield detection of dipole sources by the goldfish (*Carassius auratus*) and the mottled sculpin (*Cottus bairdi*) *J. Exp. Biol.* **190** 109–29
- [32] Yang Y, Chen J, Engel J, Pandya S, Chen N, Tucker C, Coombs S, Jones D G and Liu C 2006 Distant touch hydrodynamic imaging with an artificial lateral line *Proc. Natl Acad. Sci. USA* **103** 18891–5
- [33] Salumäe T, Rañó I, Akanyeti O and Kruusmaa M 2012 Against the flow: a Braitenberg controller for a fish robot. *IEEE J. Robot. Autom.* at press
- [34] Montgomery J C, Baker C F and Carton A G 1997 The lateral line can mediate rheotaxis in fish *Nature* **389** 960–3

Appendix B

O. Akanyeti, L. D. Chambers, J. Ježov, J. Brown, R. Venturelli, M. Kruusmaa, and W. M. Megill, “Self-motion effects on hydrodynamic pressure sensing. Part I: Forward backward motion,” *Bioinspiration & Biomimetics*, vol. 8, no. 2, pp. 026001:1–10, 2013.

Self-motion effects on hydrodynamic pressure sensing: part I. Forward–backward motion

Otar Akanyeti¹, Lily D Chambers², Jaas Ježov³, Jennifer Brown²,
Roberto Venturelli⁴, Maarja Kruusmaa³, William M Megill²
and Paolo Fiorini⁴

¹ The Whitney Laboratory for Marine Science, University of Florida, FL 32080, USA

² Department of Mechanical Engineering, University of Bath, BA2 7AY, UK

³ Centre of Biorobotics, Tallinn University of Technology, 12618, Tallinn, Estonia

⁴ Department of Computer Science, University of Verona, I-37134, Verona, Italy

E-mail: otarakanyeti@yahoo.com

Received 15 October 2012

Accepted for publication 8 January 2013

Published 6 March 2013

Online at stacks.iop.org/BB/8/026001

Abstract

In underwater locomotion, extracting meaningful information from local flows is as desirable as it is challenging, due to complex fluid-structure interaction. Sensing and motion are tightly interconnected; hydrodynamic signals generated by the external stimuli are modified by the self-generated flow signals. Given that very little is known about self-generated signals, we used onboard pressure sensors to measure the pressure profiles over the head of a fusiform-shape craft while moving forward and backward harmonically. From these measurements we obtained a second-order polynomial model which incorporates the velocity and acceleration of the craft to estimate the surface pressure within the swimming range up to one body length/second ($L s^{-1}$). The analysis of the model reveals valuable insights into the temporal and spatial changes of the pressure intensity as a function of craft's velocity. At low swimming velocities ($< 0.2 L s^{-1}$) the pressure signals are more sensitive to the acceleration of the craft than its velocity. However, the inertial effects gradually become less important as the velocity increases. The sensors on the front part of the craft are more sensitive to its movements than the sensors on the sides. With respect to the hydrostatic pressure measured in still water, the pressure detected by the foremost sensor reaches values up to $300 Pa$ at $1 L s^{-1}$ swimming velocity, whereas the pressure difference between the foremost sensor and the next one is less than $50 Pa$. Our results suggest that distributed pressure sensing can be used in a bimodal sensing strategy. The first mode detects external hydrodynamic events taking place around the craft, which requires minimal sensitivity to the self-motion of the craft. This can be accomplished by moving slowly with a constant velocity and by analyzing the pressure gradient as opposed to absolute pressure recordings. The second mode monitors the self-motion of the craft. It is shown here that distributed pressure sensing can be used as a speedometer to measure the craft's velocity.

(Some figures may appear in colour only in the online journal)

1. Introduction

For upcoming underwater autonomous vehicles, the hydrodynamic flow and pressure sensing offer great potential

to pick up control related information embedded in the surrounding fluid, which is usually invisible to other sensor modalities such as vision and sonar. Its biological equivalent is the lateral line organ composed of modified

hair cells distributed across and along the body of fish and some invertebrates making up the acoustico-lateralis system [1]. Vibrations are detected by the mechanoreceptors and transmitted as electrical signals to the brain, providing the animal with flow velocity and pressure difference signals [2].

Desired information from this sensor array may refer to detection of nearby objects, recognition of flow regimes and their hydrodynamic features or assessment of self-motion, which can all be incorporated into a general control method to achieve enhanced swimming performances.

Extrapolating contextual cues from local flow and pressure profiles, however, is challenging due to the dynamic interaction of fluids and structures. Flow sensors do not only sense external stimuli but they are also sensitive to the perturbations caused by the self-motion of the vehicle. These perturbations would alter the flow around the body and could disguise the desired stimuli.

The ability to moderate self-generated sensor signals has been discussed in fish [3–6]. Yet within engineering, little is known on how to single out the desired control information from superimposed flow sensor readings. Experiments are usually conducted in a controlled environment, where the sensing platform is held stationary in the presence of a single stimulus. Dipole source localization [7], object recognition [8] and tracking [9], detection of flow velocity and vortex shedding frequency [10] and local analysis of steady flows and Kármán vortex streets [11] are some of the major studies reported in the literature.

The mentioned studies are important to progressively characterize the hydrodynamic signatures coming from external sources in terms of intensity and temporal/spatial profiles. However, to better understand the effects of these signals, we also need to know the background sensing picture of our vehicle generated by its own motion.

Our understanding of self-generated pressures is limited to steady, forward motion. With the assumption that the flow around an object is streamlined, the relationship between flow velocity and pressure is described by the Bernoulli law; the pressure is inversely proportional to the square of the magnitude of velocity. The highest pressure point (stagnation point) is where the velocity approaches zero on an intercepting surface and is expected to be at the foremost point of the object. The pressure profile decreases toward the sides of the object due to the accelerated flow. These arguments are supported by Dubois' pioneering work described in [12], where he actually measured the pressure distribution on the body of upstream swimming fish using pressure taps.

In theoretical studies, the stagnation point is taken as a reference to compute the velocity and pressure profiles over the object. These profiles strictly depend on the shape of the object and its orientation into the flow. One way is to start with the potential flow solution for a circular cylinder in an ideal fluid and modify it using conformal map projections such as the Joukowski transform. This approach has been widely applied in a range of aerodynamic applications [13, 14]. Hassan's mathematical model in [15] looked at the fluid-structure interaction for a three-dimensional fish shaped object. Flow field based pressure estimations were studied in [16, 17].

The focus of this paper is to analyze how pressure distribution over the head of a fusiform-shape craft is influenced while moving in an unsteady manner. We oscillate the craft forward and backward in still water and in steady flows. The geometry of the craft, with $L = 27$ cm, was inspired from a rainbow trout. On-board, miniature sensors, distributed laterally around the head, were used to measure the local pressure. The relationship between motion and pressure signals was obtained empirically through the NARMAX (nonlinear auto-regressive moving average models with exogenous inputs) system identification process. Starting with the general Bernoulli equation, the NARMAX process was used to identify the important model terms and estimate their coefficients based on the experimental data.

The resultant model is a second order polynomial which incorporates the position of sensors, swimming velocity and acceleration of the craft to predict the local pressure readings. A transparent model such as this reveals the relationship between the craft's motion and pressure signals across varying swimming speeds. It also provides a tool to quantitatively investigate sensor spacing to focus on external or self-generated flow.

2. Materials and methods

2.1. Flow tank

The experiments were conducted in the flow tank of Ocean Technologies Laboratory, University Bath. An open-air channel, with a working section of $93 \times 40 \times 36$ cm³, was bounded by collimators at either end to generate steady flow. The flow was re-circulated using a propeller. The flow within the working section was characterized using digital particle image velocimetry, which showed that steady flow was produced with negligible turbulence [11]. All testing in the flow tank was carried out in the center of the working section.

2.2. Sensing platform

The experimental craft had a fusiform-shape with an ellipsoid cross-section and geometry as detailed in figure 1. It has a passive rigid tail and pressure tapped head made of polyamide powder, manufactured using rapid prototyping and lacquer coated. The aspect ratio of the craft excluding the caudal fin, is 1 : 1.8 : 4.5. Inside the head section there are 33 holes where pressure sensors can be connected via silicon tubing. The diameter of the holes is 2 mm. The pressure sensors are sealed into a watertight box along with the electronics necessary to acquire the data.

Pressure data were recorded from nine holes distributed laterally on the horizontal plane intersecting the tip of the craft. Figure 2 shows the distribution of the holes as seen from the top and their position in polar coordinates (r, θ) with respect to the reference coordinate (x_0, y_0) , which is a point midway between the sensors p_1 and p_9 . Sensor p_5 is found on the most anterior point. Sensors p_1 and p_9 are, respectively, on the rightmost and leftmost sides of the craft.

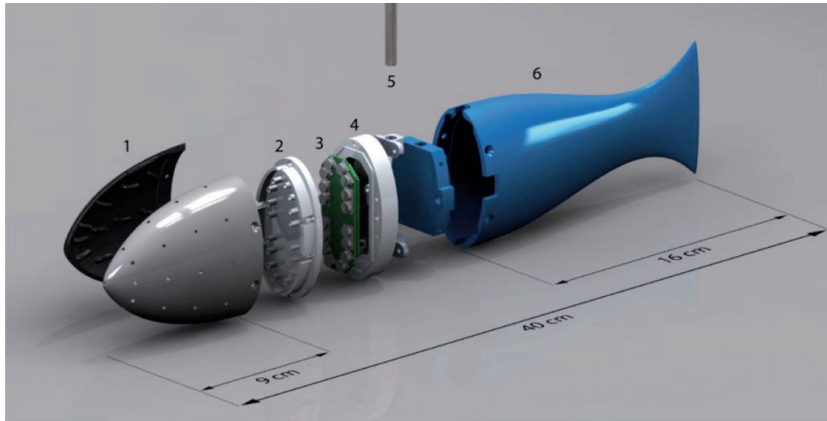


Figure 1. Schema of the sensing platform (craft). The craft’s total body length was 27 cm when its components were assembled. Components: 1—head and the pressure holes; 2—silicon tube connectors; 3—pressure sensors and electronics; 4—head-tail-rod connector; 5—rigid rod; 6—rigid tail.

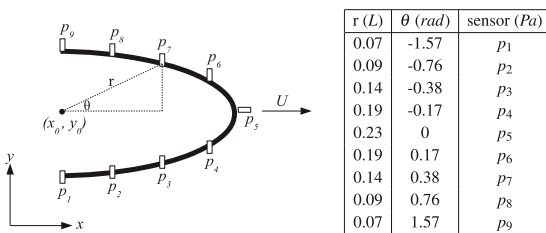


Figure 2. Distribution of nine pressure sensors around the head. U is the velocity of the craft in the x direction, with positive value indicating forward motion. The position of each sensor in polar coordinates is given on the right-hand side.

2.3. Pressure sensors and data acquisition

The pressure sensors and their circuitry were designed to fit in the craft for onboard sensing. Commercial pressure sensors MS5401-AM from Measurement SpecialtiesTM were used. These pressure sensors have a 240 mV bar⁻¹ sensitivity and 0–1 bar full scale range. The sensing unit in the MS5401-AM is connected as a Wheatstone bridge. The differential signal from each pressure sensor was filtered with a simple C filter to eliminate high frequency noise before amplification. The signal was amplified with a gain of 13.67 using an amplifier AD8226ARMZ developed by Analog Devices Inc. The single-ended signal from the amplifier was then passed through a RC filter that has a time constant of 1 ms. The filtered signal was digitalized using a 16 bit accurate AD converter ADS8332IBRGET from Texas Instruments Inc. This AD convertor was chosen because of its small packaging, but it limited the resolution of each sensor to 2 Pa. Even though 2 Pa is considerably low, especially while detecting weak stimuli or moving at low Reynolds numbers (Re), this was not a major issue for the purpose of the presented research. Digital readings from the AD converter were sent over serial peripheral interface to the micro controller AT32UC3B1128-AUT from Atmel. Within the micro controller, data was oversampled

50 times and forwarded to the computer using a RS-232 with a 200 Hz sample rate.

Before experiments, the sensors were tested for variation in depth, temperature and sensitivity to background noise. When the craft was set in motion, sensors showed nonlinear dependence to a rising temperature of the sensors themselves. Temperature-induced drifts were significant in recordings longer than a minute. To minimize the temperature effects, the duration of each experiment was kept short (less than a minute) and long breaks between experiments were given. During post-processing, each motion cycle was analyzed separately and the results were checked for consistency.

2.4. Motion rig and movement

The craft was actuated externally using a motion rig. The movement was one-dimensional along the x direction. The velocity of the craft U is therefore defined as the rate of change in position along the x direction,

$$U = \frac{dx_0}{dt} \tag{1}$$

A linear motor rig (MT480P Aerotech Inc.) was mounted above the flow tank and controlled by Soloist Motion Controller 3.02 (Aerotech Inc.). The position and speed of the craft was logged at 200 Hz. A mounting arm connected the linear motor to the craft behind the pressure array, suspending it in the middle of the working section. A harmonic motion with a forward–backward oscillation at 0.16 Hz was chosen. Peak to peak traveling distance was 0.45 L. The motion began at the center position and then moved forward to begin the oscillation which was repeated three times. Figure 3 illustrates the position, velocity and acceleration graphs of the craft while in motion.

Pressure readings were logged during motion; the initial and the final 2 s of data were excluded from the analysis due to a complex starting and ending motion. Characterization of the motion rig was performed before the actual experiments. The rod holding the craft had a resonant frequency around

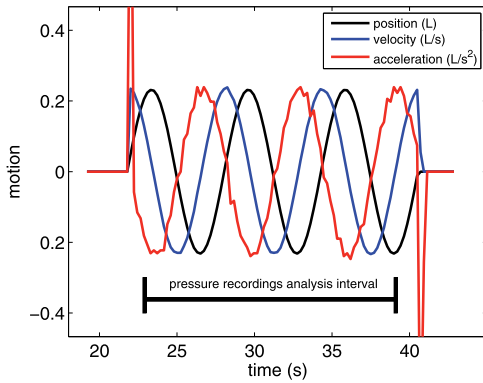


Figure 3. Position, velocity and acceleration profile of harmonic motion. Positive direction corresponds to forward motion.

Table 1. Steady motion swimming range (U) and $Re = \frac{U \cdot L}{\nu}$, defined in terms of the craft's body length (L) and kinematic viscosity (ν).

U ($L s^{-1}$)	0.34	0.54	0.69	0.89	0.96
Re	21 809	34 846	44 091	57 129	61 633

4 Hz whose amplitude was small compared to the desired harmonic motion. Even though flow visualization around the craft showed no indication of subsidiary motion effects, 4 Hz and its harmonics were picked up by the sensors. These frequencies were filtered out using a low pass filter with 3 Hz cut-off frequency.

2.5. Experiments

Two set of experiments were performed. In the first set, pressure readings were recorded when the craft was held still against a steady flow, to represent steady forward motion. Table 1 lists the investigated flow speeds.

In the latter experiments, harmonic motion as described in figure 3 was applied in still water and steady flows. The relative speed of the craft with respect to the oncoming flow was varied $\pm 0.2 L s^{-1}$ ($\pm 12800 Re$). In still water, the ratio between the magnitudes of the swimming velocity and acceleration of the craft was 1 : 1 whereas at $U = 1 L s^{-1}$ it was 5 : 1, enabling the analysis of self-generated pressures over varying swimming conditions.

Before each experiment sensor readings were recorded in still water for 20 s. These data were used as a background reference to analyze pressure readings.

2.6. Flow visualization

Flow visualization was used to observe the fluid-craft interaction. It was carried out using a continuous green-light laser (532 nm, Laser Quantum, TSITM), a high speed PCO 1200 hs CCD camera and a synchronizer (TSITM). Polyamide particles, (average diameter 100 μm), were used to seed the flow (Vestosint 1101, Evonik Industries). Images of laser-illuminated particles were captured, through a front-silvered mirror set at 45° below the flow tank using Insight 3G software (TSITM).

3. Theoretical framework

The presented relationship between motion and sensing is valid only for the pressure tapped head and cannot be used to predict the pressure distribution for the rest of the body. Lighthill discussed in [18] that with the assumptions of irrotational flow and no boundary layer effects, the pressure distribution on the surface of the head can be approximated by the Bernoulli equation,

$$P = -\rho \frac{\partial \phi}{\partial t} - \frac{1}{2} \rho |\text{grad} \phi|^2; \tag{2}$$

P represents the pressure difference between the actual distribution of the fluid pressure and purely hydrostatic pressure. ρ is the density of the water, which is taken as a constant, and ϕ is the velocity potential. With the assumption of a two-dimensional potential flow, the velocity potential associated with the head movement in the x direction (all lateral and rotational motions are excluded) is given by

$$\phi = U \phi_x(r, \theta), \tag{3}$$

where (r, θ) is defined with respect to origin (x_0, y_0) (figure 2).

3.1. Steady motion

In steady, forward motion, time derivatives of the velocity potential vanish ($\frac{\partial \phi}{\partial t} \rightarrow 0$) leading to a well-known case,

$$P = -\frac{1}{2} \rho U^2, \tag{4}$$

where the pressure is inversely proportional to the square of velocity magnitude. At the nose (forward most point) of the craft the velocity is assumed to be 0, resulting in the highest pressure point (stagnation point). At the widest part of the head the pressure drops to a minimum due to the accelerated flow.

3.2. Forward acceleration

In case of forward, accelerated motion, equation (3) simplifies to

$$\frac{\partial \phi}{\partial t} = \frac{dU}{dt} \phi_x - U^2 \frac{\partial \phi_x}{\partial x}. \tag{5}$$

Now equation (2) together with equation (5) gives

$$P = -\rho \frac{dU}{dt} \phi_x - \frac{1}{2} \rho U^2 \left(\frac{\partial \phi_x}{\partial x} \frac{\partial \phi_x}{\partial x} + \frac{\partial \phi_x}{\partial y} \frac{\partial \phi_x}{\partial y} - 2 \frac{\partial \phi_x}{\partial x} \right). \tag{6}$$

Equation (6) can be represented in the form

$$P = C_1 \frac{dU}{dt} + C_2 U^2 + C_3, \tag{7}$$

where

$$C_1 = -\rho \phi_x$$

$$C_2 = -\frac{1}{2} \rho \left(\frac{\partial \phi_x}{\partial x} \frac{\partial \phi_x}{\partial x} + \frac{\partial \phi_x}{\partial y} \frac{\partial \phi_x}{\partial y} - 2 \frac{\partial \phi_x}{\partial x} \right). \tag{8}$$

The first term is an inertial term related to the acceleration of the craft and the second term is related to the square of

its swimming velocity. The coefficients of C_1 and C_2 depend on the geometry of the craft. The term C_3 is incorporated in the model to account for any other relations which we were unaware of. It is difficult to derive these coefficients theoretically; we therefore follow a data-driven approach which builds and validates the model using experimental measurements.

3.3. NARMAX system identification

The relations given in equation (7) were identified using NARMAX system identification [19], which produces the most parsimonious model to capture the relationship between self-motion and pressure sensing based on the experimental data (input–output measurements). NARMAX system identification is a well-established parameter estimation toolkit which has been used in many disciplines [20, 21]. A NARMAX model can be in various forms such as polynomials, multi-resolution wavelets [22], Bernstein coefficients and radial basis function expansions [23]. A polynomial expression was the most appropriate to represent the equation (7).

For a multiple input, single output noiseless system the model terms are constructed based on all the linear and nonlinear combinations of

$$y(n) = f(u_1(n), \dots, u_d(n), \dots, u_d^l(n - N_u), y(n - 1), \dots, y^l(n - N_y)) + C_0,$$

where $u(n)$ and $y(n)$ are sampled input and output signals at discrete time n , N_u and N_y are the regression orders (maximum number of time lags) of the input and output, d is the dimension of the input vector and l is the degree of the polynomial. C_0 is a constant number. The modeling parameters N_u , N_y , d and l are chosen manually depending on the nature of the system under investigation.

Coefficients of the model terms are estimated using an orthogonal parameter estimation (OPE) algorithm [24]. First an auxiliary model is defined such that the terms in the model are orthogonal over the training data set. The coefficient of each term in the auxiliary model is then estimated in the least-squares manner. The individual contribution of each term to the desired output variance is measured using an error reduction ratio. The terms with contributions less than a determined threshold are removed from the model and the coefficients of the remaining terms are re-computed. This is an iterative process until the model passes the model validity test [25]. Finally, the coefficients of the NARMAX model are calculated from the resultant auxiliary model.

One decisive advantage of OPE compared to classical least-squares parameter estimation methods is that OPE provides an indication to the significance of model terms allowing the removal of insignificant ones, which yields to more parsimonious models. In this way, the real structure of the system can be detected.

During modeling, sensor p_5 on the tip of the craft (highest pressure point) was used as a reference to the ground the other pressure sensors ($p_5 - p_i$, where $i = (1, \dots, 9)$). The data recorded from experiments were divided into two parts: (i) training data and (ii) validation data. The training data

Table 2. NARMAX model which relates the pressure difference between nose and lateral sensors to the flow speed.

$$p_{5-1} = 0.05U^2 + 0.80U + 1.86, \quad (R^2 = 0.90, \text{ MAE} = \%4 \pm 2 \text{ Pa})$$

$$p_{5-9} = 0.05U^2 + 0.78U + 1.35, \quad (R^2 = 0.96, \text{ MAE} = \%3 \pm 1 \text{ Pa})$$

was used to estimate the parameters of the model and the validation data was used to evaluate the obtained models. Statistical measures—coefficient of determination (R^2) and mean absolute error (MAE) between real and predicted pressure—were computed to measure the performance.

4. Results

4.1. Experiment 1. Craft fixed in steady flow

We first analyzed pressure distribution (p_1, \dots, p_9 , mean \pm standard deviation) when the craft was held still facing toward the incoming flow. The flow speed was equivalent to the forward velocity of the craft. The pressure measurements were averaged over a 20 s window. The measurements in still water were taken as a reference (0 Pa).

Figure 4(a) shows that the absolute pressures increased with the flow speed. The foremost sensor (p_5) always measured the highest pressure (stagnation point). The pressure decreased gradually toward the sides. The pressure profile was symmetric across the head; sensors on the right and left sides had similar values. The lowest pressure was detected by the most lateral sensors (p_1 and p_9). At two extreme flow speeds ($U = 0.34 \text{ L s}^{-1}$ and $U = 0.96 \text{ L s}^{-1}$), $p_5 = 97.6 \pm 6.1 \text{ Pa}$ and $305.7 \pm 8.5 \text{ Pa}$, $p_1 = 88.0 \pm 5.3 \text{ Pa}$ and $222.0 \pm 5.7 \text{ Pa}$ and $p_9 = 86.3 \pm 6.3 \text{ Pa}$ and $227.1 \pm 5.5 \text{ Pa}$.

Figure 4(b) shows the pressure gradient (pressure difference across sensors). The highest pressure difference was detected around the tip of the craft by $p_5 - p_4$ ($3.0 \pm 1.1 \text{ Pa}$ at $U = 0.34 \text{ L s}^{-1}$ and $43.9 \pm 6.0 \text{ Pa}$ at $U = 0.96 \text{ L s}^{-1}$) and $p_5 - p_6$ ($2.1 \pm 0.7 \text{ Pa}$ and $42.5 \pm 6.4 \text{ Pa}$). The minimum pressure difference was detected by $p_3 - p_2$ ($1.0 \pm 0.5 \text{ Pa}$ and $6.3 \pm 0.7 \text{ Pa}$) and $p_7 - p_8$ ($1.0 \pm 0.4 \text{ Pa}$ and $9.1 \pm 0.6 \text{ Pa}$). The minimum pressure points were at $\theta = \pm \frac{\pi}{3}$.

Figure 4(c) presents how the pressure distribution was changed with respect to the stagnation point (sensor p_5). The relationship between $p_5 - p_1$, $p_5 - p_9$ and flow velocity was identified through NARMAX modeling (table 2). The pressure difference was proportional to the square of the flow speed. Figure 4(d) shows the experimentally measured and model predicted data points that matched closely ($R^2 > 0.90$, $\text{MAE} < \%5$).

4.2. Experiment 2. Moving the craft forward and backward

We next analyzed the pressure measurements when the craft was exposed to the harmonic forward–backward motion (at 0.16 Hz), where the velocity and acceleration of the craft changed sinusoidally with 90° phase difference.

Figure 5 shows the effect of motion on the pressure measurements when the craft was moving in still water. The pressure readings oscillated around 0 Pa with the frequency of

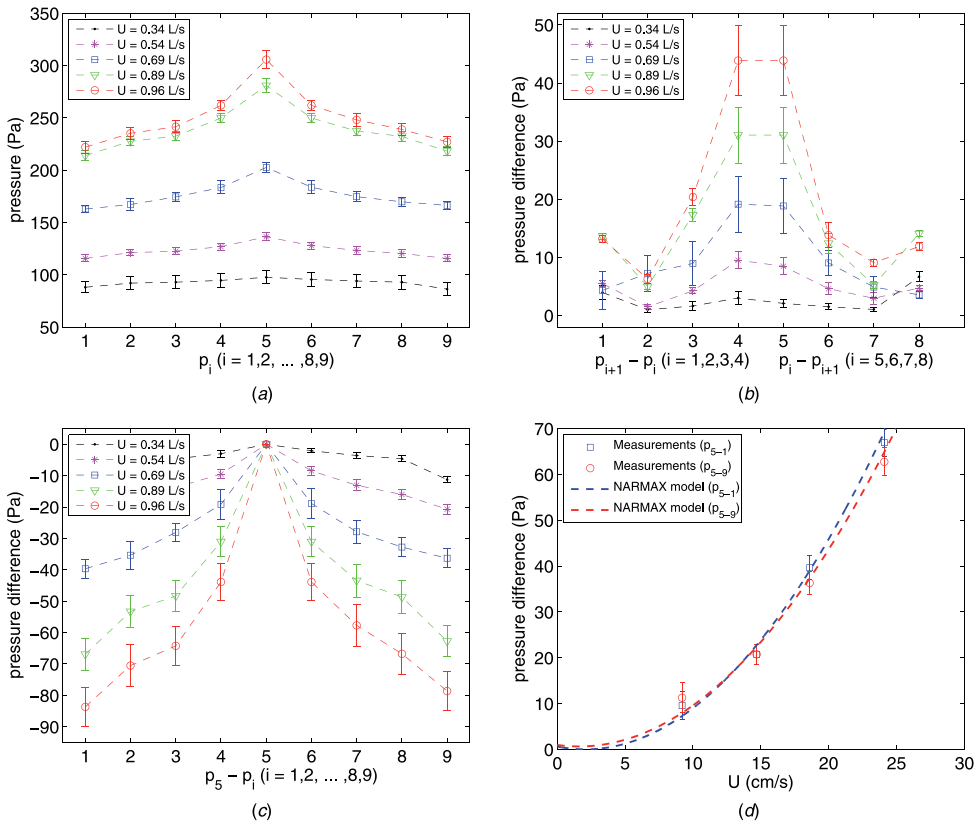


Figure 4. Five flow velocities (listed in table 2) were tested against the rigidly held craft. (a) Mean pressure recordings. (b) Mean pressure gradient. (c) Mean pressure referenced to the sensor on the nose p_5 . (d) Mean pressure difference between nose and lateral sensors versus flow speed. Second degree polynomial fits are presented in table 3.

the harmonic motion (figure 5(b)). The foremost sensors p_4 , p_5 and p_6 measured higher pressure values than the sensors on the sides. The maximum peak to peak pressure was detected by the sensor p_5 (± 10 Pa) and the minimum peak to peak pressure was detected by the most lateral sensors p_1 and p_9 (± 2 Pa). We observed high correlation between the pressure readings and the acceleration of the craft; the extremum points of pressure signals matched the ones of acceleration vertically along the time axis.

Figure 5(c) shows the pressure readings referenced to the sensor p_5 . The maximum pressure difference was detected by the most apart sensors $p_5 - p_1$ and $p_5 - p_9$. Both values were around ± 6 Pa.

Figure 5(d) shows the local pressure difference across the sensors. They were also correlated with the acceleration of the craft. Their oscillation amplitude was less than ± 2 Pa⁵. There was no significant pressure difference across the head of the craft (figure 5(e)).

Figure 6 shows the sensor recordings when the craft was moving in steady flow ($U = 0.7$ L s⁻¹). Compared to the

⁵ In this particular experiment, the resolution of sensors was not high enough to investigate the pressure gradient as a function of the location of sensors.

motion in still water, the acceleration of the craft remained the same, but its relative velocity with respect to the incoming flow increased from $[-0.2, 0.2]$ L s⁻¹ to $[0.4, 0.8]$ L s⁻¹.

The offset of the absolute pressure detected by the sensor p_5 increased by 250 Pa. It's oscillation amplitude also increased from 19 to 47 Pa (figure 6(b)). The offset of the pressure difference $p_5 - p_1$ increased by 44 Pa and its oscillation amplitude increased from 13 to 38 Pa (figure 6(c)). The pressure gradient on the front part of the craft was significantly larger than the pressure gradient on the sides (figure 6(d)). The oscillation amplitudes of $p_5 - p_4$ and $p_2 - p_1$ were 31 and 8 Pa, respectively. The pressure readings were more sensitive to the craft's velocity than to its acceleration. Again, no pressure difference across the head was detected (figure 6(e)).

4.3. Flow visualization around the craft

Flow visualization was used during the motion of the pressure head to highlight the surrounding fluid motion. The craft was illuminated by the laser sheet from one side, so the shadow cast behind the object remains black. Figure 7(a-c)

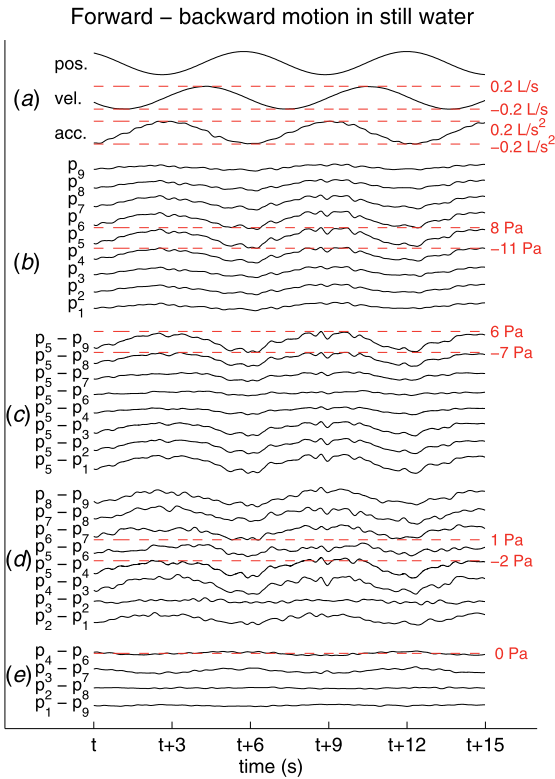


Figure 5. Pressure recordings when craft was moving in still water. (a)—Craft’s motion data, (b)—absolute pressure recordings from each sensor, (c)—pressure recordings referenced to p_5 , (d)—pressure gradient, e —pressure difference across the head. The numbers on the right shows the range of maximum peak to peak signal in each class.

shows the movement of the fluid caused solely by the motion of the craft in still water. The fluid was pushed forward and sideways when the craft was accelerating forward (figure 7(a)). The entrained fluid along the body continued to move forward once the craft was reversing the motion path (figure 7(b)), visualized as a region of decelerated flow largest just after the widest section of the craft. The flow direction was then reversed as surrounding fluid was sucked in behind the nose and from the sides as the craft moved backward (figure 7(c)).

When moving in a steady flow ($U = 0.7 \text{ L s}^{-1}$), the relative velocity of the craft changed compared with that of its environment. However the fluid overcame any effects from the movement of the craft that were seen in still water. Figure 7(d) shows the streakline patterns suggesting very little fluid separation over the accelerating body that can be seen at this resolution. Flow visualization and pressure recordings were in agreement that inertial effects of the craft were more tangible at low swimming velocities ($U < 0.2 \text{ L s}^{-1}$). These effects diminished to a great extent at higher swimming velocities ($U > 0.7 \text{ L s}^{-1}$).

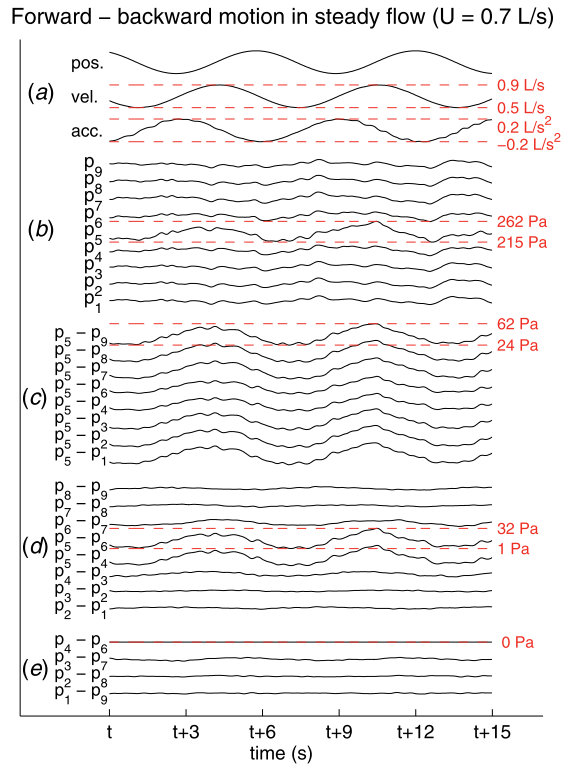


Figure 6. Pressure recordings when the craft was moving in steady flow ($U = 0.7 \text{ L s}^{-1}$). (a) Craft’s motion data, (b) absolute pressure recordings from each sensor, (c) pressure recordings referenced to p_5 , (d) pressure gradient, (e) pressure difference across the head. The numbers on the right show the range of maximum peak to peak signal in each class.

Table 3. The NARMAX model which estimates the pressure distribution around the craft based on its motion. The units of U , $\frac{\partial U}{\partial t}$ and r are represented in terms of L . The unit of θ is in radian.

$$p_5 - p_i = (20.4 \sin(|\theta_i|) + 4.7) \frac{\partial U}{\partial t} + 68.9U^2 + (21.1 \sin(|\theta_i|) - 18.0)U + 2.7 \sin(|\theta_i|) - 1.6 \quad (9)$$

5. Mapping motion to pressure sensing

Next, the relationship between the motion and pressure distribution over the craft was identified. Motion parameters (position, velocity and acceleration) and position of each sensor $i (r_i, \sin(\theta_i))$ were fed into the NARMAX method to model pressure readings in terms of $p_5 - p_i$. Due to lateral symmetry across the head, $|\theta_i|$ was used instead of θ_i . The training and validation data sets were formed from all the data recorded at different flow speeds when the craft was in motion. The resultant model is a second-order polynomial (table 3). Figure 8 shows the experimental and model predicted pressure, which match closely ($R^2 = 0.84$ and $\text{MAE} = 7.71 \pm 0.03 \text{ Pa}$).

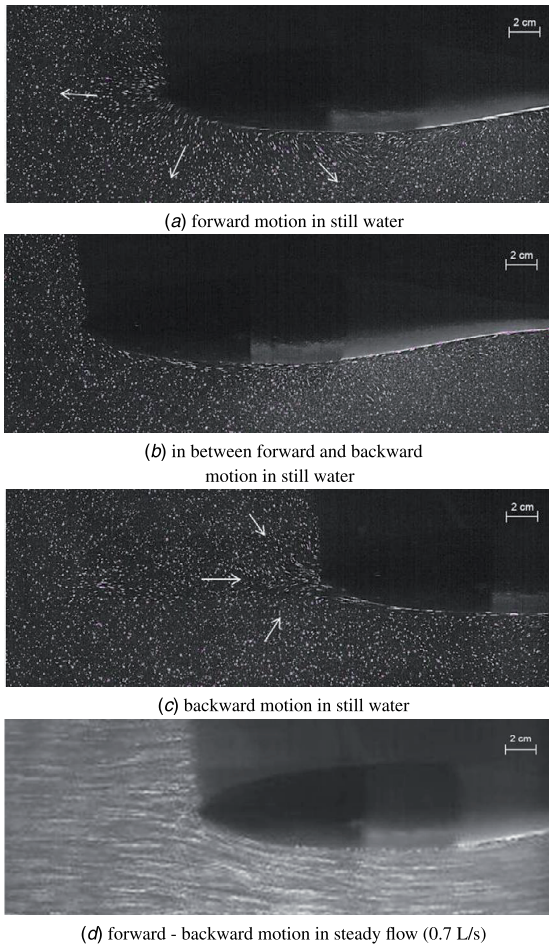


Figure 7. Flow visualization of the craft moving forward and backward in still water (a)–(c) and in steady flow (d). (a) Forward motion in still water, (b) in between forward and backward motion in still water, (c) backward motion in still water, (d) forward–backward motion in steady flow (0.7 L s⁻¹).

Table 4. Sensitivity of the NARMAX model of table 4 to the velocity, acceleration and position of the sensors.

$\frac{\partial(p_s - p_i)}{\partial U}$	$= 137.8U + (21.1 \sin(\theta_i) - 18.0$
$\frac{\partial(p_s - p_i)}{\partial \frac{dU}{dt}}$	$= 15.4 \sin(\theta_i) + 4.7$
$\frac{\partial(p_s - p_i)}{\partial \theta_i}$	$= 20.4 \cos(\theta_i) \frac{dU}{dt} + 21.1 \cos(\theta_i)U + 2.7 \cos(\theta_i)$

5.1. Sensitivity of the NARMAX model to the craft’s velocity, acceleration and sensor position

The model’s partial derivatives with respect to the craft’s velocity, acceleration and sensor position were analyzed to measure the model’s sensitivity to these variables (table 4).

We defined sensitivity as the change in pressure as a function of the change in U , $\frac{dU}{dt}$, θ_i ; the higher the pressure

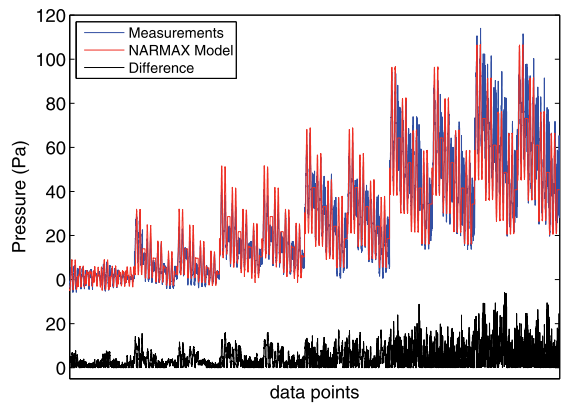


Figure 8. The real pressure measurements (blue) are overlaid with the predictions generated by the NARMAX model detailed in table 4 (red). The difference between the two is plotted in black.

change, the more sensitive the model is. For a given sensor where $\sin(|\theta_i|)$ is known, the sensitivity coefficient of velocity ($\frac{\partial(p_s - p_i)}{\partial U}$) increases proportionally with increasing velocity, whereas the coefficient of acceleration ($\frac{\partial(p_s - p_i)}{\partial \frac{dU}{dt}}$) remains constant. Figure 9(a) shows the behavior of these coefficients as a function of swimming velocity for $p_s - p_i$. When $U < 0.2 \text{ L s}^{-1}$, the model is more sensitive to the craft’s acceleration ($\frac{\partial(p_s - p_i)}{\partial \frac{dU}{dt}} > \frac{\partial(p_s - p_i)}{\partial U}$). This relationship changes in favor of velocity at higher swimming velocities. When $U = 1 \text{ L s}^{-1}$, the model is almost five times more sensitive to the velocity than the acceleration.

Figure 9(b) shows the model’s sensitivity to the position of the sensors when $\frac{dU}{dt} = 0.1 \text{ L s}^{-12}$. The sensitivity decrease as the angle θ_i increases indicates that the sensors on the sides are less sensitive to the forward motion than the sensors on the front. The slope of the curves gets steeper at higher swimming velocities suggesting that the difference between the sensitivity of the front and side sensors increases.

6. Discussion

The navigation of complex aquatic environments requires an increased sensitivity to external signals, which can come from static objects, moving objects or hydrodynamic features in the flow such as eddies and vortices. In real life scenarios detection of peripheral stimuli is challenged by the self-motion of the craft.

The purpose of this study is to analyze the self-motion effects on the surface pressure of the fish-shape craft. The investigated motion, an harmonic forward–backward movement in still and in flowing water, was unexplored before, and it provided a rich repertoire of unsteady, accelerated/decelerated motions at different swimming speeds. A second-order polynomial (table 3) obtained via the NARMAX process shows that the pressure distribution across the head can be anticipated successfully using the velocity and acceleration of the craft. Within the swimming range up to 1 L s^{-1} , the model predictions closely matched the

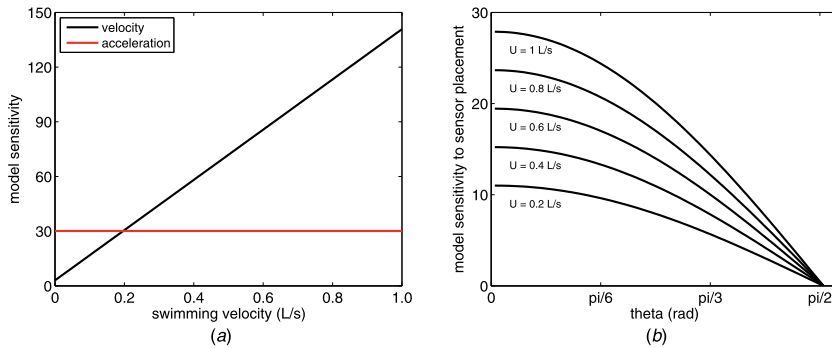


Figure 9. (a) The NARMAX model sensitivity to both velocity (black) and acceleration (red) are plotted across the swimming range. The profiles are computed based on the equations given in table 5. Acceleration dominates the signal response below 0.2 L s^{-1} . (b) The NARMAX model sensitivity to sensor position. The front sensors (small θ) are more sensitive to the self-motion than the sensors on the side.

experimental data with an error margin of 20% and an average error less than 10%.

6.1. Effects of swimming speed

The analysis of both the experimental data and the NARMAX model revealed that the pressure increased quadratically with increasing swimming velocities. When $U < 0.2 \text{ L s}^{-1}$ the sensors were more sensitive to the craft's inertia than its velocity. The pressure profiles matched closely the acceleration profile of the craft. On the other hand, the inertial effects decreased proportionally at higher swimming velocities; the pressure signals were correlated with the velocity of the craft rather than its inertia. These results suggest that moving at a low, constant velocity is preferential as a sensing strategy to focus on external stimuli.

Our results also have direct relevance to biology, in particular lateral line sensing. When fish forage or watch out for predators, their tendency to swim quietly using burst and coast swimming can be interpreted as an effort to minimize self-motion effects and increase the sensitivity of lateral line to external stimuli. While swimming at higher velocities, the self-generated pressures increase to high levels, which can easily mask the hydrodynamic stimuli. For instance, when the craft is moved at 1 L s^{-1} the pressure detected by the foremost sensors reach values up to 300 Pa. This value is at least an order of magnitude higher than the vortex-induced pressure detected in Kármán vortex streets [11]. We speculate that at higher swimming velocities fish may rely on other sensor modalities more to monitor the environment. In the mean time, the information sensed by the lateral line can be used for supervising swimming such as rheotaxis behavior [26].

The self-motion effects are minimized in the domain of pressure gradient, local pressure differences among sensors. The pressure difference between $p_5 - p_4$ was at least an order of magnitude smaller than the individual pressure readings p_5 and p_4 . It is assumed that the canal neuromasts in fishes are sensitive to the pressure difference across the canal pores, which is similar to the pressure gradient measured in this study.

Table 5. Reverse NARMAX model which maps pressure readings to the craft's velocity.

$$U = 0.01(p_5 - p_1) - 0.09(p_5 - p_3) + 0.04(p_5 - p_6) + 0.03(p_5 - p_8) + 0.03(p_5 - p_9) - 0.06 \quad (10)$$

Our results suggest that this sensing arrangement can improve the signal-to-noise ratio, especially to detect the information related to external stimuli.

We loosely divide the pressure sensors into two groups in terms of their location: the sensors on the front and the sensors on the sides. The first group is more sensitive to the self-motion and the sensitivity increases at higher swimming velocities. Windsor previously reported that certain fish heading toward the wall could detect the wall at shorter distances with increasing speed [16]. This was contrary to the initial hypothesis of fish swimming at higher speeds would generate a stronger bow wake enabling the fish to detect the wall earlier at longer distances. However, our findings suggest that the self-generated pressures of faster fish can lower the signal-to-noise ratio and prevent early detection of the wall.

6.2. Speedometer via distributed pressure sensing

Finally we used the NARMAX process to obtain a reverse model which links the pressure readings to the velocity of our craft. The resultant model is given in table 5 with $R^2 = 0.92$ and $\text{MAE} = 0.08 \pm 0.001 \text{ L s}^{-1}$. Figure 10 illustrates the measured and predicted velocities as well as their difference. Predictably the linear model did not perform well when $U < 0.2 \text{ L s}^{-1}$, as in this swimming range the pressure readings were more sensitive to the craft's acceleration. Higher order polynomials, including time lagged pressure readings, can address this problem straight away.

We conclude that distributed pressure sensing can be used as a speedometer to estimate the relative velocity of the craft. Sensor feedback on swimming velocity can be used to stabilize the cruising speed or to estimate the traveling distance like an odometer. Overall, our results emphasize that distributed pressure sensing can be used to evaluate the motion of the craft as well as to predict the hydrodynamic conditions around

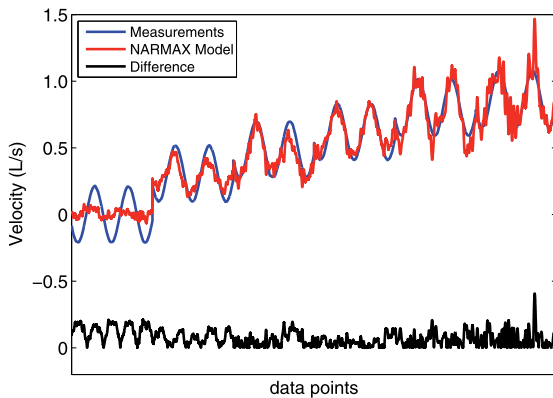


Figure 10. Performance of the reverse NARMAX model of table 5 to estimate the craft's velocity.

the craft, enabling us to develop more efficient navigation strategies.

Acknowledgments

This work is carried out under the FILOSE project, supported by the European Union, seventh framework programme (FP7-ICT-2007-3). We thank Dr James C Liao and Dr Steve A Billings for their guidance and constructive criticism on the presented work.

References

- [1] Bleckmann H 1994 Reception of Hydrodynamic Stimuli in Aquatic and Semiaquatic Animals (*Progress in Zoology* vol 41) ed W Rathmayer (Stuttgart: Gustav Fisher Verlag) pp 1–115
- [2] Coombs S and Smart s 2001 Information processing by lateral line flow sensors *Auton. Robots* **11** 225–61
- [3] Bodznick D, Montgomery J C and Bradley D J 1992 Suppression of common mode signals within the electrosensory system of the little skate *Raja erinacea* *J. Exp. Biol.* **171** 107–25
- [4] Montgomery J C and Bodznick D 1994 An adaptive filter that cancels self-induced noise in the electrosensory and lateral line mechanosensory systems of fish *Neurosci. Lett.* **174** 145–8
- [5] Cowan N J and Fortune E S 2007 The critical role of locomotion mechanics in decoding sensory systems *J. Neurosci.* **27** 1123–8
- [6] Feitl K E, Ngo V and McHenry M 2010 Are fish less responsive to a flow stimulus when swimming? *J. Exp. Biol.* **213** 3131–7
- [7] Yang Y, Nguyen N, Chen N, Lockwood M, Tucker C, Hu H, Bleckmann H, Liu C and Jones D L 2010 Artificial lateral line with biomimetic neuromasts to emulate fish sensing *Bioinspir Biomim.* **5** 016001
- [8] Bouffanais R, Weymouth G D and Yue D K P 2011 Hydrodynamic object recognition using pressure sensing *Proc. R. Soc. A* **467** 19–38
- [9] Fernandez V I and Triantafyllou M S 2011 Performance analysis for lateral-line-inspired sensor arrays *PhD Thesis* Massachusetts Institute of Technology and the Woods Hole Oceanographic Institution
- [10] Klein A and Bleckmann H 2011 Determination of object position, vortex shedding frequency and flow velocity using artificial lateral line canals *Beilstein J. Nanotechnol.* **2** 276–83
- [11] Venturelli R, Akanyeti O, Visentin F, Jezov J, Chambers L D, Toming G, Brown J, Kruusmaa M, Megill W M and Fiorini P 2012 Hydrodynamic pressure sensing with an artificial lateral line in steady and unsteady flows *Bioinspir Biomim.* **7** 036004
- [12] Dubois A, Cavagna G A and Fox R S 1974 Pressure distribution on the body surface of swimming fish *J. Exp. Biol.* **60** 581–91
- [13] Zingg D W 1989 Low mach number Euler computations *NASA TM* 102205
- [14] McAlister K W and Takahashi R K 1991 NACA 0015 wing pressure and trailing vortex measurements, *NASA TP* 3151
- [15] Hassan E S 1992 Mathematical-description of the stimuli to the lateral line system of fish derived from a 3-dimensional flow field analysis: I. The cases of moving in open water and of gliding towards a plane surface *Biol. Cybern.* **66** 443–52
- [16] Windsor S P, Norris S E, Cameron S M, Gordon D M and Montgomery J C 2010 The flow fields involved in hydrodynamic imaging by blind Mexican cave fish (*Astyanax fasciatus*): part 1. Open water and heading towards a wall *J. Exp. Biol.* **213** 3819–31
- [17] Ragni D, Ashok A, van Oudheusden B W and Scarano F 2009 Surface pressure and aerodynamic loads determination of a transonic airfoil based on particle image velocimetry *Meas. Sci. Technol.* **20** 074005
- [18] Lighthill J 1993 Estimates of pressure difference across the head of a swimming clupeid fish *Phil. Trans. R. Soc. B* **341** 129–40
- [19] Chen S and Billings S A 1989 Representations of non-linear systems: the NARMAX model *Int. J. Control* **49** 1013–32
- [20] Billings S A and Chen S 1998 The determination of multivariable nonlinear models for dynamical systems *In Neural Network Systems, Techniques and Applications* ed C Leonidas (New York: Academic) pp 231–78
- [21] Akanyeti O 2009 Automatic code generation for autonomous mobile robots *PhD Thesis* University of Essex
- [22] Coca D and A Billings S 2001 Non-linear system identification using wavelet multiresolution models *Int. J. Control* **74** 1718–36
- [23] Chen S and Billings S A 1992 Neural networks for nonlinear dynamic system modelling and identification *Int. J. Control* **56** 319–46
- [24] Korenberg M, Billings S A, Liu Y P and McIlroy P J 1988 Orthogonal parameter estimation algorithm for non-linear stochastic systems *Int. J. Control* **48** 193–210
- [25] Billings S A and Voon W S F 1986 Correlation based model validity tests for non-linear models *Int. J. Control* **44** 235–44
- [26] Montgomery J C, Baker C F and Carton A G 1997 The lateral line can mediate rheotaxis in fish *Nature* **389** 960–3

Appendix C

J. Ježov, O. Akanyeti, L. D. Chambers, and M. Kruusmaa, “Sensing oscillations in unsteady flow for better robotic swimming efficiency,” in *2012 IEEE International Conference on Systems, Man, and Cybernetics*, 2012, pp. 91–6.

Sensing oscillations in unsteady flow for better robotic swimming efficiency

Jaas Ježov, Otar Akanyeti, Lily D. Chambers, Maarja Kruusmaa

Abstract—Turbulent flows are often treated as a noisy environment by control algorithms of underwater robots. However, aquatic animals such as fish have learned to take advantage of certain unsteady flow. Periodic complex flow, such as that found in the wake of cylinders has been shown to offer energy saving opportunities to fish. We built a fish-like robot with an integrated pressure sensor array housed in the head. The robot can control its tail beat synchronization with respect to the periodic oscillations in the flow behind a cylinder. We show that vortices, represented here by pressure maxima, can be detected and exploited to increase the swimming efficiency of the robot fish while it remains rigidly mounted to a force plate. Force measurements show an efficiency gain of 23% when the tail beat of the robotic fish is synchronized at a particular phase lag.

I. INTRODUCTION

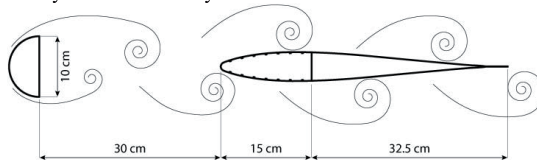
The swimming efficiencies of fish and sea mammals are investigated by many researchers in various disciplines as understanding the principles of their control and locomotion is interesting both for biologists and engineers. Fin locomotion is mostly investigated in steady flows. But as in a real world, flow is seldom steady, it is therefore interesting to investigate how fish negotiate turbulence to minimize their energy consumption.

Studies show that fish prefer swimming in predictably oscillating flows [1-4], like the Kármán vortex street generated in the wake of a cylinder at particular flow speeds. In the Kármán vortex street, fish can adapt their tail beat to the vortex shedding frequency and slalom between vortices. The tail beat frequency of fish drops considerably compared to swimming in a steady flow [5], also the muscle activity of fish swimming in periodic turbulence is much lower than it would be suggested by the reduced flow behind a bluff body [6]. This suggests that fish can potentially utilize energy from the flow.

Energy harvesting is an interesting topic for underwater robotics because it permits the design and build of vehicles that can survive longer missions. The energetics of finned propulsion has been previously investigated in periodic turbulence and it was found that the efficiency depends on

the timing of the tail beat.

Gopalkrishnan et al. [7] found that the efficiency of an actuated hydrofoil in a controlled turbulence depends on the phase of the hydrofoil interaction with the vortices shed from behind a cylinder. They showed that there are 3 different interaction modes that leave visually distinctive vortex patterns in the wake of the hydrofoil. The mode of interaction depends on the phase of the foil flapping with respect to the vortex location. Triantafyllou et al. [8] highlights that the most thrust is produced with a destructive vortex merging mode. In this mode a vortex produced by the hydrofoil is merging with a vortex from the cylinder rotating in the opposite direction. These vortices destroy each other producing a pattern of weaker vortices in the wake of the hydrofoil. This mode is less efficient than a vortex pairing mode as it requires more power. In the vortex pairing mode a pattern of mushroom like double vortices is produced. The most inefficient is a constructive vortex merging mode where vortices from the cylinder and the hydrofoil are rotating in the same direction at the time of merging. In the vortex pairing mode hydrofoils and fishlike three-dimensional bodies can be actuated even with efficiency over 100% [7-8]. In their studies the controlled turbulence was achieved by oscillating the cylinder laterally in the flow. The angle of the hydrofoil was changed periodically while the pivot point of the hydrofoil was oscillated laterally. The phase difference was measured between the oscillations of the cylinder and the hydrofoil.



In the above mentioned studies the body interaction with the turbulence was controlled experimentally, which, from robotics applications point of view, is not a realistic precondition. In robotics, the control problem is the reverse, instead of controlling the turbulence, the tail beat of the fin should be controlled to gain better efficiency.

The hydrofoils in those experiments were also moving in a lateral direction, which is similar to the biological fish kinematics in the wake of a cylinder [5]. Fish-like robots are usually not directly controlled in the lateral direction. Since we do not have the control over the hydrodynamic environment and the lateral translation, two questions can be asked when investigating swimming efficiency in the

Jaas Ježov and Maarja Kruusmaa are with the Centre for Biorobotics, Tallinn University of Technology, Tallinn, Estonia. {jaas.jezov, maarja.kruusmaa}@ttu.ee

Otar Akanyeti is with the Department of Computer Science, University of Verona, Verona, Italy. otarakanyeti@yahoo.com

Lily D. Chambers is with the Department of Mechanical Engineering, University of Bath, Bath BA2 7AY, UK.

L.D.Chambers@bath.ac.uk

periodic turbulence generated in the wake of a cylinder:

1. Is it possible to synchronize a fishlike robot with a periodically turbulent flow by sensing and measuring flow features?
2. Does the dependency between the tail beat timing and swimming efficiency still exist when a lateral translation of a fish-like robot is not possible?

To investigate these questions we built a robotic fish that is harnessed rigidly in the flow and can only move its tail. A control algorithm of the robotic fish uses a signal from distributed pressure sensors in the robot's head to identify periodic features in the flow. The hydrodynamic presence of a vortex is sensed here by the presence of a pressure maximum on the most forward reaching sensor. When this signal is sensed, an appropriate delay is applied to allow the tail of the robotic fish to interact with the vortex. We show that by controlling the tail beat phase with respect to a periodic turbulence pressure cue, tail efficiency can be considerably increased without the lateral or angular movement of the robotic fish.

II. MATERIALS AND METHODS

A. The flow tunnel

Experiments for this study were conducted in a flow tank located in the Centre for Biorobotics in the Tallinn University of Technology. A flow tunnel is assembled into the tank with 4 m x 1.3 m x 1.45 m dimensions (Figure 1). The tunnel has a 150 cm x 50 cm x 50 cm working section with Plexiglas for the side, bottom and top boundaries. A propeller circulates the flow that pass through two collimators before entering the working section. The collimators insure steady flow for speeds up to 50 cm/s. Periodic turbulence is created in the flow tunnel with a D-shape cylinder that has the flat surface facing downstream. The cylinder has a 10 cm diameter and a length of 48 cm and it is positioned 30 cm downstream from the collimators in the centre of the working section. The robotic fish is fastened to a force gauge so that it is facing upstream. The distance between the flat surface of the cylinder and the nose of the fish is 30 cm.

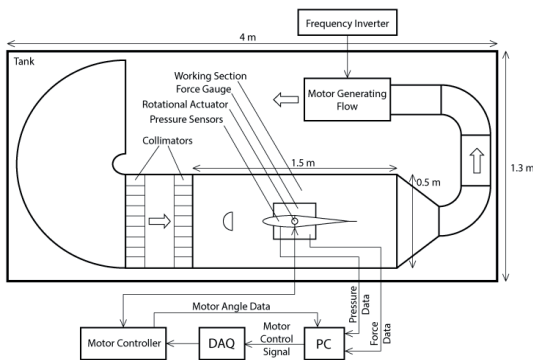


Figure 1. Schematic of the experimental setup.

B. The force gauge

The force gauge was custom made for underwater measurements. It can measure the drag/thrust, the lateral force and the torque around the vertical axis. The force gauge is calibrated with a force gauge LG-5000A developed by Lutron Electronic Enterprise CO., LTD. The custom made force gauge is used with a DC motor that can actuate around the vertical axis. The DC motor is controlled with a PID controller with a position feedback from a Hall Effect sensor AS5304A developed by Austriamicrosystems AG. In these experiments we used motor angle oscillations of ± 15 degrees.

C. The robotic fish

The robotic fish has a fish-like body with a length of 47.5 cm (Figure 2). The largest cross-section area perpendicular to the flow direction is 34.69 cm². The head of the robotic fish is printed out of polyamide powder while the tail is cast from silicon Dragon Skin (Smooth-On, Inc.). A flexible 0.5 mm thick plastic backbone is cast into the tail. The backbone material extends outside the tail to support the tail fin. It forms the upper and lower edge of the tail fin. The fin membrane between the edges is cast from silicon Elite Double 8 (The Zhermack Group). The shape and stiffness profile of the tail is manufactured according to a bio-inspired approach reported in [10]. The tail is treated as a compliant body and is actuated about a single point. In these experiments, the actuator of the tail is an external DC motor fixed to the force gauge. When the tail moves, the head of the robotic fish is fixed with a support fastened to the base of the motor. The gap between the head and the tail is removed by extending the silicon skin from the tail to the edge of the head.

D. Flow sensing

The fish robot senses flow with an artificial lateral line consisting of an array of pressure sensors in the head. The pressure sensing array is connected to the surface of the robot fish head by 14 holes with 2 mm diameter. These holes are positioned on the horizontal plane crossing the tip of the nose. There are 7 holes on either side with 2 cm displacement. The first holes are 2 cm away from the nose tip, measured along the surface of the head.

Each hole leads to a watertight compartment for the MS5407-AM pressure sensors (Measurement Specialties TM) and for data acquisition electronics [9]. In the current study we use only the two pressure sensors closest to the nose. We label the sensor on the left side p1 and the sensor on the right side p2. The signals from the pressure sensors are sampled 50 times per second with an accuracy of 0.1 Pa for the least significant bit.

Digital signals from the pressure sensors, the force gauge and the motor position sensor are transferred to a PC over a RS-232 serial connection. In the PC the signals are processed with a program written in LabVIEW (National Instruments). The same program transmits an analog control signal through a data acquisition card PCIe-6363 (National

Instruments) to a motor controller that drives the motor of the tail.

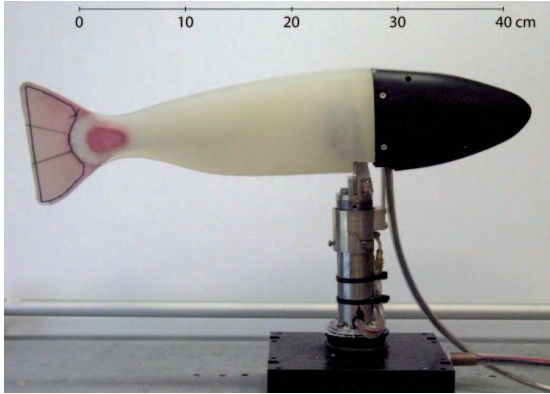


Figure 2. The robotic fish with a compliant tail attached to the force gauge.

To record the experiments we use an overhead camera UI5240HE-M developed by IDS Imaging Development Systems GMBH. For the flow visualization, a laser with a cylindrical lens is used to illuminate particles added to the flow.

E. A periodically turbulent flow

Placing a bluff body into a steady flow will not only slow down the flow because of the shadowing effect but vortices will appear at a certain Reynolds number range. The effect is easiest to understand when the bluff body in the flow has a simple geometrical shape like a cylinder. Shear stress between the low speed flow behind the cylinder and the high speed flow around it encourage vortices to form. First, two stable vortices will form behind the cylinder. This condition will remain stable with low Reynolds number flows; at higher Reynolds numbers, vortices are shed from the cylinder as they grow out of the shadow region of the cylinder.

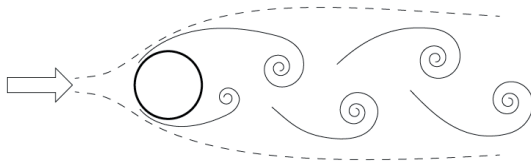


Figure 3. Schematic of the circulation within a Kármán vortex street generated behind a cylinder in flow.

There are always asymmetric events in the flow so that the vortices are never carried away in pairs. Instead a periodical vortex shedding can be observed when vortices are shed intermittently from either side of the cylinder. An illustration of the vortex shedding can be seen in Figure 3. As these vortices travel downstream, they form a pattern of two rows of vortices. This pattern is known as von Kármán vortex street (KVS). In Figure 4 is a streakline capture of a Kármán vortex street created in our test tank for our experiments. In these experiments, the vortex street is not controlled but is measured and characterized beforehand.

The experiments are carried out with a free stream flow speed of 30 cm/s. In the vortex street created with a 10 cm D-shape cylinder the vortex shedding frequency of 0.65 Hz was measured from the pressure data using Fast Fourier Transform. The average wake wavelength of 40 cm and the vortex traveling speed of 26 cm/s was measured from flow visualization captures.

Introducing a fusiform body (such as our robotic fish) in the middle of the vortex street will disturb the flow. Vortices at the side of the robotic fish could get weaker or even be destroyed. However, some regions of vorticity that travel downstream with the vortex shedding periodicity, always remain.

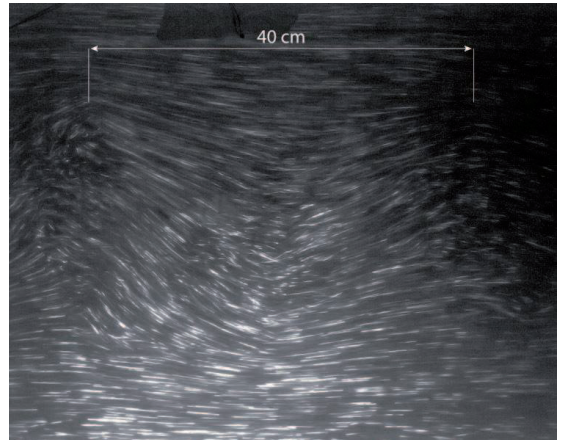


Figure 4. A flow visualization of illuminated particle trajectories within the recirculating wake, with the vortex wake wavelength highlighted, behind a D-shaped cylinder. The left edge of the field of view is approximately 25 cm downstream from the flat side of the D-shape cylinder.

F. Pressure sensing with a fusiform agent

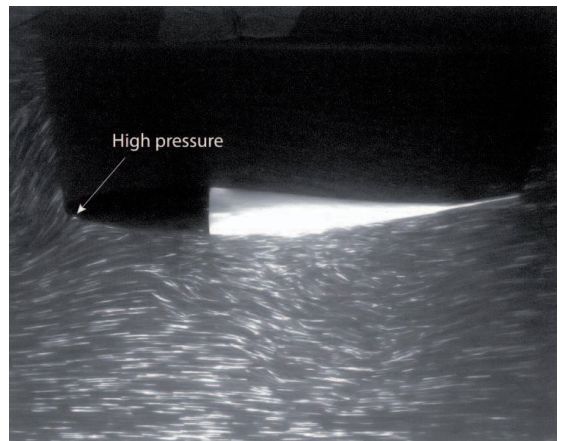


Figure 5. A flow visualization of the robotic fish within a Kármán vortex street. The left edge of the field of view is approximately 25 cm downstream from the flat side of the D-shape cylinder.

It has been experimentally shown that pressure sensors can sense the periodicity of a vortex street [9]. We assume that the pressure sensors sense a relatively higher pressure in

front of the turbulent flow feature, such as a vortex, and a lower pressure behind it. In Figure 5 is a streakline capture of the vortex street with the robotic fish. In the picture the flow is hitting the nose at an angle that makes the stagnation point appear at the location marked by an arrow. This is the high pressure condition preceding the vortex. As the location marked by the arrow is also the location of the pressure sensor, the pressure data synchronized with camera footage shows that there is a pressure maximum at the moment this frame was captured.

Figure 6 illustrates our observations as the oncoming wake interacts with the robotic fish. Arrows in the diagram indicate the flow direction and grey circles represent vortices or areas of vorticity that have survived the collision with the body of the robot fish. On the surface of the robotic fish there is a high pressure at the locations where the arrows are pointing towards the body and low pressure at the locations where arrows are pointing away from the body.

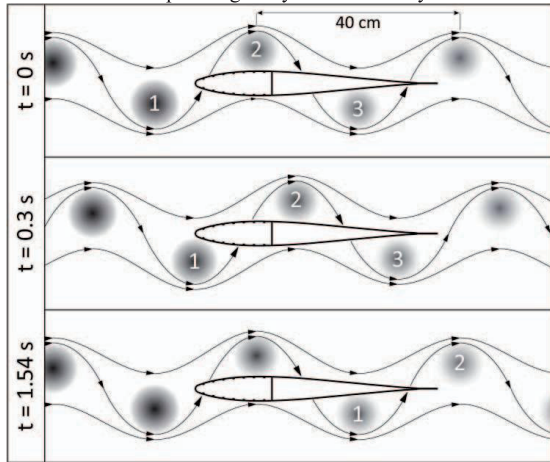


Figure 6. The vortex street with the robotic fish. ($t = 0$ s) A moment when the first pressure sensor on the left side senses the vortex marked by number 1; ($t = 0.3$ s) a moment when the control algorithm detected the maximum that was produced by vortex 1; ($t = 1.54$ s) one period (of vortex street) later from $t = 0$ s, vortex 1 is applying force on the tail fin of the robotic fish.

We propose that in order to achieve the maximum thrust the robotic fish should synchronize its tail beat so as to take advantage of the high pressure regions when the tail pushes away from them. In this case the pressure difference on both sides of the tail helps to push the tail in the forward direction.

In Figure 6 ($t = 0$ s), vortex number 3 is pressing on the tail and at the same time vortex 1 is creating high pressure on the left side of the head at the location of the sensor p1. This is further highlighted in Figure 5 where the tail is slightly bent upwards due to the hydrodynamic forces created by the pressure differences. According to this theory the control algorithm should move the tail with a delay of approximately one period from the moment when the pressure sensor at the head senses the pressure maximum. The movement should be towards the same side of the robotic fish as where the maximum pressure was first

detected.

G. Control algorithm

1) Detection of the vortex street

It is possible to measure the vortex shedding frequency from the pressure sensor signal on runtime but we did not use it as the Fast Fourier Transform would need at least a 5 s time window to give sufficiently accurate results [9]. Instead we decided to find extremums from the pressure signal. For that purpose our fish control algorithm first subtracts the signals of the sensors p1 and p2. These sensors measure the pressure changes caused by the vortex street in an opposite phase and the subtraction helps to raise the signal to noise ratio without losing any useful information [9].

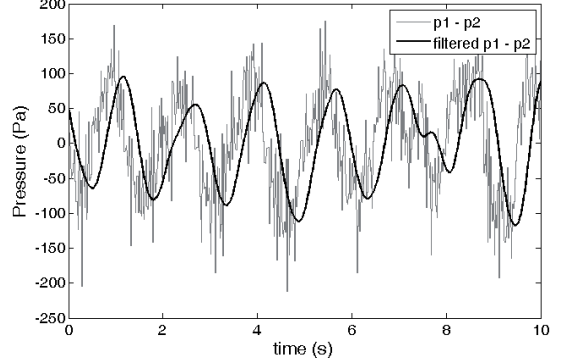


Figure 7. A pressure signal difference between the sensors closest to the nose and the corresponding filtered signal. The signal $p1 - p2$ is grounded to zero by subtracting the mean value of the signal. The filtered signal is delayed by 0.28 s because of the phase shift the filter introduces.

The result is filtered with a low-pass Infinite Impulse Response 3rd order filter with a 0.75 Hz pass band. The filter introduces a 280 ms delay into the signal. The extremums were found with the 2nd order central difference equation by looking for 2 sequential derivatives with a different sign. We were interested in the large scale vortices only so some of the false positives were filtered with an amplitude constraint. A typical pressure signal along with the filtered signal is shown in Figure 7.

2) Phase shift

By the time our algorithm has found an extremum 300 ms has already passed from the time the pressure sensor actually sensed this condition (Figure 6. $t = 0.3$ s). So considering the theory previously proposed in section F. *Pressure sensing with a fusiform agent* we should use a delay $d = T - 0.3$ s to interact with the vortex for the maximum thrust. In this equation T is the period of the vortex street. The delay d also represents a zero phase shift in this study. An additional delay for the phase shift is calculated as a fraction $phase/180$ from $T/2$, the half-period of the vortex street. Instead of increasing this delay over half of the period for a phase shift bigger than 180 degrees, the direction of the motor movement is modified as explained in the following algorithm:

$$q_1 = \text{floor}\left(\frac{\text{phase}}{180}\right)$$

$$q_2 = \text{floor}\left(\frac{q_1}{2}\right)$$

$$r_2 = q_1 - 2 * q_2$$

$$\text{Motor Direction} = \begin{cases} \text{sign}_{\text{extremum}}, r_2 = 0 \\ -\text{sign}_{\text{extremum}}, r_2 \neq 0 \end{cases}$$

where q is the quotient of the floor function and r is the remainder. A total delay (which is from the time a vortex was detected as the maximum in the pressure signal by the first pressure sensor to the moment when the tail of the robot fish has to interact with it) can be calculated with the following formula:

$$\text{Delay}_{\text{Total}} = d + (T * \text{phase}) \bmod 360$$

where d is the delay for the zero phase, T is the period of the vortex street and phase is the desired phase shift of tail-vortex interaction.

3) Motor control signal

When an extremum is found, $\text{Delay}_{\text{Total}}$ is added to the present time. This timestamp marks the time when the motor controlling the tail should reach its maximum deflection. The timestamp is then added to the First In First Out array.

The motor is controlled with sinusoidal actuation signals that are divided into half-periods. During one cycle, the motor is driven from one extreme position to the opposite which both correspond to the opposite maximum deflections of the tail. When the current half-period of the command signal is finished, a new interaction time for the next half-period is taken from the array of timestamps and a sinusoidal half-period is fitted between the current time and the interaction time. The direction of the motor is read from a similar array which is filled with directions that correspond to the interaction times. This kind of a control insures that we have a continuous control signal even when the phase of the tail movement is changed.

III. RESULTS

TABLE I. THE EXPERIMENTAL SEQUENCE

Time	Flow	Actuation	Phase
5 min	Still	off	-
5 min	KVS	off	-
2 min	KVS	on	0 deg
2 min	KVS	on	30 deg
2 min	KVS	on	60 deg
...
2 min	KVS	on	330 deg
2 min	KVS	on	360 deg
5 min	KVS	off	-
5 min	Still	off	-

To test the control algorithm the experiments were carried out in sequence described in Table I. There are 5 minute data recording periods, with no actuation, for still water and Kármán vortex street at the beginning and at the end of the experiment. In between the data for the different phase shifts are recorded starting with 0 degrees and ending with 360 degrees. The phase shift is changed with 30 degree increments with 2 minutes of data recording for every step of the phase shift. From this data an average thrust coefficient C_t and average efficiency η can be calculated for every phase with the following equations:

$$C_t = \frac{2 * F_t}{\rho * v^2 * A}$$

$$\eta = \frac{F_t * v}{\tau * \omega}$$

where F_t is the thrust force, ρ is the fluid density, v is the swimming speed (or in our case the speed of vortex traveling), A is the cross-section area of the fish, τ is the torque of the tail and ω is the angular velocity of the motor.

Figure 8 plots the thrust coefficient C_t with respect to the phase and Figure 9 shows the efficiency with respect to the phase. Phases 0 degrees and 360 degrees correspond to the same time delay T when measured from the time the pressure maximum was sensed by the nose. Each data point on the plots is an average taken over a 60 second time period with standard deviations plotted as error bars. $C_t = 0$ represents the average drag force that acts upon the robotic fish when the actuation is switched off and the tail is parallel with the free stream flow.

In Figure 8 the maximum thrust coefficient 0.44 is achieved at the phase shift angle 330 degrees and the minimum thrust coefficient 0.1 at 90 degrees. The efficiency graph is slightly shifted compared to the thrust showing that the maximum thrust does not necessarily lead to maximum efficiency. The maximum efficiency 0.345 on Figure 9 is at the phase shift angle 360 degrees and the minimum 0.114 at 180 degrees.

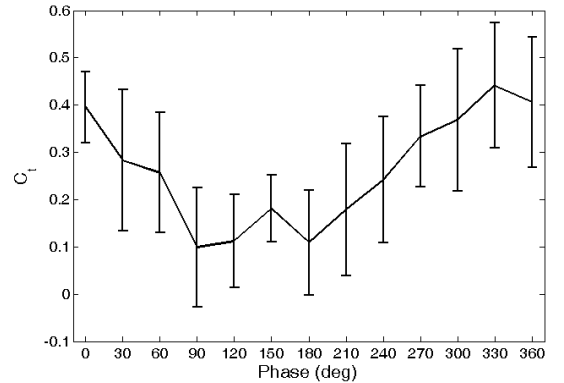


Figure 8. Thrust coefficient C_t with respect to the phase. Error bars show standard deviation of C_t .

The efficiency of the robotic fish does not reach 100% but that was expected as the robotic fish was fixed to the force gauge. With no lateral movement the efficiency difference of 23% was still achieved between the phases 360 (0) degrees and 180 degrees.

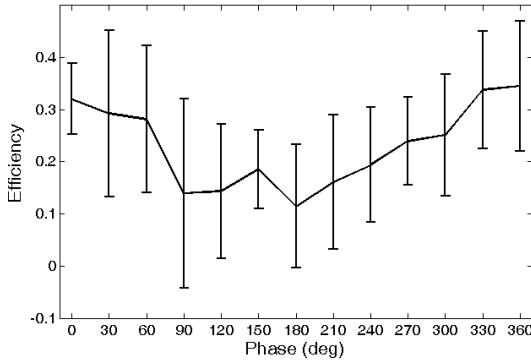


Figure 9. The efficiency η with respect to the phase. Error bars show standard deviation of η .

Since the flow conditions are never perfect, the standard deviations for those measurements are high. We associate these errors with strength and speed of the vortices that vary over time as they imping on the robot. Fluctuations in strength of the vortex can affect how well the robotic fish can use these to harvest energy while changes in vortex traveling speed can cause the actual phase shift with respect to vortex to be different from the desired phase shift.

IV. DISCUSSION

Our results show that the energy harvesting with a robotic fish can be achieved using flow sensing without the necessity to control the turbulence. The timing of the tail beat with respect to an oncoming vortex is important and pressure difference across the head can be used to analyse the flow online for vortex synchronization.

Fish harvesting energy in Kármán vortex streets have been documented in [5]. It was also shown that a hydrofoil that is controlled laterally and angularly can benefit from the synchronicity with the Kármán vortex street [7-8]. However, so far very little is understood about the strategies of fluid-structure interaction which take advantage of readily available vortices. For instance, the kinematics of a Kármán gaiting fish has components of translation, head movement, body bending and tail beat. The contribution of each one of these components to the resultant behaviour still needs to be addressed.

In this study, we single out the tail beat motion by harnessing the robot (no lateral or rotational motion) and demonstrate that an increase of 23% in efficiency can still be generated with a particular phase between tail beat interacting with a wake. The timing is controlled in real time by detecting the pressure maximum on the head and anticipating its arrival time to the tail.

Given that an unharnessed robot has little control over the

lateral translation and rotation, we understand that more sophisticated control algorithms are needed to control the free swimming robot in turbulent flow, even if it is predictable like Kármán vortex streets, where force profiles over the robot are complex and subject to unpredictable changes. However, low-level control methods for vortex exploitation, such as the one presented here, can be key to increase power efficiency or generate high acceleration.

V. ACKNOWLEDGMENTS

This work is carried out under the FILOSE project, supported by the European Union, seventh framework programme (FP7-ICT-2007-3).

REFERENCES

- [1] C. L. Gerstner, "Use of substratum ripples for flow refuging by Atlantic cod, *Gadus morhua*," *Environmental Biology of Fishes*, vol. 51, pp. 455-460, 1998.
- [2] C. L. Gerstner and P. W. Webb, "The station-holding performance of the plaice *Pleuronectes platessa* on artificial substratum ripples," *Canadian Journal of Zoology*, vol. 76, no. 2, pp. 260-268, 1998.
- [3] P. W. Webb, "Entrainment by river chub *Nocomis micropogon* and smallmouth bass *Micropterus dolomieu* on cylinders," *Journal of Experimental Biology*, vol. 201, pp. 2403-2412, 1998.
- [4] J. C. Liao, "A review of fish swimming mechanics and behaviour in altered flows," *Philosophical transactions of the Royal Society of London. Series B, Biological sciences*, vol. 362, no. 1487, pp. 1973-93, 2007.
- [5] J. C. Liao, "The Karman gait: novel body kinematics of rainbow trout swimming in a vortex street," *Journal of Experimental Biology*, vol. 206, no. 6, pp. 1059-1073, 2003.
- [6] J. C. Liao, D. N. Beal, G. V. Lauder, and M. S. Triantafyllou, "Fish exploiting vortices decrease muscle activity," *Science (New York, N.Y.)*, vol. 302, no. 5650, pp. 1566-9, 2003.
- [7] R. Gopalkrishnan, M. S. Triantafyllou, G. S. Triantafyllou, and D. Barrett, "Active vorticity control in a shear flow using a flapping foil," *Journal of Fluid Mechanics*, vol. 274, pp. 1-21, 1994.
- [8] M. S. Triantafyllou, A. H. Techet, Q. Zhu, D. N. Beal, F. S. Hover, and D. K. P. Yue, "Vorticity control in fish-like propulsion and manoeuvring," *Integrative and comparative biology*, vol. 42, no. 5, pp. 1026-31, 2002.
- [9] R. Venturelli et al., "Hydrodynamic pressure sensing with an artificial lateral line in steady and unsteady flows," *Bioinspiration & biomimetics*, vol. 7, no. 3, p. 036004, 2012.
- [10] T. Salumäe and M. Krusmaa, "A flexible fin with bio-Inspired stiffness profile and geometry," *Journal of Bionic Engineering*, vol. 8, no. 4, pp. 418-428, 2011.

Acknowledgements

I would like to express my sincere gratitude to my supervisor Professor Maarja Kruusmaa whose guidance, advice, support, criticism and knowledge have made completion of this work possible.

I want to thank all the people from the Centre for Biorobotics for providing every kind of support for my work. I also want to thank Dr. Otar Akanyeti, Dr. Lily D. Chambers and Professor William M. Megill for their supervision and knowledge for me and my work.

Financially my research has been funded from the FILOSE project, supported by the European Union, seventh framework programme (FP7-ICT-2007-3) along with the support from Estonian Science Foundation and Archimedes Foundation which are greatly appreciated.

Finally I want to thank my family and friends for their encouragement and support which have kept me thriving in my studies.

Abstract

Pressure sensitive lateral line for underwater robot

In order to use different flow regimes, underwater robots need to have sensors that can detect them. Fish can sense flow with their lateral line organ that consists of hundreds of flow and pressure sensitive sensors covering their body. By example of those, artificial lateral line sensors are being developed for use on underwater robots.

In this thesis we have used miniature pressure sensors assembled into arrays for artificial lateral lines, designed for different sensing platforms. We have developed these sensing platforms for different tasks relating to the flow feature recognition. The overall objective of this research is to advance the use of flow information for control of underwater vehicles.

To do that, we have studied how to recognize different flow regimes and present a comparison of steady flow and periodically turbulent flow from the perspective of underwater robots. With different scenarios we investigate how the flow regimes would be felt from different angles and positions. By comparing the flow regimes we also demonstrate which data processing tools are suitable for flow data analysis, as the data from the hydrodynamic environment is noisy and hard to interpret.

It is a common problem with any sensory system to pick up noise and other stimuli that interfere with useful signals. When a flow sensing system is mounted on an underwater vehicle, it should be taken into consideration that this system also provides information about the craft's movements that modify the surrounding flow field. To separate the self-motion information from the rest of the flow stimuli we have developed a model that can estimate motion mediated signals in lateral line sensors. The model is built based on experimental data, containing craft's movement information and signals sensed by the pressure sensing lateral line. This way an underwater robot equipped with an accelerometer can enhance its sense of external stimuli that would be otherwise masked by disturbances created by the robot's own motion.

This kind of selective filtering could be very useful for fishlike robots, trying to sense flow features while undulating in periodically turbulent flows. We show that the flow information in periodic turbulence can be used for control of the robot to increase its swimming performance. Matching only the frequency of flow features is not enough to enhance propulsion of the tail while a proper timing of the tail beat with respect to the vortices results in more thrust and makes the propulsion more efficient compared to that in steady flows. With correct synchronization the power used to move the tail is directed from producing lateral forces to thrust, making the underwater robot's movement in turbulent flows more stable.

Lühikokkuvõte

Rõhutundliku küljejoone kasutamine allveerobotil

Allveekeskkonnas on robotitel raske toime tulla, kuna neil puuduvad andurid vedelikuvoolu tunnetamiseks. Kaladel on selleks eraldi meeleeelund, küljejoon, mille voolu- ja rõhutundlikud andurid katavad kogu nende keha. Bioloogiliste vooluandurite näitel on hakatud välja arendama ka tehis küljejooneandureid, mida saab kasutada allveerobotitel.

Käesolevas väitekirjas on kasutatud miniatuurseid rõhuandureid, millest on koostatud tehisküljejooned erinevate vooluvälja mõõtvate platvormide jaoks. Need andurite platvormid on arendatud vedelikuvoolus katsete tegemiseks, et selgitada välja, kuidas allveerobotid saaksid eristada voolurežiime. Antud uuringu peamiseks eesmärgiks on arendada vedeliku voolust saadava teabe kasutatavust allveerobotite juhtimises.

Selle saavutamiseks oleme uurinud erinevate voolurežiimide tuvastamist allveeroboti perspektiivist vaadatuna. Mitmeid stsenaariumeid katsetades vaatesime, kuidas allveerobot tunnetab voolu erinevate nurkade alt ja erinevates asukohtades vedelikuvoolu suhtes. Vooluvälja mõõtmiste põhjal näitasime, millised andmetöötluse viisid on kasulikud vedelikuvoolu andmete analüüsimiseks ja tõlgendamiseks, et eraldada mürastest mõõtmistest allveeroboti juhtimiseks vajalik teave.

Andurisüsteemidaga on tavaline probleem, et lisaks kasulikule signaalile mõõdavad need ka müra ja muid ebavajalikke signaale. Nii on ka tehisküljejoon tundlik allveeroboti enda liigutustele, kuna need mõjutavad vooluvälja roboti ümber. Roboti liigutustest tingitud muutuste eemaldamiseks vooluandurite mõõtmistest arendasime välja meetodi, millega saab hinnata neid muutusi liikumisandurilt saadava teabe põhjal. Antud meetod kasutab eksperimentaalselt kogutud liikumise ja vedelikuvoolu andmeid, et luua konkreetsele robotile spetsiifiline mudel, mis arvestab roboti kuju ja küljejooneandurite asetusega. Sellist mudelit kasutades saab kiirendusanduritega varustatud allveerobot suurendada oma küljejoone tundlikkust välistele allikatele, mille põhjustatud vedelikuvoolu muutused oleks muidu kaetud roboti enda liikumisest tulenevate muutustega.

Seda laadi valikuline filtreerimine on väga kasulik uimede abil liikuvatele robotitele, mis tahavad ujudes ka vooluvälja mõõta. Antud situatsioonis on näiteks robot, mis kasutab voolust saadavat teavet, et ajastada oma uimetööd perioodilise vooluga. Me oleme näidanud, et perioodiliselt turbulentses voolus ujudes on õige ajastusega võimalik tõsta roboti ujumise jõudlust. Sabauime korrektne sünkroniseerimine perioodiliselt turbulentses voolus leiduvate keeristega suurendab roboti poolt edasiliikumiseks tekitatud jõudu ja muudab selle tekitamise efektiivsemaks võrreldes ühtlases voolus ujumisega. Õige ajastusega tekitatakse ka vähem külgsuunalisi jõude, muutes allveeroboti liikumise turbulentses voolus stabiilsemaks.

Curriculum Vitae

Personal Data

Name: Jaas Ježov
Birth date: 15.07.1983
Birth place: Kuressaare, Estonia
Citizenship: Estonian
Marital status: single

Contact Data

Address: Uus 20-40, 50604 Tartu, Estonia
Phone: +372 53326107
E-mail: jaas.jezov@gmail.com

Education

2008–2013 Tallinn University of Technology PhD studies
2006–2008 University of Tartu MSc (information technology)
2003–2006 University of Tartu BSc (information technology)

Language competence

Estonian: native
English: fluent

Professional employment

2012–2013 Tallinn Univ. of Tech., Centre for Biorobotics; junior researcher
2007–2012 University of Tartu; engineer
2006–2007 AS Webmedia; junior software developer

Defended thesis

MSc thesis (2008): “Robotic mannequin”
(sup) Alvo Aabloo, Artur Abels
BSc thesis (2006): “Dynamic measurements of IPMC resistance”
(sup) Alvo Aabloo, Andres Punning

Research interests

Underwater robotics, flow sensing, CFD simulations.

Elulookirjeldus

Isikuandmed

Nimi: Jaas Ježov
Sünniaeg: 15.07.1983
Sünnikoht: Kuressaare, Eesti
Kodakondsus: eestlane
Perekonnaseis: vallaline

Kontaktandmed

Aadress: Uus 20-40, 50604 Tartu, Eesti
Telefon: +372 53326107
E-mail: jaas.jezov@gmail.com

Hariduskäik

2008–2013 Tallinna Tehnikaülikool doktoriõpe
2006–2008 Tartu Ülikool tehnikateaduse magister (infotehnoloogia)
2003–2006 Tartu Ülikool tehnikateaduse bakalaureus (infotehnoloogia)

Keeleoskus

Eesti keel: emakeel
Inglise keel: kõrgtase

Teenistuskäik

2012–2013 Tallinna Tehnikaülikool, Biorobootika keskus; nooremteadur
2007–2012 Tartu Ülikool; insener
2006–2007 AS Webmedia; nooremprogrammeerija

Kaitstud lõputööd

Magistritöö (2008): “Robot mannekeen”
(juh) Alvo Aabloo, Artur Abels
Bakalaureusetöö (2006): “IPMC takistuse dünaamiline mõõtmine”
(juh) Alvo Aabloo, Andres Punning

Teadustöö põhisuunad

Allveerobootika, vedelikuvoolu andurid, hüdrodünaamika simulatsioonid.

**DISSERTATIONS DEFENDED AT
TALLINN UNIVERSITY OF TECHNOLOGY ON
*INFORMATICS AND SYSTEM ENGINEERING***

1. **Lea Elmik**. Informational Modelling of a Communication Office. 1992.
2. **Kalle Tammemäe**. Control Intensive Digital System Synthesis. 1997.
3. **Eerik Lossmann**. Complex Signal Classification Algorithms, Based on the Third-Order Statistical Models. 1999.
4. **Kaido Kikkas**. Using the Internet in Rehabilitation of People with Mobility Impairments – Case Studies and Views from Estonia. 1999.
5. **Nazmun Nahar**. Global Electronic Commerce Process: Business-to-Business. 1999.
6. **Jevgeni Riipulk**. Microwave Radiometry for Medical Applications. 2000.
7. **Alar Kuusik**. Compact Smart Home Systems: Design and Verification of Cost Effective Hardware Solutions. 2001.
8. **Jaan Raik**. Hierarchical Test Generation for Digital Circuits Represented by Decision Diagrams. 2001.
9. **Andri Riid**. Transparent Fuzzy Systems: Model and Control. 2002.
10. **Marina Brik**. Investigation and Development of Test Generation Methods for Control Part of Digital Systems. 2002.
11. **Raul Land**. Synchronous Approximation and Processing of Sampled Data Signals. 2002.
12. **Ants Ronk**. An Extended Block-Adaptive Fourier Analyser for Analysis and Reproduction of Periodic Components of Band-Limited Discrete-Time Signals. 2002.
13. **Toivo Paavle**. System Level Modeling of the Phase Locked Loops: Behavioral Analysis and Parameterization. 2003.
14. **Irina Astrova**. On Integration of Object-Oriented Applications with Relational Databases. 2003.
15. **Kuldar Taveter**. A Multi-Perspective Methodology for Agent-Oriented Business Modelling and Simulation. 2004.
16. **Taivo Kangilaski**. Eesti Energia käiduhaldussüsteem. 2004.
17. **Artur Jutman**. Selected Issues of Modeling, Verification and Testing of Digital Systems. 2004.
18. **Anders Tenno**. Simulation and Estimation of Electro-Chemical Processes in Maintenance-Free Batteries with Fixed Electrolyte. 2004.
19. **Oleg Korolkov**. Formation of Diffusion Welded Al Contacts to Semiconductor Silicon. 2004.
20. **Risto Vaarandi**. Tools and Techniques for Event Log Analysis. 2005.

21. **Marko Koort**. Transmitter Power Control in Wireless Communication Systems. 2005.
22. **Raul Savimaa**. Modelling Emergent Behaviour of Organizations. Time-Aware, UML and Agent Based Approach. 2005.
23. **Raido Kurel**. Investigation of Electrical Characteristics of SiC Based Complementary JBS Structures. 2005.
24. **Rainer Taniloo**. Ökonoomsete negatiivse diferentsiaaltakistusega astmete ja elementide disainimine ja optimeerimine. 2005.
25. **Pauli Lallo**. Adaptive Secure Data Transmission Method for OSI Level I. 2005.
26. **Deniss Kumlander**. Some Practical Algorithms to Solve the Maximum Clique Problem. 2005.
27. **Tarmo Vesikioja**. Stable Marriage Problem and College Admission. 2005.
28. **Elena Fomina**. Low Power Finite State Machine Synthesis. 2005.
29. **Eero Ivask**. Digital Test in WEB-Based Environment 2006.
30. **Виктор Войтович**. Разработка технологий выращивания из жидкой фазы эпитаксиальных структур арсенида галлия с высоковольтным р-п переходом и изготовления диодов на их основе. 2006.
31. **Tanel Alumäe**. Methods for Estonian Large Vocabulary Speech Recognition. 2006.
32. **Erki Eessaar**. Relational and Object-Relational Database Management Systems as Platforms for Managing Softwareengineering Artefacts. 2006.
33. **Rauno Gordon**. Modelling of Cardiac Dynamics and Intracardiac Bio-impedance. 2007.
34. **Madis Listak**. A Task-Oriented Design of a Biologically Inspired Underwater Robot. 2007.
35. **Elmet Orasson**. Hybrid Built-in Self-Test. Methods and Tools for Analysis and Optimization of BIST. 2007.
36. **Eduard Petlenkov**. Neural Networks Based Identification and Control of Nonlinear Systems: ANARX Model Based Approach. 2007.
37. **Toomas Kirt**. Concept Formation in Exploratory Data Analysis: Case Studies of Linguistic and Banking Data. 2007.
38. **Juhan-Peep Ernits**. Two State Space Reduction Techniques for Explicit State Model Checking. 2007.
39. **Innar Liiv**. Pattern Discovery Using Seriation and Matrix Reordering: A Unified View, Extensions and an Application to Inventory Management. 2008.
40. **Andrei Pokatilov**. Development of National Standard for Voltage Unit Based on Solid-State References. 2008.

41. **Karin Lindroos**. Mapping Social Structures by Formal Non-Linear Information Processing Methods: Case Studies of Estonian Islands Environments. 2008.
42. **Maksim Jenihhin**. Simulation-Based Hardware Verification with High-Level Decision Diagrams. 2008.
43. **Ando Saabas**. Logics for Low-Level Code and Proof-Preserving Program Transformations. 2008.
44. **Ilja Tšahhirov**. Security Protocols Analysis in the Computational Model – Dependency Flow Graphs-Based Approach. 2008.
45. **Toomas Ruuben**. Wideband Digital Beamforming in Sonar Systems. 2009.
46. **Sergei Devadze**. Fault Simulation of Digital Systems. 2009.
47. **Andrei Krivošei**. Model Based Method for Adaptive Decomposition of the Thoracic Bio-Impedance Variations into Cardiac and Respiratory Components. 2009.
48. **Vineeth Govind**. DfT-Based External Test and Diagnosis of Mesh-like Networks on Chips. 2009.
49. **Andres Kull**. Model-Based Testing of Reactive Systems. 2009.
50. **Ants Torim**. Formal Concepts in the Theory of Monotone Systems. 2009.
51. **Erika Matsak**. Discovering Logical Constructs from Estonian Children Language. 2009.
52. **Paul Annus**. Multichannel Bioimpedance Spectroscopy: Instrumentation Methods and Design Principles. 2009.
53. **Maris Tõnso**. Computer Algebra Tools for Modelling, Analysis and Synthesis for Nonlinear Control Systems. 2010.
54. **Aivo Jürgenson**. Efficient Semantics of Parallel and Serial Models of Attack Trees. 2010.
55. **Erkki Joason**. The Tactile Feedback Device for Multi-Touch User Interfaces. 2010.
56. **Jürgo-Sören Preden**. Enhancing Situation – Awareness Cognition and Reasoning of Ad-Hoc Network Agents. 2010.
57. **Pavel Grigorenko**. Higher-Order Attribute Semantics of Flat Languages. 2010.
58. **Anna Rannaste**. Hierarcical Test Pattern Generation and Untestability Identification Techniques for Synchronous Sequential Circuits. 2010.
59. **Sergei Strik**. Battery Charging and Full-Featured Battery Charger Integrated Circuit for Portable Applications. 2011.
60. **Rain Ottis**. A Systematic Approach to Offensive Volunteer Cyber Militia. 2011.
61. **Natalja Sleptšuk**. Investigation of the Intermediate Layer in the Metal-Silicon Carbide Contact Obtained by Diffusion Welding. 2011.

62. **Martin Jaanus.** The Interactive Learning Environment for Mobile Laboratories. 2011.
63. **Argo Kasemaa.** Analog Front End Components for Bio-Impedance Measurement: Current Source Design and Implementation. 2011.
64. **Kenneth Geers.** Strategic Cyber Security: Evaluating Nation-State Cyber Attack Mitigation Strategies. 2011.
65. **Riina Maigre.** Composition of Web Services on Large Service Models. 2011.
66. **Helena Kruus.** Optimization of Built-in Self-Test in Digital Systems. 2011.
67. **Gunnar Piho.** Archetypes Based Techniques for Development of Domains, Requirements and Software. 2011.
68. **Juri Gavšin.** Intrinsic Robot Safety Through Reversibility of Actions. 2011.
69. **Dmitri Mihhailov.** Hardware Implementation of Recursive Sorting Algorithms Using Tree-like Structures and HFSM Models. 2012.
70. **Anton Tšertov.** System Modeling for Processor-Centric Test Automation. 2012.
71. **Sergei Kostin.** Self-Diagnosis in Digital Systems. 2012.
72. **Mihkel Tagel.** System-Level Design of Timing-Sensitive Network-on-Chip Based Dependable Systems. 2012.
73. **Juri Belikov.** Polynomial Methods for Nonlinear Control Systems. 2012.
74. **Kristina Vassiljeva.** Restricted Connectivity Neural Networks based Identification for Control. 2012.
75. **Tarmo Robal.** Towards Adaptive Web – Analysing and Recommending Web Users' Behaviour. 2012.
76. **Anton Karputkin.** Formal Verification and Error Correction on High-Level Decision Diagrams. 2012.
77. **Vadim Kimlaychuk.** Simulations in Multi-Agent Communication System. 2012.
78. **Taavi Viilukas.** Constraints Solving Based Hierarchical Test Generation for Synchronous Sequential Circuits. 2012.
79. **Marko Kääramees.** A Symbolic Approach to Model-based Online Testing. 2012.
80. **Enar Reilent.** Whiteboard Architecture for the Multi-agent Sensor Systems. 2012.
81. **Jaan Ojarand.** Wideband Excitation Signals for Fast Impedance Spectroscopy of Biological Objects. 2012.
82. **Igor Aleksejev.** FPGA-based Embedded Virtual Instrumentation. 2013.
83. **Juri Mihhailov.** Accurate Flexible Current Measurement Method and its Realization in Power and Battery Management Integrated Circuits for Portable Applications. 2013.

84. **Tõnis Saar**. The Piezo-Electric Impedance Spectroscopy: Solutions and Applications. 2013.
85. **Ermo Täks**. An Automated Legal Content Capture and Visualisation Method. 2013.
86. **Uljana Reinsalu**. Fault Simulation and Code Coverage Analysis of RTL Designs Using High-Level Decision Diagrams. 2013.
87. **Anton Tšepurov**. Hardware Modeling for Design Verification and Debug. 2013.